UNIVERSITÀ DEGLI STUDI DI PARMA

Dottorato di ricerca in Fisica
XXVII ciclo

HYBRID ORGANIC-INORGANIC NANOSTRUCTURES AND INTERFACES:
FROM FUNDAMENTAL STUDIES OF LOW DIMENSIONAL SYSTEMS TO BIOMEDICAL APPLICATIONS

COORDINATORE:
Chiar.mo Prof. Cristiano Viappiani

TUTOR:
Chiar.mo Prof. Luigi Cristofolini

DOTTORANDO:
Tiziano Rimoldi

Abstract

This thesis reports some studies of interfacial systems for biomedical applications. Nanosystems for Self Lighting Photo Dynamic Therapy (SLPDT) of cancer have been characterized from the growth steps up to the in vitro tests. At the same time, from a more fundamental point of view, aggregation and spontaneous fluctuation dynamics in interfacial model systems has been investigated.

Several complementary techniques are employed for a comprehensive characterization of nanostructures (i.e. SEM, TEM, AFM) and for the study of their optical properties (i.e. microfluorescence, epifluorescence). Farther, for this cutting-edge research, state-of-the-art techniques have been employed: for instance, i) singlet oxygen production was excited by irradiation with a 6 MeV Linac; ii) mechanical properties of delicate Langmuir monolayers have been measured by ad-hoc developed techniques; iii) spontaneous fluctuation dynamics was characterized by synchrotron X-ray photon correlation spectroscopy (XPCS).

The thesis begins reporting investigations on molecular layers of porphyrins deposited by Supersonic Molecular Beam Deposition (SuMBD) as idealized interfaces to comprehend the more complex nanosystem i.e. porphyrinated core-shell nanowires constituted by a silica coating around a silicon carbide core. The latter are developed and studied for SLPDT applications. SLPDT is the evolution of the standard PDT to the treatment of deep tumors; the porphyrins locally activated by nanowires -suitably excited by X-rays- react with the oxygen molecules present in tissues, generating cytotoxic singlet oxygen. In this framework, besides nanowires, other nanostructures have been synthesized to pursue the maximum efficiency i.e. core-shell nanoparticles based on CeF_3 surrounded by an oxide cladding. CeF_3 is a very efficient scintillator converting X-ray photons in visible light while the oxide cladding allows many easy functionalization processes for biocompatibility and targeting.

At the same time, some model interfacial systems have been investigated: firstly, a Langmuir network of hydrophobic gold nanoparticles at air/water interface to understand aggregation processes and to study the evolution of the dynamics at nanoscopic scale. Furthermore, a Langmuir mixed monolayer of lipid and silica nanoparticles has been investigated as a model system for the interactions between hydrophilic nanoparticles and a simple model of cell membrane.

It is expected that studies like those presented here shall prove useful to understand the behavior of nanostructures in interaction with bio-interfaces and shall pave the way for novel applications.

Summary

1 Introduction and motivations

The development of multifunctional nanomaterials for biomedical applications is one of the main aims in nanotechnology. Key points are: 1) the optimization of the material, and 2) a detailed control of the structure and the dynamics of the interfaces that are formed between the nanostructure and biological matter.

An interesting recent development is the idea of Self-Lighting photodynamic therapy (SLPDT [Juzenas2008]). It is an extension of the traditional photodynamic therapy (PDT [Dolmans2003]). PDT is usually used to treat tumors on or just under the skin by the photo-induced production of the strongly oxidizing singlet oxygen species. As shown in **Figure 1.1**, a laser light is used to excite a photosensitizer (PS), e.g. organic dyes and aromatic hydrocarbons, porphyrins, phthalocyanines and related tetrapyrroles etc. [Bonnett1995], to its excited state. Subsequently, it can have an intersystem-crossing to a triplet excited state that can excite the oxygen molecules, present in tissues to treat, from their triplet ground state ($^3O_2$) to their singlet excited state ($^1O_2$). This one is highly cytotoxic and causes death of tissues through oxidative stress.

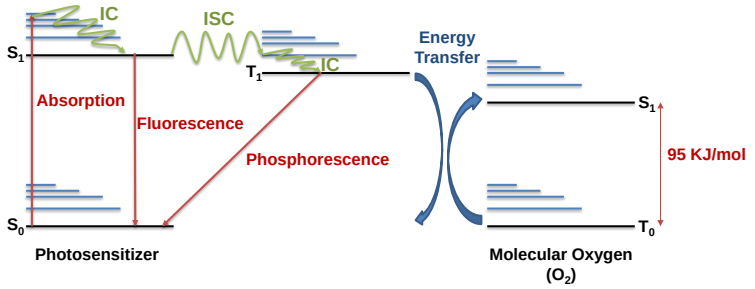

Figure 1.1 Mechanism of PDT along with other possible competitive mechanisms: in green are shown the internal conversion (disexcitations of vibrational modes, IC) and the intersystem-crossing (ISC). The second one has high probability to occur if the others disexcitations (i.e. fluorescence and phosphorescence) have long decay rates.

The newly proposed technique SLPDT consists in extending the traditional PDT to those cancer tissues which are not directly reachable by light, using the "local" source of light constituted by scintillator nanostructures, such as nanoparticles, nanotubes or nanowires coated with layers of organic photosensitizers [Lal2008, Llusarand2008, Zou2014]. When these systems are irradiated with X-rays, in a similar manner as in the traditional radiotherapy of cancer, the cascade process originated by the scintillator and put forward by the organic coating, results in the final production of oxidizing species that kill cancer cells. As this process happens at interfaces, the interfacial properties play a key role towards the desired functionality.
Recent pilot studies [Juzenas2008, Chen2006, Liu2008] indicate that this might work: scintillating nanostructures can potentially be used to activate photodynamic therapy as a promising deep cancer treatment modality. The process is shown in (**Figure 1.2**): energetic X-rays are used to excite a scintillating nanostructure (SNt), where the PS are previously attached, then an energy transfer from the SNt to the PS could excite the second one. From this point the mechanism of singlet oxygen production is the same as in the standard PDT. Because X-rays can easily penetrate deeply in tissues, SLPDT can overcome the main problem of the standard PDT: the capability to treat deep tumors.

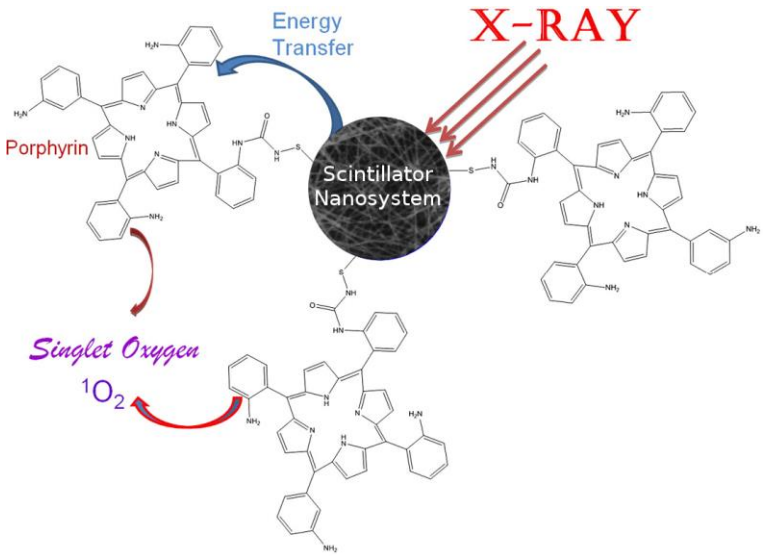

Figure 1.2 Scheme of the Self-Lighting Photo Dynamic Therapy mechanism: X-rays excite the scintillating nanosystem then, an energy transfer to the photosensitizer (i.e. porphyrin) allows the production of singlet oxygen by the second one.

Most part of my project is framed in this broad scenery, in particular in the project called "Innovative multifunctional hybrid nanosystems for biomedical applications" (BioNiMED), coordinated by Dr. Giancarlo Salviati from IMEM-CNR institute of Parma. In detail, the nanosystem studied is a hybrid organic-inorganic based on 3C-SiC@SiO_x core-shell nanowires functionalized with porphyrin molecules. The goal is to kill deep tumors while minimizing side effects of the actual clinical treatments mainly due to the high doses of X-rays released in the radiotherapy protocols.
Within the BioNiMED project, my work is focused on the optical and functional study of the proposed hybrid nanosystem: in particular on the study of the SLPDT mechanism.
The choice of porphyrin molecules to functionalize the nanowires surface is motivated by the fact that they are well known photosensitizers [Ackroyd2001] for standard PDT treatments. At the same time, the SiC@SiO_x core-shell nanowires are promising as scintillating nanostructure for two main reasons: SiC has been

proven to be biocompatible[Saddow2011] besides having the 3C-SiC near band edge (NBE) emission that matches with Q absorption bands of porphyrins [Gouterman1961, 1963]. Unfortunately SiC is not an effective emitter because it is a semiconductor with an indirect band gap but it is first demonstrated that the SiC@SiO_x core-shell nanostructure strongly enhances the NWs luminescence efficiency due to the carriers confinement in a type-I quantum well, in which the SiO_x shell makes the barriers [Fabbri2010].
Due to their shape and size, nanowires do not have the capability to move and diffuse inside the tissues. This can be an advantage in terms of localization of the treatment but, at the same time, could be a drawback due to the local nature of the oxidizing process. The energy transfer that is responsible for the excitation of oxygen molecules, in the SLPDT process, can occurs only if they are in the range of few nanometers from porphyrinated nanowires. Moreover, the typical lifetime of singlet oxygen in water is about 3-4 μs [Kuimova2009]; accordingly, their mean free path is short (up to 200 nm treating $^1O_2$ molecules as Brownian diffusors). Therefore, it is needed to arrange the nanowires to maximize their effect i.e. on the cells membrane, inside the nuclei etc. This is at odds with the natural endocytosis process: TEM imaging has shown that during the cell uptake, NWs are internalized in bundles inside vesicles [Cacchioli2014]. Therefore this situation might obstruct the effectiveness of the treatment protecting vital parts of the cells.
To overcome this obstacle, and to maximize the performance of the process, a complementary approach has been pursued, i.e. growing nanoparticles that can have high capability to diffuse. In this case, the main problem is the confinement of nanoparticles in the region to treat: the necessity is foreseen in a new step of functionalization in which targeting receptor molecules, able to stick on i.e. cell membrane, organelles etc., are anchored on nanoparticles surface.
In this direction, a preliminary study on a different nanostructure based on CeF_3@ZnO core-shell nanoparticles has been performed during my visit at University of Texas at Arlington in the group of Prof. Wey Chen: one of the pioneers of SLPDT mechanism. The work is aimed to combine the efficiency of CeF_3 to convert X-rays in visible light with the biocompatibility and the various functionalization processes available for ZnO.

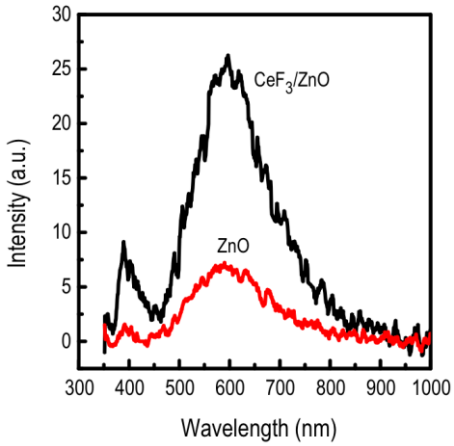

Figure 1.3 Enhancement of the X-ray luminescence of ZnO in CeF_3/ZnO nanocomposites, taken from [Sahi2011].

Starting from a work of Sunil Sahi and Wei Chen [Sahi2011] where in CeF_3/ZnO nanocomposites the X-ray luminescence of ZnO is enhanced by a factor of 4 (**Figure 1.3**), the study is focused on the synthesis of the core-shell structure in which an increase of the effect is expected due to the optimized structure.
Nevertheless, the characterization of the nanostructure and the improvement of singlet oxygen production are only one side of the study. The comprehension of the local interactions, involved among nanostructures and between nanostructures and biological interfaces, is fundamental as the intrinsic study of the nanostructure properties and functionalities. In particular, the interaction between the nanostructures and the biological interfaces, as cells membrane, is central because these nanosystems have to pass through or stuck onto the cells membrane during the internalization process.
In this way, to investigate the collective behavior and the physics of interactions, as model nanostructure we also studied different bidimensional networks based on nanoparticles. To obtain a 2D network at air/water interface is exploited the Langmuir technique, one the most suitable to control the speed of network formation and to contemporary study the dynamics as a function of the network packing. To study the evolution of the dynamics of these networks is employed the grazing-incidence X-ray Photon

Correlation Spectroscopy technique (GI-XPCS) available at synchrotron ESRF of Grenoble (FR); the setup is schematized in **Figure 1.4**.
Firstly are studied hydrophobic gold nanoparticles, stabilized by dodecanethiols, to understand the ensemble dynamics and the interactions involved between them.

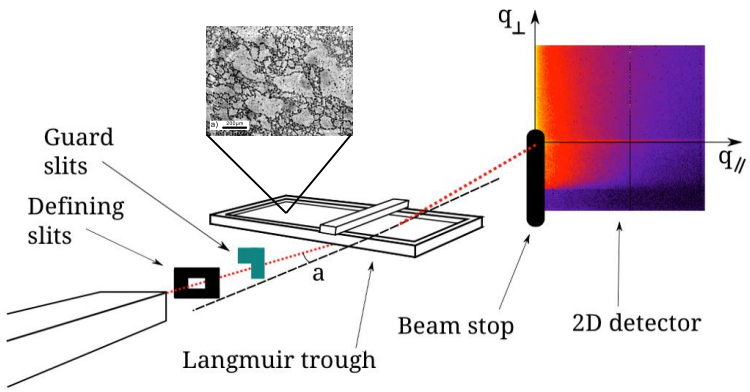

Figure 1.4 Scheme of the GI-XPCS setup used for the measurements of the microscopic dynamics on the gold nanoparticles 2D network.

The phenomenology related to the formation of the network was well known from previous works of our group [Orsi2012]. In the incubation time, in which individual nanoparticles diffuse and aggregates driven by hydrophobic interactions, are formed small disk-like aggregates. During the compression three steps occur: i) disks of sufficient size aggregate because of their mutual attraction and when, at least two disks stick together, the aggregation proceeds tip to tip [Schmidle2013] resulting in the formation of a quasi-1D structures; ii) growth of branched structure upon percolation; iii) final compaction of the structure.
We also studied another bidimensional network based on silica nanoparticles interacting with a phospholipid monolayer of DPPC. The choice of DPPC is related to its abundance in cell membranes and in the lung surfactant (40% in weight of their total solid content [Boal2012]) while silica nanoparticles are extensively utilized in various applications [Santini2012].

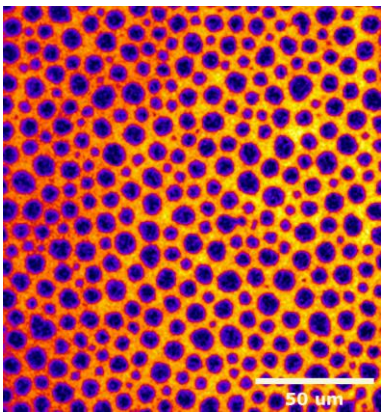

Figure 1.5 Black circular features stabilized by the incorporation of silica nanoparticles in the DPPC Langmuir monolayer. Image in in false color.

DPPC is well known to have two distinct liquid phases at the air/water interface, called liquid expanded (LE) and liquid condensed (LC) with a plateau in the Langmuir isotherm in which LC domains coexist with LE regions [Courrier2003]. Moreover, many studies have shown that the incorporation of nanoparticles, in phospholipid monolayers [Guzmán2014], changes the structural properties of the monolayer.
The presence of black circular features (**Figure 1.5**), which seem the phantoms of the LC domains, are stable even at the highest attainable pressure and they are responsible of film morphology and of its microscopic dynamics. To characterize the latter, we introduced a novel, comprehensive approach: we combined an experimental technique operating in the direct space -micro-tracking- and GI-XPCS on the same system. GI-XPCS provides excellent statistics, but its results are deduced through model-dependent analysis. Micro-tracking, on the other hand, unveils the model but often suffers from limited statistics. In this way we could show a smooth and controlled evolution of the circular features dynamics while increasing surface compression.
These studies of the dynamics at mixed interfaces, might be of use to model the aggregation and localization processes that take place when nanosystems are let interact with bio-membranes and interfaces. For instance we can imagine that after the injection of a certain amount of nanoparticles in a cell culture, locally the concentration could be enough to induce the formation of

aggregates that i) can grow as rigid networks and then, ii) stick on cells surface. As a result, the change in the shape of the nanostructures might be effective to enhance their spreadability. At the same time, it is necessary to control the surface hydrophobicity/philicity and, more in general, the surface coverage.

2 *Background on nanostructures production*

The films studied in this thesis are obtained with two techniques: the Super Sonic Molecular Beam Deposition and the Langmuir technique. While, the porphyrinated 3C-SiC@SiO_x are grown through Vapor Liquid Solid mechanism and functionalized via "click chemistry" process.
Now a detailed description of each procedure will be presented.

2.1 - The Langmuir technique

In general, an interface is a surface delimiting two bulk phases, which shows peculiar properties often different to both separate phases. The air/water interface is the most common in the everyday experience and because of that, one of the most important to study. A constant problem is how give a precise definition of the thickness of the interface because is due to a several factors: usually ranges up to several nanometers but the presence of charged molecules can extend the interface because of the columbic interactions between them.
As discovered in the late XIX century [Strutt1899, Pockels1891], in equilibrium conditions the air/water interface always assumes the shape that minimizes its area. The reaction to any deformation of the shape of the interface region is called surface tension and, it has the dimension of a force divided by a length. The air/water interface presents a surface tension equal to 72.8mN/m at 20°C. The presence of a interfacial film on a liquid surface will affect the surface tension: in particular, the reduction of the pure liquid surface tension due the film is called surface pressure $\Pi = \gamma_0 - \gamma$, where γ_0 is the surface tension of the pure liquid and γ is the surface tension of the film-covered surface [Roberts1990]. Usually, Π for the air/water surface is of the order of some mN/m; obviously, the maximum value of Π is equal to γ_0 for water.
A fundamental tool for the scientific investigation of molecular films at the air/water interface is the Langmuir trough: the one used in our experiments is depicted in **Figure 2.1**. It consists of a container made of highly polished Teflon, a relatively common and cheap hydrophobic material, fixed to an aluminum base, equipped with a system of internal channels for water heating/cooling circulation. Two Teflon barriers can be moved synchronously onto the trough, varying the area A of the air/water interface. Teflon is employed because its hydrophobicity ensures the formation of a concave meniscus when the trough is completely filled with water. This meniscus reduces the formation of collapses and aggregates in the film, during its formation.

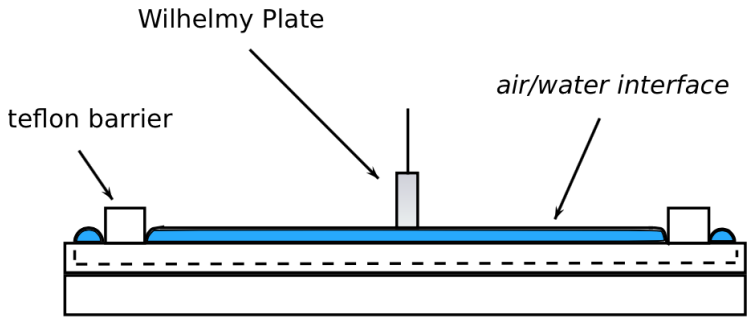

Figure 2.1 Scheme of a double barrier Langmuir trough.

The purity of the water surface is a key parameter to control the successful formation of a uniform monolayer at the interfaces, so an accurate cleaning procedure is performed before each measurement: the trough and the barriers are washed multiple times with hot water and soap, and finally rinsed with high-purity water.
The solution of the insoluble molecules we want to investigate is dispersed onto the water surface. When the solvent is completely evaporated, if molecules are enough few to not aggregate, they will be confined on the water surface in a 2D gaseous state. In case of amphiphilic molecules, characterized by hydrophilic and hydrophobic portions, we find that the first is immersed in water while the second is lifted out of the water subphase.
The surface pressure Π is measured using a device, called Wilhelmy balance, that operates through the detection of the force necessary to keep a small (1cm wide) paper/silver plate, partially immersed into the liquid, at constant height. This force has to equilibrate the sum of the surface tension, the weight of the plate and the buoyancy due to displaced water. The balance measures this force as the voltage that has to be applied to the electromagnet that holds the plate to keep constant its vertical position.
With this setup the formation of a molecular layer at the air/water interface can be easily studied by monitoring the surface pressure Π vs. the surface area A defined by the moving Teflon barriers: the so called Langmuir Isotherm. In this way, the pressure Π can be monitored as a function of sample packing, ensuring a continuous control of the sample phase transitions that may occur as the surface area is reduced.

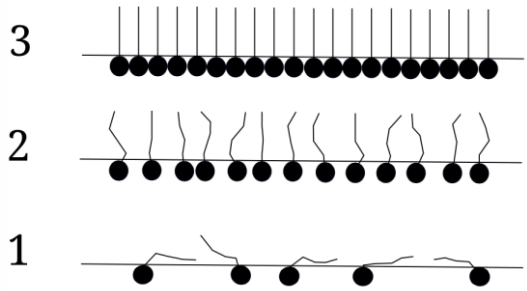

Figure 2.2 Scheme of the three main phases of lipid film, at air/water interface, during its formation: (1) gas phase, (2) liquid phase, (3) solid phase.

A general characterization, by X-ray diffraction, of the different phases that could occurs during the formation of a molecular layer at air/water interface using amphiphilic molecules as lipids (e.g. DPPC), is reported by Kaganer, Möhwald and Dutta [Kaganer1999]. They highlight many steps described as follow:

- At large values of the area, molecules do not interact with each other; the monolayer can be considered to lay in a "gaseous" state, at zero surface pressure.
- A first small increase of the surface pressure to a constant value, smaller than 1mN/m, is produced by the lifting of the hydrophobic tail of the stearic acid from the water surface (**Figure 2.2**, step1).
- At lower values of the surface area, the surface pressure starts to grow linearly, as a consequence of the onset of intermolecular interactions: the monolayer is in the so-called "liquid" phase (**Figure 2.2**, step2).
- A "solid" phase is reached by further reduction of the area, which results in a steeper increase of Π. The close packing of the molecules lifts the hydrophobic tails completely out of the subphase and orients them into an ordered phase (**Figure 2.2**, step3).
- By compressing the solid phase above a rupture point, collapses start to appear in the molecular layer, with the formation of portions of film denoted by bilayers and/or aggregates.

In addition to this rough and oversimplified categorization of the possible phases of Langmuir films, in the literature is reported that several liquid-liquid and solid-solid transitions have been observed, depending on the molecules dispersed at the interface. Besides the structural description of the different phases, is possible to describe the dynamics of lipid molecules inside the 2D layers by using the Saffman-Delbrück model [Saffman1975]: a direct extension of the Stockes-Einstein relation of diffusive motion for two-dimensional lipid systems.
In order to be useful for technological applications, Langmuir monolayers have to be transferred onto solid substrates, such as glass or silicon. Two deposition techniques (**Figure 2.3**) can be exploit:

a) the Langmuir-Shaeffer (horizontal) deposition technique;
b) the Langmuir-Blodgett (vertical) deposition technique.

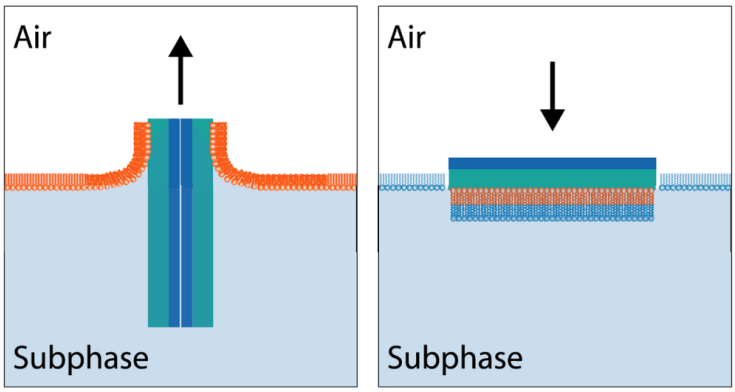

Figure 2.3 Sketch of the Langmuir-Brodgett deposition technique (left), and the Langmuir-Shaeffer deposition technique (right). The figure is taken from ref. [Prudovsky2013].

In the Langmuir-Shaeffer technique the operator holds the substrate, horizontally oriented, using a pair of tweezers; then he places the substrate in contact with the film transferring it onto the substrate as this is gently lifted up. Then, the residual water is removed using a subtle nitrogen blow. The main advantage of this technique is that it does not require any special equipment; however, the uniformity of the deposited film is strictly related to the operator skills. On the contrary, in the Langmuir-Blodgett

technique, the substrate is mounted vertically on a motorized support, then slowly immersed completely and extracted transferring a layer of molecules onto it. The Langmuir-Blodgett technique requires dedicated deposition hardware and software, but it ensures the deposition of molecular layers with high uniformity and reproducibility.
In both techniques, the substrate has to present a clean and smooth surface in order to ensure that the fewest modification will be induced on the film structure by the transfer process. Despite the highest accuracy paid in the deposition process, the first layers always suffer a certain degree of modification with respect to the structure shown at the air/water interface.
The laboratory for Molecular Nanotechnology in Parma is equipped with several custom Langmuir troughs. All troughs can be controlled either with an electronic hardware from Riegler & Kirstein GmbH (Postdam, DE) or with a custom made electronics, equipped with a PID controller for measurements performed while keeping constant the surface pressure. The whole system is interfaced with a computer, using Matlab for data acquisition.

2.2 - The Super Sonic Molecular Beam Deposition (SuMBD)

Supersonic molecular beams are originally developed for molecular scattering experiments and single molecule spectroscopy but only in recent years are used in a new approach: to growth film through the so-called Supersonic Molecular Beam Deposition (SuMBD).
SuMBD technique differs from ordinary methods for deposition of organic molecules (like Organic Molecular Beam Epitaxy, OMBE) mainly in how the molecular beam is produced. In classical beams, molecules are evaporated from a Knudsen cell and vapors effuse through the cell aperture into the deposition chamber with a Maxwell-Boltzmann distribution for the speed and the internal energy.

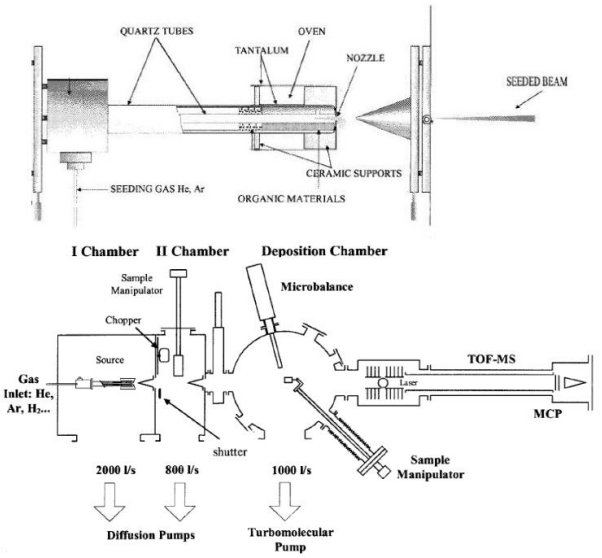

Figure 2.4 SuMBD apparatus (bottom) and the detail of the supersonic effusive cell (top) taken from [Iannotta2003].

In SuMBD, inside the cell, is maintained a greater pressure than in the deposition chamber by a carrier gas. During the expansion into the vacuum, gas and molecules mixture can reach supersonic

speed and, in the limit of low seeding, molecules can approach the carrier gas speed undergoing to a fast cooling of the internal degrees of freedom. To note that before encountering the substrate, molecular beam is defined by several skimmers and passes through successive ultra high vacuum chambers (**Figure 2.4**).
Several parameters can be controlled in SuMBD apparatus for defining the working conditions of the setup and to obtain a beam with the required characteristics:

- The internal pressure in the cell,
- The pressure in the expansion chamber,
- The temperature of the cell,
- The dilution of seeding species into the carrier gas.

The choice of the carrier gas is related mainly to the desired kinetic energy of the molecules beam impinging the substrate: different carrier gasses are suitable for SuMBD depositions as various noble gases (He, Kr etc.) or hydrogen. Heavy atoms allow to reach a low final kinetic energy (i.e. Kr=0.5 eV) while light atoms a high final kinetic energy (i.e. He=25 eV). To note that the use of hydrogen may allow a partial control of the surface reactivity during the deposition.
Moreover, besides the cooling of internal degrees of freedom, in some cases also the orientation of the molecules is achieved because these try to show their least cross section to the carrier gas. This is particularly true for long planar molecules.
A complete characterization of the SuMBD molecular beam is obtainable with time of flight molecular spectroscopy; moreover, using a quartz microbalance directly inside the growth chamber, the complete characterization of the molecular fluxes is possible.

2.3 - Vapor Liquid Solid (VLS) process for nanowires growth

The core-shell 3C-SiC@SiO_2 NWs are grown on (001) Silicon substrates by an Iron assisted carbo-thermal method. The synthesis is activated by using a Fe compound, safe for biological studies, as catalyst of the growth. In detail, the substrates are cleaned in ultrasonic bath with organic solvent and then dipped in a 0.05 M ethanol solution of Ferric Nitrate ($Fe(NO_3)_3$). Oleylamine (O7805 Aldrich) surfactant is added to the solution to favor the uniform wetting and spreading of the catalyst over the substrate. The growth is performed at atmospheric pressure in open tube configuration (**Figure 2.5**), flowing carbon monoxide as gaseous precursor and nitrogen as carrier gas at 1100°C for 30 minutes.

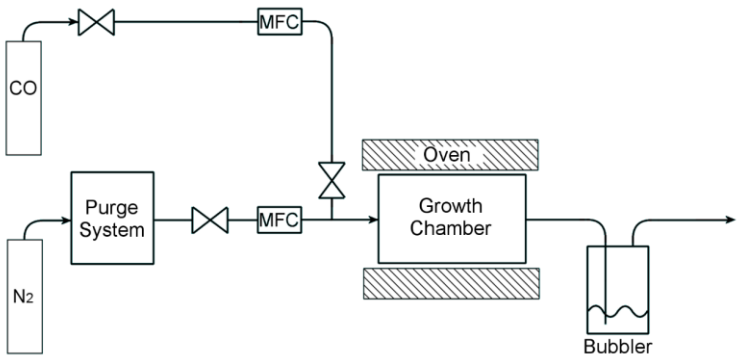

Figure 2.5 Sketch of the experimental setup for the NWs growth.

The 1D growth of the nanowires occurred according to a Vapor Liquid Solid (VLS) process and the mechanism is explainable considering three main steps:

1. CO adsorption on the silicon dioxide,
2. diffusion through the SiO_2 and
3. reaction with silicon at the interface SiO_2/Si, according to the following reaction: $4(CO)_g + 6Si = 4(SiC)_s + 2(SiO_2)_s$.

The as synthetized core-shell nanowires is subsequently proved to be cytocompatible and a detail description of the internalization

process is discussed in this work of our collaborators [Cacchioli2014].

2.4 - Nanowires functionalization process

The NWs as grown on the Si substrates are first activated with aq. HCl and then reacted with 3-azidopropyltrimethoxysilane by refluxing in toluene. Azide groups are bound to the NWs by condensation of alkoxysilyl groups with the hydroxyl groups present on the surface of the SiO_x shell.

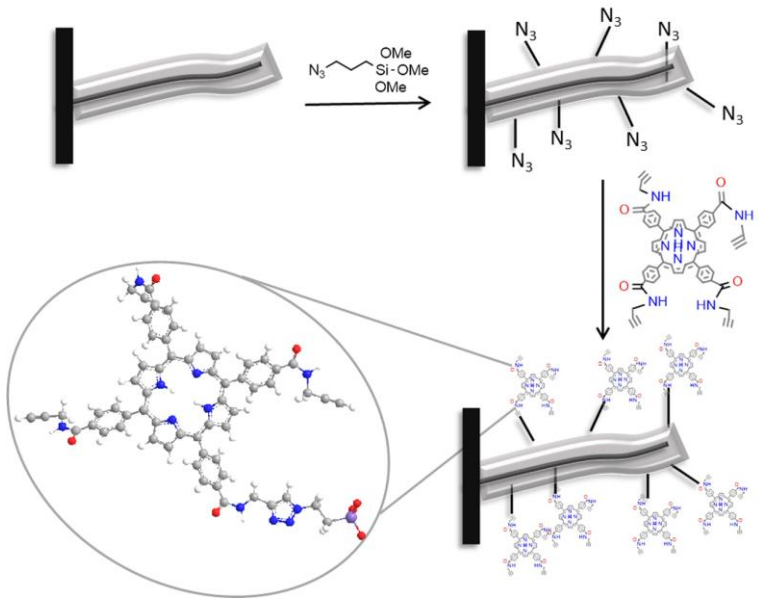

Figure 2.6 Conjugation of porphyrin with SiC/SiO_x NWs. Design of the $SiC/SiO_x/H_2TPACPP$ system: as-grown nanowires are functionalized with azide groups; the H_2TCPP porphyrin derivative containing C-C triple bonds ($H_2TPACPP$) is synthesized by converting the carboxyl groups into N-propynylamides; the nano-hybrid is constructed by bonding $H_2TPACPP$ to the NWs.

On the other side, the starting porphyrin is the tetra(4-carboxyphenyl)porphyrin (H_2TCPP) in which the carboxyl groups are converted into amides containing a short chain with a terminal alkyne functional group (carbon-carbon triple bonds) becoming the $H_2TPACPP$ porphyrin derivative (tetra(N-propynyl-4-aminocarbonylphenyl)porphyrin). Indeed, to allow an efficient

energy transfer from the nanowires to the photosensitizers, they have to be linked together and the distance between the donor and the acceptor should be less than 10 nm [Liu2008]. Therefore, the attachment of the photosensitizer to SiC/SiO_x nanowires is accomplished on the basis of reactive group-matching, that via the Huisgen 1,3 dipolar cyclo-addition reaction giving the stable triazole (1,4- and 1,5-isomers) link. The procedure employed to conjugate the porphyrin to the NWs is depicted in **Figure 2.6**. Thermal conditions, 130°C for 24h, are preferred to Cu(I)-catalyzed click-reaction to avoid the metal insertion into the porphyrin core. The samples are washed with DMSO, acetone and dried in the air. Last, the nanowires are removed (detached) from the support using an ultrasound micro-tip in acetone (Misonix Sonicator S4000, 5W) and are recovered from the solvent by ultracentrifugation (14000 Hz).

3 *Techniques for sample characterization*

The characterization of the sample structure is the first control after the sample production; in nanostructures studies, the characterization of the micro and nano structure of the sample is fundamental in order to understand if all the synthesis processes are well done. A lot of microscopy (e.g. SEM, TEM, AFM) and spectroscopic (e.g. microfluorescence, epifluorescence) techniques have been developed to investigate the micro and the nano scale. In this thesis are employed several of them: for this reason a brief overview on these is given.

3.1 - Electron Microscopies

Starting from particle/wave dualism and following the development of the first electromagnetic lens in 1926 by Hans Busch, during the 30ies the electrical engineer Ernst Ruska built and improved the first electron microscope prototype. Few years after, the first scanning electron microscope (SEM) is build by M. von Ardenne and, at the end of the decade, Siemens produced the first commercial transmission electron microscope (TEM).
In an electron microscope the source of illumination is configured on accelerated electrons in place of light. Depending on the accelerating voltage, the wavelength of an accelerated electron can be up to 10^4 times shorter than visible light photons resulting in a higher resolving power than an optical microscope. Electron microscopes are the first instruments that didn't have the problem of the Raleigh diffraction limit, as happen in the optical microscopes: for this reason they can achieve resolution up to 50 pm (TEM) instead of 200nm.
Both TEM and SEM microscopes are arranged with four main parts:

1. An electron gun, in which electrons are extracted and accelerated;
2. A column, in which electron are focused and deflected by electromagnetic lenses that play the role of optical lenses for an electron microscope;
3. A chamber (SEM) or a specimen holder (TEM), in which it is possible to place the sample to investigate;
4. Detectors, to obtain the image collecting electrons that interact with the specimen or for analyzing sub-products (e.g. light, X-rays etc.) due to the interaction between electrons and matter.

The entire instrument is maintained in ultra high vacuum (10^{-6}-10^{-11} mbar) to prevent scattering events of the electron beam by gas molecules and to avoid electric discharges.

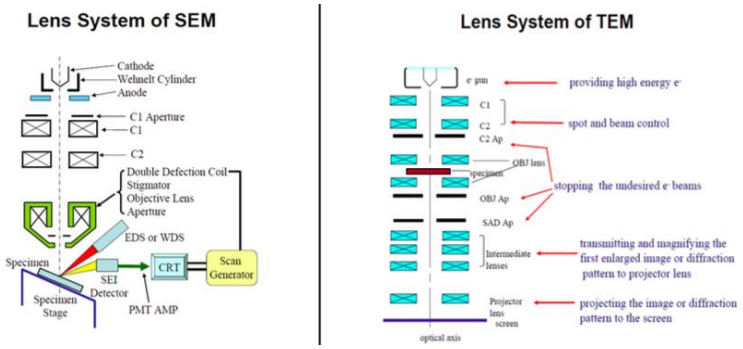

Figure 3.1 Comparison between SEM(left) and TEM(right) instrument scheme. To highlight the four main parts (from top to bottom): 1) the electron gun, 2) the column with lenses, 3) specimen chamber/specimen holder and 4) the detection system. Image taken with permission from ref. [Salviati2006].

The main differences between the two microscopes are schematized in **Figure 3.1**. Inside the SEM, the electron beam is focused and allowed to scan the specimen by using the objective lenses: all the products of interaction between the main beam and the specimen can be collected and produce an image related to the morphology (low-energy secondary electrons), to the atomic number (high-energy backscattered electrons) or to the chemical composition (X-rays).
Conversely inside the TEM the specimen is placed before the objective lens and the beam, not focused, passes through the sample: the scattering induced by the interaction with the specimen is spatially amplified by the magnification lenses and projected on the image plane where a CCD collects the intensity profile. Again it is possible to exploit the X-rays coming out to obtain informations about the chemical composition of the specimen as well as different modes of collecting electrons, to obtain the image contrast (e.g. dark field, bright field, HREM etc.).
Electron microscopes are used for a broad variety of samples: from metal and semiconductors (crystalline and amorphous) to more recently, organic and biological samples including large molecules, polymers, cells, etc (see e.g. Environmental-SEM). In general the ability to see at the nanometric scale and below has made the electron microscopes a unique tool in the research and development of nanotechnologies.

Figure 3.2 The two instruments used. (left) Zeiss SUPRA40 scanning electron microscope at Laboratory of Molecular Nanotechnologies - Parma University, (right) JEOL JEM2200FS transmission electron microscope at IMEM-CNR of Parma.

In this work, electron microscopy analyses have been performed with a Field-Emission SUPRA40 Zeiss SEM equipped with a GEMINI FESEM detection column (**Figure 3.2 left**) using different accelerating voltage (3-20 kV), and in a Field-Emission JEOL JEM-2200FS TEM microscope operated at 200 kV (**Figure 3.2 right**), placed at IMEM-CNR of Parma.

3.2 - Atomic Force Microscopy

The atomic force microscope (AFM) is one of the foremost tolls for imaging, measuring and manipulating matter at the nano-scale. Following the first experimental implementation by Binnig, Quate and Gerber in 1986 at IBM Research, the first commercially available was introduced in 1989. The AFM is a high-resolution type of scanning probe microscope, with a resolution on the order of fractions of nanometer.

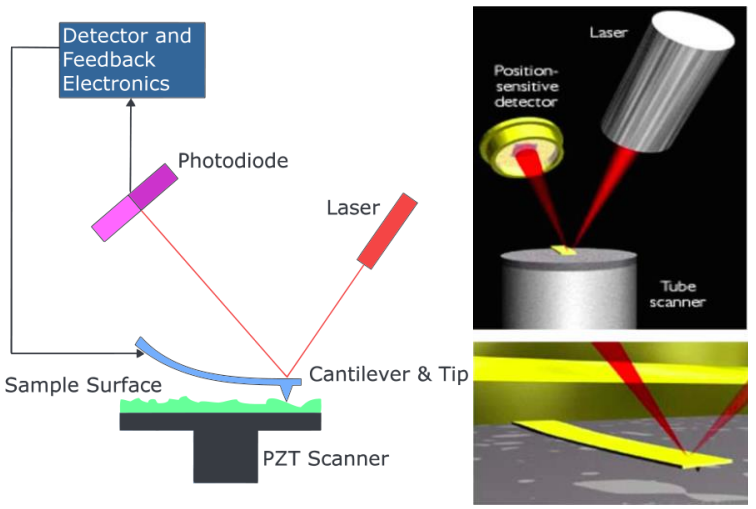

Figure 3.3 Typical scheme of an AFM instrument (left) and a cartoon of the detection system (right) taken from [Jalili2004].

The AFM core (**Figure 3.3**) is the cantilever where at its end is positioned a small tip -curvature radius of fractions of nanometer (**Figure 3.4**)- usually made by silicon or silicon nitride. Operationally, the tip is approached to the sample surface where are established the Van der Waals forces between the tip and the sample surface generating a deflection of the cantilever (the elastic constant is known) in accordance with the Hooke law. The cantilever deflection is measured by the optical deflection of a laser that is reflected from the top surface of the cantilever into a four sectors photodiode (see **Figure 3.3**). In a scanning microscope, the sample is placed on a piezoelectric tube that can be controlled for

the scan in the plane xy and, through a feedback system, for the movement along the z axis (perpendicular to the sample).

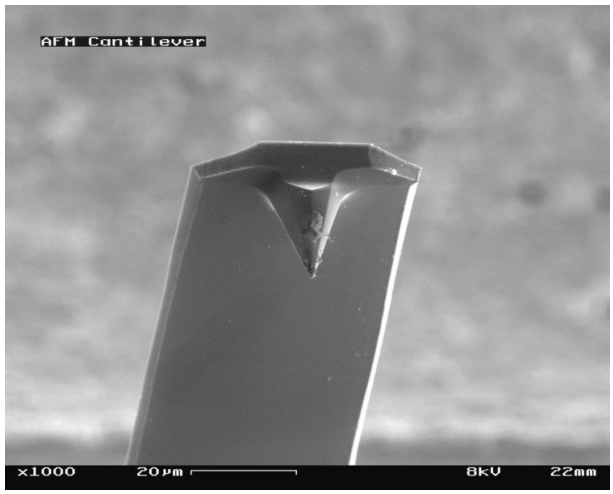

Figure 3.4 Typical SEM micrograph of a silicon AFM tip.

There are three main working modes related to different regions of the curve of interatomic force variation (**Figure 3.5**):

1. Contact mode, in which the contours of the surface are commonly measured using a feedback signal that keep the cantilever at a constant position just changing the z extension of the piezoelectric actuator. The tip works in contact to the surface under the presence of repulsive forces between the tip and the sample (**Figure 3.5**).
2. Tapping mode, in which the cantilever is driven to oscillate near its resonance frequency. The amplitude of oscillations are typically 100-200 nm and changes due to the proximity of the tip to the sample (presence of Van der Waals forces): an electronic feedback system controls the extension of the piezoelectric actuator in order to change the height from the sample surface and then to maintain unchanged the amplitude of the cantilever oscillations during the xy scan.
3. Non-contact mode, in which the cantilever is driven again to oscillate near its resonant frequency but with amplitude up to 10 nm. The tip doesn't contact the sample surface, as for tapping mode, even if the procedure to keep the amplitude oscillations constant is the same. In this mode

the AFM works using the attractive Van der Waals forces present on sample surface (**Figure 3.5**).

To remind that the tapping and non-contact modes are preferred for samples sensitive to damages due to the repetition of scans (e.g. organic film, molecules etc.). Otherwise, especially for non-contact mode, the presence of an adsorbed fluid on the surface doesn't allow to acquire the "real" morphology of the sample because it is sensitive to that layer.

Unfortunately, AFM is limited by the acquisition speed, the presence of artifacts due to the convolution of the tip shape with the sample morphology, drifts of the piezoelectric elements, hysteresis problems due to the piezoelectric actuator and the limited dimension of the maximum scan area (100x100 μm).

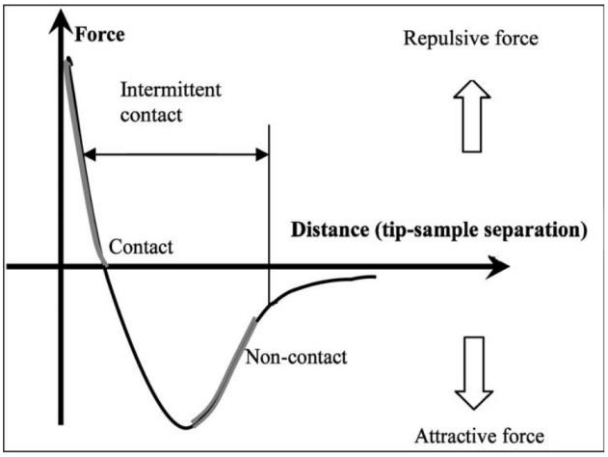

Figure 3.5 Interatomic force variation versus distance between AFM tip and sample surface, taken from [Jalili2004].

Conversely, the AFM is extremely versatile because it works in ambient condition and on all kind of samples, even insulators, without a particular preparation. Farther, it can acquire a lot of different information as the shape of magnetic domains (MFM) or electric fields (EFM) just changing the kind of tip used. Last but not least, it acquires the real 3D profile of the sample and not just a 2D projection as for SEM and TEM.

The samples morphology in this thsesis is studied by the AFM in contact mode, Autoprobe CP-R, Thermomicroscope (**Figure 3.6**);

typical topography images are acquired on a 10x10 μm area with a 256x256 sampling points.

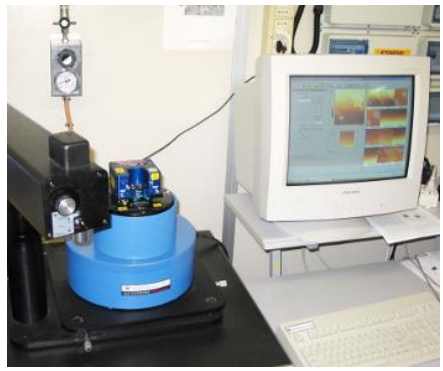

Figure 3.6 The AFM used for the measurements.

3.3 - Microfluorescence Setup

With the aim to measure the fluorescence spectra of a single molecules layer and of very low concentrated fluorescent solutions, we built ad-hoc microfluorescence setup, after all able to acquire also Raman spectra, around a TRIAX320 Horiba/Jobin-Ivon single pass monochormator (**Figure 3.7 center**).
The monochromator is equipped with two gratings:

1. 600 gr/mm for acquisition on large spectral ranges (useful for microfluorescence)
2. 1800 gr/mm for high resolution acquisitions (useful for micro-Raman).

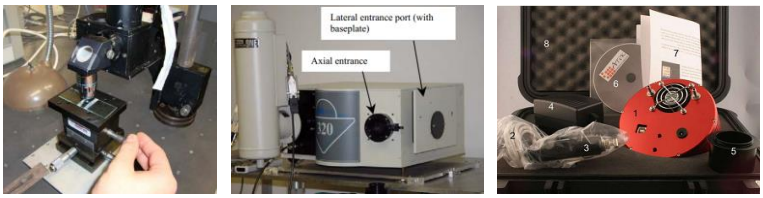

Figure 3.7 The three main parts of the ad-hoc microfluorescence setup. The microscope head (left), the Triax320 monochromator (center) and the Atik CCD camera (right).

It is coupled with a homemade microscope head (**Figure 3.7 left**) capable to mount various available objectives (e.g. from 5x up to 100x) among which a useful Olympus ULWD50 long focal 50X objective (N.A. 0.55): the most employed in the measurements because of its adaptability with different samples environments and of its brightness. Besides the objective, the microscope head holds a sliding beam splitter that allows acquiring the sample image where are performed the measurements (**Figure 3.8**). Furthermore, the microscope head can be coupled with the monochromator with or without optical fibers giving a large versatility of employment.

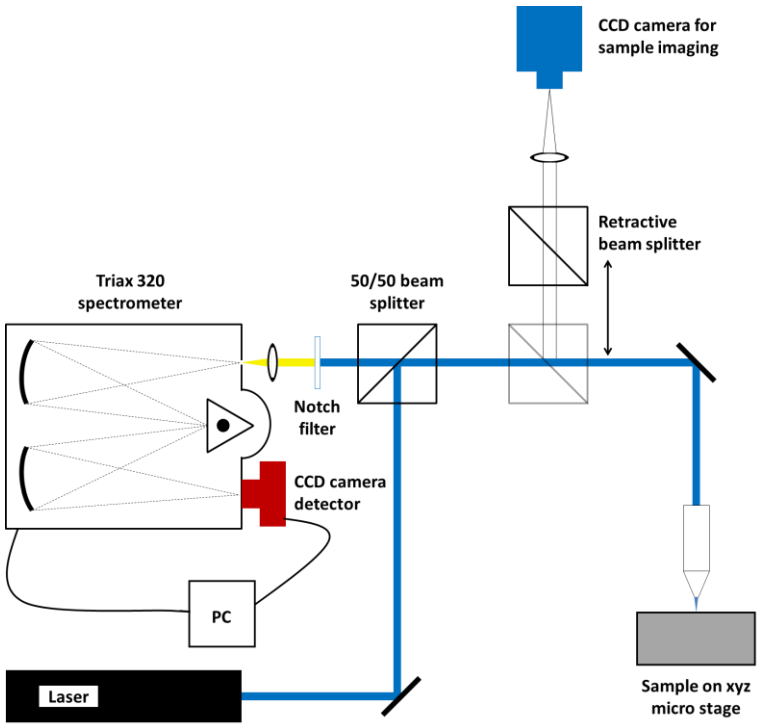

Figure 3.8 Ensemble scheme of the microfluorescence setup used for the measurements.

The entrance of the microscope head is designed to be coupled again -with or without optical fibers- to a large variety of light sources among which lamps and different kind of lasers. In our laboratory are available three Diode Pumped Solid State (DPSS) lasers covering the spectral range of excitation between 380nm and 690nm. The entering beam is guided, by a beam-splitter, to the objective that, in backscattering geometry, collects the fluorescent light: an edge filter, matched with the excitation line, filters the laser light before the monochromator entering slits.
The fluorescence light is then divided in all its components inside the monochromator and revealed by an Atik-11000 peltier-cooled CCD camera (**Figure 3.7 right**) installed matching the focus plane of the monochromator exit with the sensor window of the camera. This camera is originally made for amateur astronomers but because possesses forefront characteristics, in terms of sensitivity and low electronic noise, is adaptable for science employments:

farther is 10 times cheaper then a commercial CCD detector for science.
In addiction we developed, in Matlab® computing environment, an all-in-one software interface, through which is possible to control the positioning of the gratings turret, the aperture of the monochromator slits an all the acquisition parameters of the CCD camera.

3.3.1 - Starting up the instrument

Before the assembly of the CCD camera on the TRIAX320 monochromator, we checked the operation of the sensor.

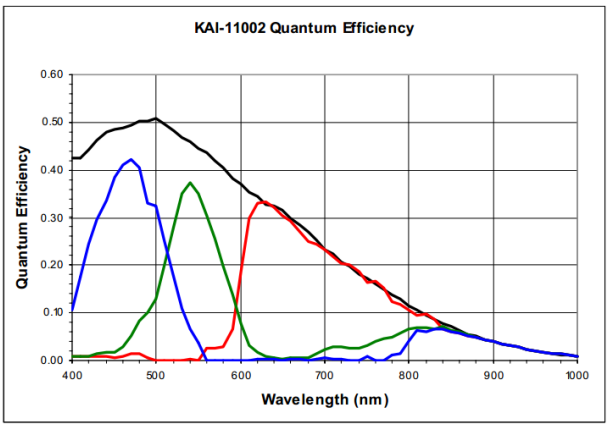

Figure 3.9 Efficiency profile of the Kodak-KAI11002 sensor installed in the Atik CCD camera. The black line is the profile for the B/W version.

In **Figure 3.9** is depicted the efficiency profile of the Kodak-KAI11002 that equips the Atik camera. In the visible range (400nm - 700nm) the efficiency profile has the shape of a broad peak, centered at 500 nm, it ranges from 20% up to 50%. Because, in fluorescence and Raman measurements, the relative intensities of the peaks are one of the key parameters to study, all acquired spectra are corrected for the sensitivity of the CCD just dividing the acquired intensities by the normalized efficiency at the same spectral position.

Farther is performed a characterization of the dark noise of the device. We acquired three images, with the sensor window close by its stopper, at the maximum cooling temperature of the CCD (-38° C below the room temperature) but changing the exposure time. The mean on the columns provides the profile in **Figure 3.10 top panel**, where the mean counts of each column is plotted vs. the pixels index: the green line corresponds to 100 seconds of exposure, the red line to 1 second and the black to 1 millisecond. To note that, in the range of exposure times checked, the increase of the mean signal due to the acquisition electronics is negligible proving that the camera can acquire for very long exposure times before to go to a self-saturation.

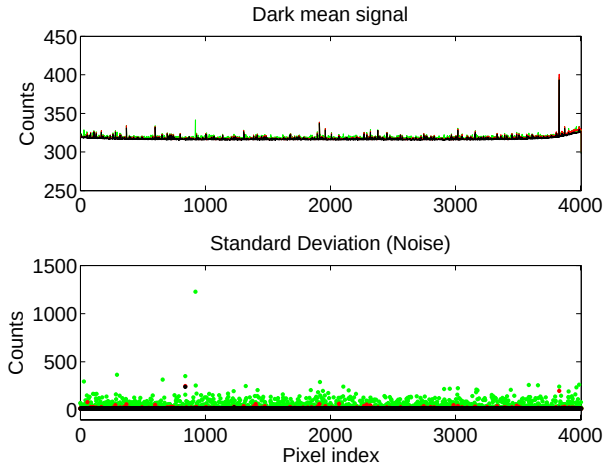

Figure 3.10 Dark mean signal (top) and the related noise (bottom). The green line (or dots) is related to 100 seconds acquisition, the red line (or dots) to 1 second and the black line (or dots) to 1 millisecond.

Focusing on the standard deviation, the noise on dark signal (**Figure 3.10 bottom panel**), it is appreciable the increase for the 100 seconds of exposure (green dots) but also in 1 second acquisition (red dots) there is a change respect to the 1 millisecond points (black dots). For this reason, each fluorescence or Raman spectrum is subtracted every time with a dark spectrum acquired without the excitation light on the sample but with exactly the same parameters. This subtraction provides two corrections: i) the removal of the baseline (mean value of the dark signal) due to the

acquisition electronics and, ii) the partial removal of the statistical noise superimposed to the spectra.

3.3.2 - *The calibration*

After the assembly of the CCD on the monochromator, is performed the calibration of the system employing the characteristics lines of various gas lamps (e.g. Cd, Hg, He, Na etc.) that cover all the visible spectral range.

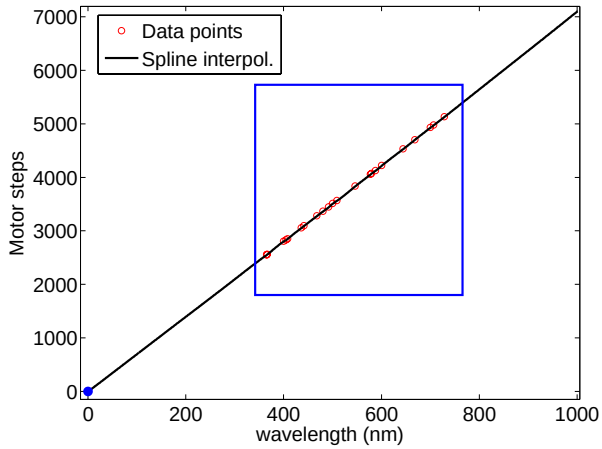

Figure 3.11 Calibration curve of the microfluorescence setup. Red open circles are obtained with the gas lamps employed and the blue filled circle is the zero order reflection of the grating. The black line represents the spline extrapolation, see text for more details.

In **Figure 3.11** is shown the calibration curve of the grating 600gr/mm. This curve links the motor steps of the gratings turret to a specific spectral position in nanometers. Each red empty circle in the blue box corresponds to an emission line of one gas lamp, the blue filled circle is the reflection at order zero of the grating while the black line is the spline extrapolation. It extends the validity of the calibration curve for wavelengths that are outside the blue box. To note that, this is allowed because the calibration shows a linear law and moreover, the system is built to work only in the visible

region thus an accurate positioning in the other spectral regions is unnecessary.

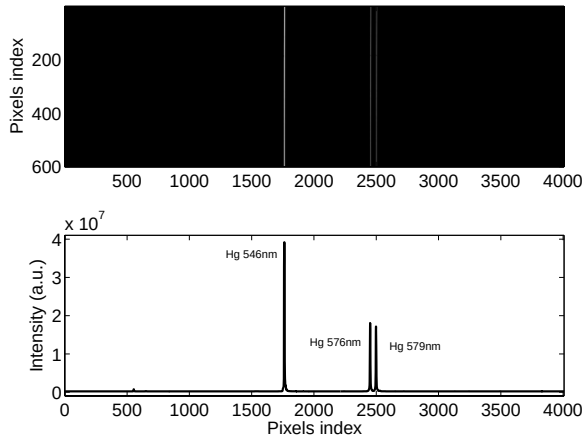

Figure 3.12 An image (top) acquired by the CCD camera and the related spectrum (bottom) of the characteristic lines of an Hg gas lamp.

This calibration curve is implemented in the all-in-one software developed in Matlab® computing environment: this allows acquiring a picture with the CCD (**Figure 3.12 top panel**), to generate the spectrum (**Figure 3.12 bottom panel**) and, through the calibration curve, to label the peaks with the correct wavelengths.

3.3.3 - Setup employed for acquisitions

Fluorescence spectra in this thesis have been acquired with an excitation light provided by a DPSS laser (CNI-Laser MBL-III-473-100-3 emission wavelength 473nm, 100 mW maximum power, 1.2 mm spot size, beam divergence <1.5mrad) filtered with a 10nm band-pass filter (Semrock FF01-473/10-25). The microscope head has been equipped with an Olympus ULWD50 long focal 50X objective (N.A. 0.55). Fluorescent light, collected in backscattering geometry, has been filtered with a 473nm edge filter (Semrock BLP01-473R-24). Typical integration times ranged from 1 to 30 seconds with maximum power density on the samples 1-2mW/μm^2. No photobleaching effect is observed in these conditions.

3.4 - Epifluorescence Microscopy

The epifluorescence microscope allows to acquire the fluorescence images of the surface of a broad range of samples: from depositions onto solid substrates to films at air/water interface labeled with fluorophores.

Figure 3.13 The epifluorescence inverted microscope used for measurements.

In this thesis, epifluorescence measurements are performed using a Nikon Ti-Eclipse inverted microscope equipped with an high-sensitivity Andor Clara camera, an high power Hg lamp "Intensilight", two block-sets (FITC and TRITC) for epiflorescence analysis in different spectral regions together with different objectives, including 60x (N.A. 1.4) and ULWD 50x (WD 10mm), to accommodate different sample environments. The instrument is shown in **Figure 3.13**.

4 Techniques for physical investigation

4.1 - Mechanical properties

Two complementary techniques are used in this thesis for measuring the mechanical properties of Langmuir films: the oscillating barriers technique and the oscillating needle technique. In particular, both the compression (ε) and shear (G) complex moduli as functions of surface concentration are investigated. The combination of these two techniques is extremely newsworthy because both operate on the macroscopic scale and on the same temporal scale.

4.1.1 - Oscillating barriers

The oscillating barriers technique exploits the fact that uniaxial compression can be decomposed in isotropic compression and shear deformation. This results in the difference in the surface pressure measured by perpendicular Wilhelmy plates when a dense Langmuir film is subjected to uniaxial compression [Cicuta2005]. In particular, applying a sinusoidal uniaxial deformation, under suitable conditions [Brooks1999] one can extract both the in phase (real) and the out of phase (imaginary or dissipative) parts of the mechanical response function.

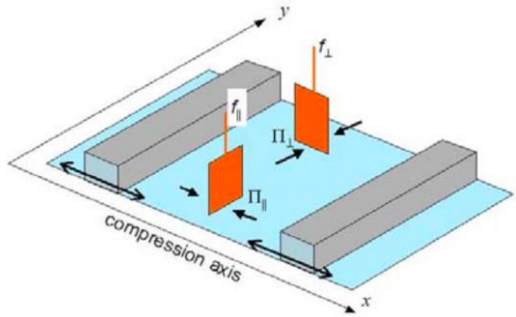

Figure 4.1 Scheme of the oscillating barrier technique, taken from [Cicuta2005].

The experimental setup is based on a Langmuir trough (custom made, size 10x40 cm², with KSV Nima mechanics) equipped with two identical Wilhelmy balances, which monitor the evolution of the surface tension (and hence the phase and amplitude of their oscillations $\Delta\Pi_{||}$ and $\Delta\Pi_{\perp}$) while the area available to the film is oscillated by the synchronized movement of the two barriers, operated at a typical frequency of 0.5 Hz (**Figure 4.1**).
From the area A_0, its oscillation ΔA, and the phase lag ϑ we obtain the complex mechanical moduli:

$$G = G' + iG'' = A_0 \left(\frac{\Delta\Pi_{\parallel}}{\Delta A} - \frac{\Delta\Pi_{\perp}}{\Delta A}\right) e^{i\vartheta} \qquad \text{Eq. 1}$$

$$\varepsilon = \varepsilon' + i\varepsilon'' = A_0 \left(\frac{\Delta\Pi_{\parallel}}{\Delta A} - \frac{\Delta\Pi_{\perp}}{\Delta A}\right) e^{i\vartheta} \qquad \text{Eq. 2}$$

This analysis assumes linearity in the response of the system to the external perturbation: this assumption is limited to the diluted regimes.

4.1.2 - Oscillating needle

The oscillating needle technique, which imposes a pure shear perturbation, is employed to characterize the mechanical shear. The oscillating needle rheometer used is an adapted version of the instrument proposed years ago by Fuller and co-workers [Brooks1999] and is described in detail in [Orsi2011].

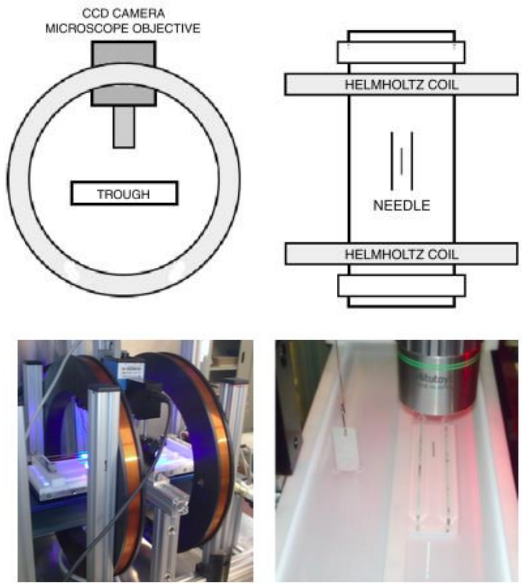

Figure 4.2 Sketch of the rheometer design (top) and the image of the entire instruments employed (bottom left) besides a particular of the measurement region [Orsi2011].

In brief, a stainless steel needle (1 cm long, 0.3 mm radius), magnetized to saturation, is placed at air/water interface of a Langmuir trough inside a tunnel built with two parallel glass plates (see **Figure 4.2**). Two Helmholtz coils are located around the Langmuir trough with a static current applied. The current that

flows inside the coils generates a static magnetic field that aligns the needle along the axis of the coils, in its equilibrium position. Applying a sinusoidal current to one of the coils, is produced the oscillating field gradient that moves the needle. Now, a fast CCD camera measures the amplitude and the phase of the oscillations of the needle and the mechanical shear modulus G is then obtained with:

$$G = G' + iG'' = \frac{\sigma}{\gamma} e^{i\vartheta} \qquad \text{Eq. 3}$$

where σ is the stress exerted by the needle, γ is the resulting strain, and θ is the phase difference between the oscillations of the magnetic field and of the needle.

4.2 - X-ray Photon Correlation Spectroscopy (XPCS) technique

X-ray photon correlation spectroscopy (XPCS) technique allows to access an otherwise inaccessible region of the space-time plane corresponding to localized and slow motions, e.g. taking place on the nm-scale and on the $10^{-3} - 10^{2}$ second time scales (**Figure 4.3**).

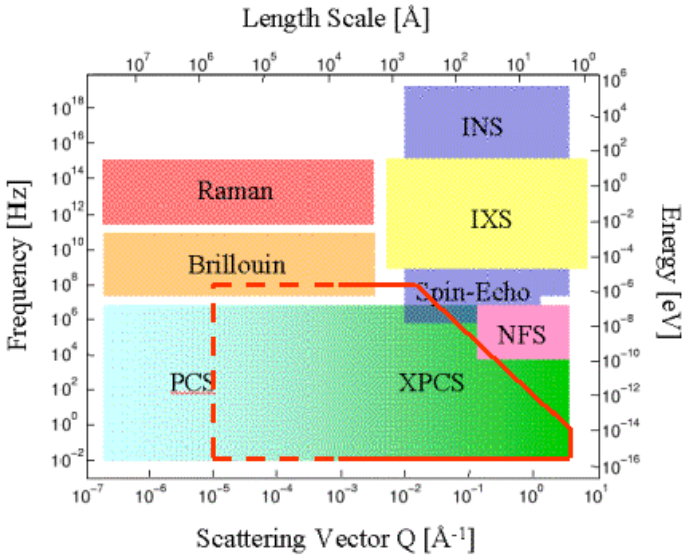

Figure 4.3 The field of application of XPCS technique in the space-time plane.

It is the extension of photon correlation spectroscopy (also called dynamic light scattering, DLS) to the X-ray regime. The X-rays speckle patterns have been observed for the first time at the National Synchrotron Light Source at Brookhaven National Laboratory by Sutton, Mochrie and co-workers in the 90s [Suttun1991, Sutton2008]. In comparative analogy with DLS, it includes several advantages as:

- it is possible to study matter on the interatomic length scale, since it is possible to reach higher values of the exchanged momentum q;

- it is possible to study optically opaque samples since multiple scattering, one of the main difficulties in DLS, is negligible.

Its birth required many nontrivial experimental issues to be solved: mainly the production of a clean X-ray beam of sufficient coherence and intensity, and the detection of the scattered intensity.
With visible light, coherence is obtained using a laser source. Aside of X-ray Free Electron Lasers, every other X-ray source emits transversely incoherent light. In this case, as for X-ray undulators, coherence is obtained from an highly collimated and monochromatic beam by using micron-sized pinholes: in this case the intensity of coherent light is directly proportional to the brilliance of the source. XPCS is currently feasible at third generation synchrotrons, since they produce X-rays beams several order of magnitudes more intense than the ones produced by smaller synchrotrons or laboratory sources.
For studying gold nanoparticles 2D network formation and DPPC-silica nanoparticles Langmuir films, the multi-speckle GI-XPCS experiments are performed at the beamline ID10 of the European Synchrotron Radiation Facility (ESRF) in Grenoble, France. An incident X-ray beam with an energy of 8 keV (λ = 0.155 nm) is selected from the undulator radiation by a Si(111) monochromator scattering in vertical geometry (energy bandwidth $\Delta E/E \sim 10^{-4}$). The beam is then focused with Be compound lenses while higher harmonics are suppressed by two Si mirrors. The resulting incident flux of coherent monochromatic X-rays photons on the sample, higher than 10^9 photons/s, is obtained using a 10x10μm^2 pinhole (placed ~0.18 m upstream of the sample), for an electron current of 100mA injected in the storage ring of the synchrotron.

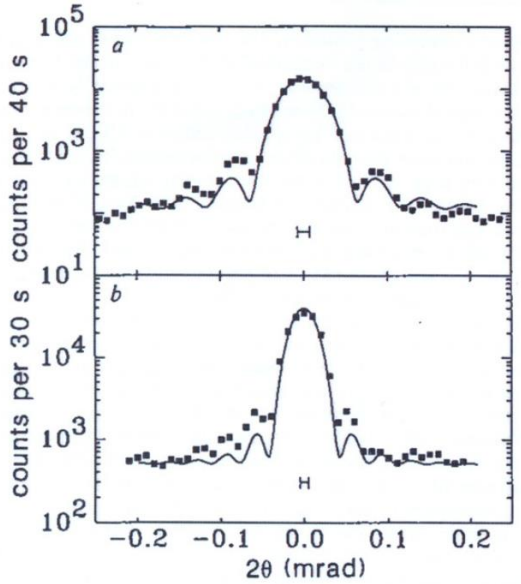

Figure 4.4 Fraunhofer diffraction from (a) 2.5µm and (b) 5µm diameter pinholes [Sutton1991].

The parasitic scattering (**Figure 4.4**), due to Fraunhofer diffraction, produced by the beam-defining slits is removed by carefully adjusting a set of guard slits a few centimeters upstream of the sample. The beam is reflected on the liquid surface at a grazing incident angle of the order of 0.12°, which is about 90% of the critical angle for total reflection on the water surface at this photon energy.

Two-dimensional X-ray scattering speckle patterns are recorded by using a photon-counting area detector (Medipix, 256×256 pixels, 55µm pixel size [Ponchut2011]) placed at a distance of 3.3 m from the sample. The exposure time of the Medipix detector is chosen to be long enough to warrant a reasonable signal-to-noise ratio, 10-100 ms in our case. To avoid unnecessary irradiation of the sample, a fast shutter, synchronized with the area detector, is placed upstream of the sample. Sets of up to 20000 images are collected for different sample concentrations with different exposure times.

4.2.1 - Setup for film at air/water interface

Within this thesis, we have performed some XPCS measurements on interfacial layers, i.e. in grazing incidence (GI-XPCS). While XPCS is already quite commonly exploited in the study of slow dynamics in the bulk, this is not the case for interfacial dynamics, perhaps due to some technical difficulties associated with interfaces.
To perform a GI-XPCS experiment at air/water interface a custom-made Langmuir trough with a single moving barrier (maximum surface 418x170 mm^2) is installed on the sample diffractometer (**Figure 4.5**). It is relatively large, to minimize meniscus effect on the scattered signal, but this imply a relatively low compression ratio 3:1.

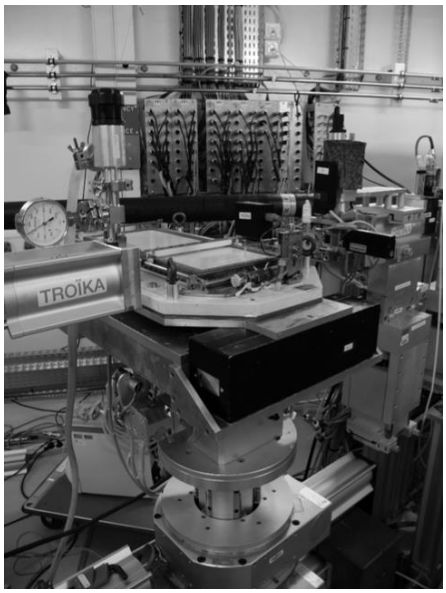

Figure 4.5 A photo of the Langmuir trough used for XPCS measurements.

The water level has been adjusted so that a very small -almost absent- meniscus is present. The setup is mounted on an active anti-vibration support and provided with a plastic enclosure, under which a helium atmosphere is created in order to minimize parasitic scattering from air and at the same time reduce risks of beam-induced damage. KSV-Nima Wilhelmy balance and

electronics are used to control the trough, measure the surface pressure and the trough's area during GI-XPCS measurements.
The X-ray beam (size 10x10 μm²) is directed towards the water surface with an angle of the order of a = 0.12°, leading to a total footprint

$$10\mu m \times \frac{10\mu m}{\sin(0.12°)} = 10\mu m \times 4.7mm = 4.7 \cdot 10^4 \mu m^2.$$

Again, the detector has been positioned in correspondence of the reflected beam. The diffraction pattern arising from a Langmuir film is anisotropic; hence the pixels that compose the detector area are divided into a grid of squares. Each square is then characterized by a parallel and a perpendicular component of the exchanged momentum, $q_{||}$ and $q_{\perp}$, respectively parallel and perpendicular to the water surface, as indicated in **Figure 4.6**.

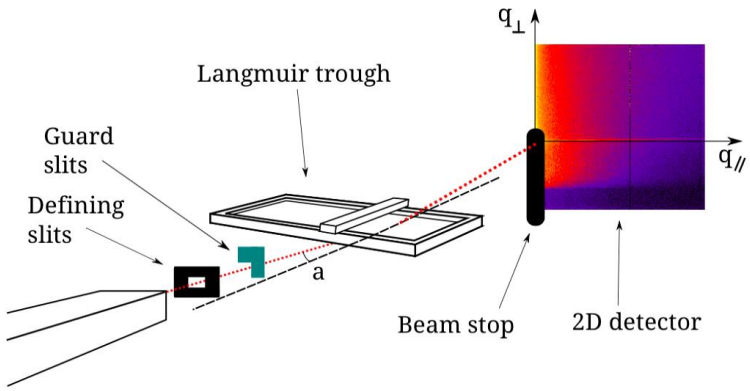

Figure 4.6 Scheme of the GI-XPCS setup for measurements at the air/water interface.

4.3 - Radiotherapy: Setup and basic concepts

In 1953 at the Hammersmith Hospital (London, UK) the first patient is treated with a linac-based radiation therapy.
The linear accelerator for radiotherapy treatments is a machine able to generate collimated electron and photon beams that are allowed to impinge on a target volume: normally the used beam energy is 6 MeV.

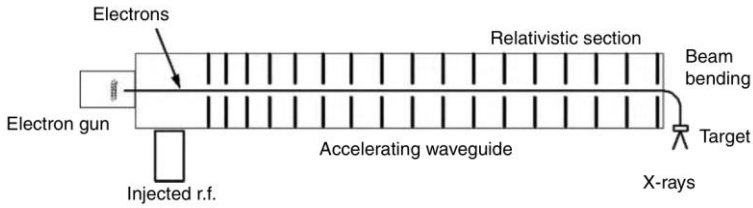

Figure 4.7 Scheme of the linear accelerator for radiotherapy treatments. From left to right, electrons are generated by an electron gun, injected in the accelerating waveguide where are accelerated before reaching the high Z target. Taken from [Mayles2007].

Because of the complexity of the setup of a medical linear accelerator, we report in brief the components and the operation but is possible to find a complete overview of the system in the Handbook of Radiotherapy Physics by Philip Mayles [Mayles2007]. In particular the core of the setup, schematized in **Figure 4.7**, is based on three main parts:

1. The microwave power source made with a Magnetron or with a Klystrons: it provides the radiofrequency needed for pulsed operation in the 2-10 MW power range.
2. The electron gun is the source of electrons that have to be accelerated: they are generated from a heated cathode by thermionic emission thorough the application of a pulsed voltage of about 10 kV to the filament, resulting in an instantaneous beam current of the order of milliamps.
3. The accelerating waveguide where electrons, generated by the electron gun, are accelerated at relativistic speed: it is a long cylindrical tube containing a series of circular baffles.

Bunches of electrons, produced in the gun, are injected into the guide in synchronism with pulsed microwave radiation and are carried down the guide in a manner analogous to riding the crest of a wave.

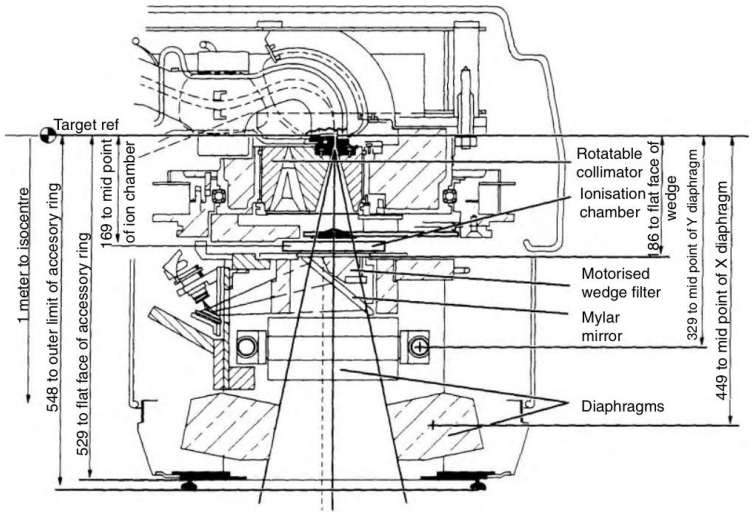

Figure 4.8 The head assembly of a linear accelerator for radiotherapy treatments. Taken from [Mayles2007].

The machine works in two operational modes: in electrons mode and in photons mode. In the first case the high energy electron beam, that come out to the accelerating waveguide, can be directly used for therapy. In the latter case, electron are focused onto a high atomic number target and the energy loss, following the impact, produces a bremsstrahlung emission of energetic X-rays. Because the energy of the electrons is in the MeV range, this emission is directed in the forward direction.
In 6 MeV machine the target is located inside the head assembly (**Figure 4.8**) after a magnetic sector that produces a beam bending of 90°: the length of the accelerator tube is great and makes impracticable other geometries. Furthermore, an advantage in the use of the magnetic sector is to filter in energy the electrons and to obtain a quasi-monochromatic beam. In addition to the target, the head assembly encloses many parts necessary for having a uniform and stable exposure field on the target to treat (i.e. flattening filters, monitor chambers, collimator etc.).

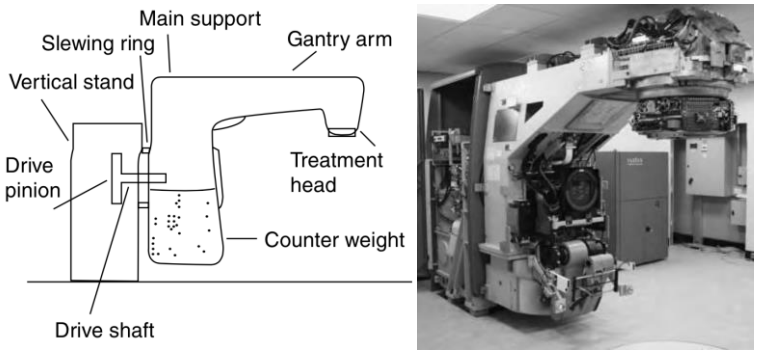

Figure 4.9 Scheme of the Gantry arm (left) and a picture of a Varian2100C gantry without its covers (right). The accelerating waveguide is on top of the arm before the treatment head assembly, while the klystron can be seen at the extreme left of the picture [Mayles2007].

The head, the electron gun and the accelerating waveguide are placed inside the Gantry, a big arm that can rotate 360° around the patient enabling the treatment of regions all around the body (**Figure 4.9**). Finally, the entire linear accelerator is located inside a room, shielded against the emission of diffuse X-rays, called Bunker.

4.3.1 - The dose construction

One of the key parameters for the success of radiotherapy treatments is the accurate determination of the absorbed dose. This requires some explanations about the energy release produced, by the incoming X-rays beam, at the point of interest. Radiation dosimetry comes in handy with methods for a quantitative determination of energy deposited in a given medium by directly or indirectly ionizing radiations. Here we report only the dosimetry key point, the dose construction: a complete overview about all the quantities and the mechanisms involved are possible to find in [Mayles2007].
To investigate in detail the phenomenon of dose construction, two quantities have to be defined. The first is *kerma*: an acronym for

Kinetic Energy Released in Matter. It quantifies the average amount of energy transferred from an indirectly ionizing radiation to a directly ionizing radiation without concern as to what happens after this transfer.
For photons, the energy is released to the medium in a two-stage process. In the first stage, primary photons transfer their energy to secondary charged particles (electrons) through various photons interactions (the photoelectric effect, the Compton effect, etc.). In the second stage, electrons transfer their energy to the medium through atomic excitations and ionizations. In this framework, the *kerma* is defined as the mean energy transferred from the photons to the electrons in the medium $d\overline{E_{tr}}$ per unit mass dm, Eq. 1:

$$K = \frac{d\overline{E_{tr}}}{dm}$$

The total *kerma* is therefore usually divided in two components: the *collision kerma* K_{col} and the *radiative kerma* K_{rad} through the following expression, Eq. 2.

$$K = K_{col} + K_{rad}$$

The *collision kerma* is the part of *kerma* which leads to the production of electrons that dissipate their energy as ionizations. While the *radiative kerma* is the part that leads to the production of secondary photons, as the secondary charged particles, that slow down and interact in the medium (bremsstrahlung).
A frequently used relation between *collision kerma* K_{col} and *kerma* K may be written as follows, Eq. 3:

$$K_{col} = K(1 - \bar{g})$$

where the fraction lost through collisions is (1-$\bar{g}$) and $\bar{g}$ is a factor, called radiative fraction, that represents the average fraction of the energy that is lost through radiative processes. The radiative fraction also depends on the material considered: high values of $\bar{g}$ are related to high Z materials.

The second quantity is the *absorbed dose*, defined in the second stage when electrons transfers energy to the medium through atomic excitations and ionizations.
It is described as the mean energy $\bar{\varepsilon}$ imparted by ionizing radiations to a medium of mass m in a finite volume V by, Eq. 4:

$$D = \frac{d\bar{\varepsilon}}{dm}$$

The energy $\bar{\varepsilon}$ is the sum of all the energies which enter the volume of interest minus all the energies that leave that volume, taking into account any mass-energy conversions within the volume.
Generally, the transfer of energy (*kerma*) from the primary photon beam to the electrons, at a particular location, does not lead to the absorption of energy by the medium (*absorbed dose*) at the same place. This is due to the finite disexcitation length of the released electrons by interactions with photons. Usually, the *absorbed dose* can be related to the *collision kerma* through the ratio, Eq. 5:

$$\beta = \frac{D}{K_{col}}$$

Since the main part of photons escapes from the volume of interest, this ratio is frequently $\beta \approx 1$.
Figure 4.10 illustrates the relation between *collision kerma* and *absorbed dose* under build up conditions, under charge particles equilibrium (CPE, right part of **Figure 4.10**) and under transient charged particle equilibrium (TCPE, left part of **Figure 4.10**).
Initially, the electrons' flux (produced by the primary photon beam) and the *absorbed dose* increase (see build up region), as a function of depth. The build up region is explainable considering that the primary photon beam generates electrons together with its flow and these electrons release their energy to the medium along their disexcitation pathway. Therefore, going in depth, more and more electrons are generated and can release energy; this increases the *absorbed dose* up to the maximum dose d_{max}. Now, if there are no photons attenuation or scattering in the medium, but yet production of electrons, a hypothetical situation would occur

(**Figure 4.10 right**): the buildup region (with $\beta < 1$) will be followed by a region of complete CPE, where $D=K_{col}$ (i.e. $\beta = 1$).

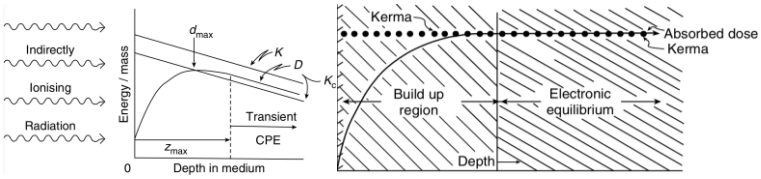

Figure 4.10 The dose construction. (left) The real case in which there is attenuation of the photons in the medium and (right) the ideal case in which the CPE is achieved after the build up region, taken from [Mayles2007].

However in a more realistic situation, with photons attenuation and scattering in the medium, exists a region of TCPE (**Figure 4.10 left**) where there is an essentially constant relation between *collision kerma* and *absorbed dose*.

4.3.2 - Varian DHX at Parma Hospital

To test the singlet oxygen production and the effectiveness of this treatment in vitro on cells, with the help of Dr. Giovanna Benecchi, we exposed the samples to the 6MeV X-rays produced by the linear accelerator (Varian DHX, **Figure 4.11**) available at radiotherapy department of Parma Hospital: the setup is commonly used for the clinical treatment of tumors on patients. Typically, Petri dishes or multi-well plates or cell culture dishes to be irradiated are placed on the couch over a 30 x 30 x 1.5 cm plastic water slab to construct the dose (build up region). The gantry of the accelerator is rotated by 180° and the irradiation field is set to 10 x 10 cm^2, with a source-skin distance (SSD) of 1 m. The dose rate is kept constant to 600 monitor units per minute, i.e. 6 Gy/min, for all the experiments.

Figure 4.11 The linear accelerator Varian DHX available at radiotherapy department of Parma Hospital.

5 *Nanosystems for biomedical applications*

As already mentioned, the BioNiMED project is focused on the development of a hybrid nanosystem based on SiC@SiO_x core-shell nanowires functionalized with porphyrin. Because of the complexity of the proposed nanosystem and the key role of the interactions between nanowires and porphyrin molecules, the first step is to study a model system in which porphyrin depositions are carried out on silicon wafers with native oxide on top.

5.1 - The porphyrins photosensitizers

A brief introduction to porphyrins is useful to deeply understand the importance of them in this thesis.
Porphyrins are a class of π-conjugated organic molecules having as base unit the pristine molecule, shown in **Figure 5.1 left**: the simplest porphyrin. Basically it's a heterocyclic macro-cycle derived from four pyrroline subunits interconnected via their α carbon atoms through methine bridges (=CH-). This skeleton makes an open structure where external groups can be bonded in the meso positions or pyrrole rings can be substituted. The four nitrogen, constituting the pristine core, may be split in two sets: one constituted by the N atoms (two) carrying a lone pair in the molecular plane and another one that include N atoms directly linked to H atoms (metal-porphyrins). As consequence of the possible de-protonation of these two H atoms, a square planar coordinative site is created and may be occupied by a metal ion. If the site is not occupied the porphyrin is called free-base. Porphyrins are commonly used by nature for various purposes in vegetal and animal organisms: well known examples are Chlorophyll in plants and Heme group (**Figure 5.1** right) in red blood cells.

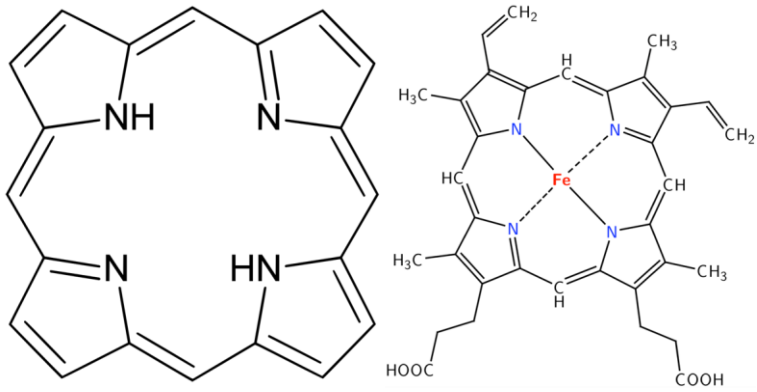

Figure 5.1 The pristine macro-cycle (left) and the Heme B group of hemoglobin (right).

This peculiar and versatile structure allows the control of the reactivity as well as the electronic and optical properties of the molecule through molecular engineering, opening the possibility to a broad range of applications. In particular, the coordinative capabilities of these molecules, together with the possible energy interaction with the oxygen molecule, enables their use for catalysis [Simonneaux2006] and photo dynamic therapy [Castano2006, Hudson2005]. Furthermore the tunability of the optical absorption and fluorescence makes these molecules promising for energy production in hybrid solar cells [Planells2008]. Extensive studies of porphyrins as active materials for sensing devices, in gaseous or liquid environments, have been also carried out leading to the development of sensor array architectures based on different metal-porphyrins [Rakow2000].
In **Figure 5.2** are shown the two porphyrins derivative employed in this thesis. The H_2TTP(F) porphyrin (left) is synthetized by the substitution of the H atoms with F atoms in all the four phenyl rings while the addiction of four carboxyl groups in H_2TCPP porphyrin (right) tunes the reactivity of the molecule allowing its use in wet chemical functionalization methods as is explained in section 2.4.

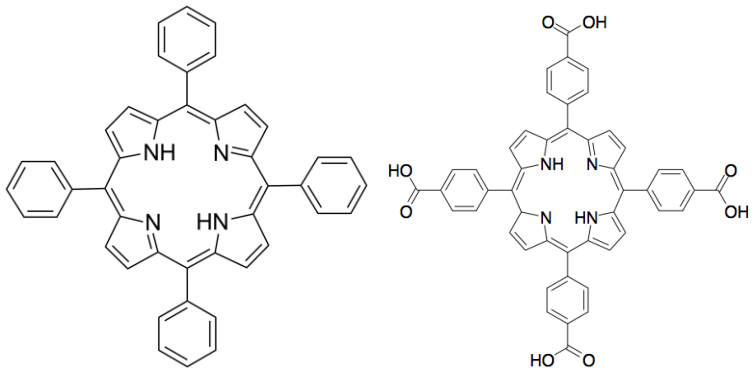

Figure 5.2 The H_2TPP porphyrin structure (left): the fluorinated derivative is obtained through the complete substitution of the H atoms with F atoms on phenyl rings. On the right is presented the structure of the H_2TCPP porphyrin derivative.

5.1.1 - Electronic properties and optical spectra

The Four Orbital Model (FOM) developed by Gouterman in the 1960s [Gouterman1961-1963] is the most widely used theory for interpretation of UV-Vis absorption and emission spectra of porphyrins.
A typical porphyrins absorption spectrum has two main spectral bands:

- an intense and narrow B-Band (or Soret band) in higher energy region of UV-Vis, originated from singlet-singlet $S_0 \rightarrow S_2$ highly dipole allowed transition;
- a wide and structured band at lower energies called Q-band, from singlet-singlet $S_0 \rightarrow S_1$ weakly dipole allowed transition.

Be emphasized that the molecular symmetry influences electronic states. Metal-porphyrins, with a D_{4h} symmetry, has degenerate LUMO states and nearly degenerate HOMO states; x and y polarized excitations generate the two pairs of degenerate low energy Q_x-Q_y and high energy B_x-B_y transitions (**Figure 5.3**).
Free-base porphyrins are different because of the two H atoms, bound to N atoms of pyrrole rings, giving D_{2h} symmetry. This is an idealization of molecule symmetry that is only true if phenyl rings planes are oriented parallel or perpendicular to porphyrin average plane. Available data say that phenyl groups form an angle of nearly 80 degrees [Bell1995, Saini2004] with porphyrin macro-cycle; nevertheless this approximation does not affect electronic states nor in plane molecular vibrations symmetry that can still be considered as belonging to D_{2h} point group. These lower also the energy of the two N atoms involved in binding, thus lowering the energy of c_2 orbital respect to c_1 (see **Figure 5.3**). Gouterman [Gouterman1961] provides also an experimental argument showing how in free-base porphyrins b_2 is higher in energy than b_1: in fact its energy appears not to be influenced by the presence of electron attractor groups on C of methine bridges, as can be seen comparing substituted and non-substituted porphyrins spectra. The decrease of symmetry from D_{4h} to D_{2h} causes further splitting in energy for Q_x and Q_y as well as for B_x and B_y. A simplified scheme of levels is given in **Figure 5.3**.

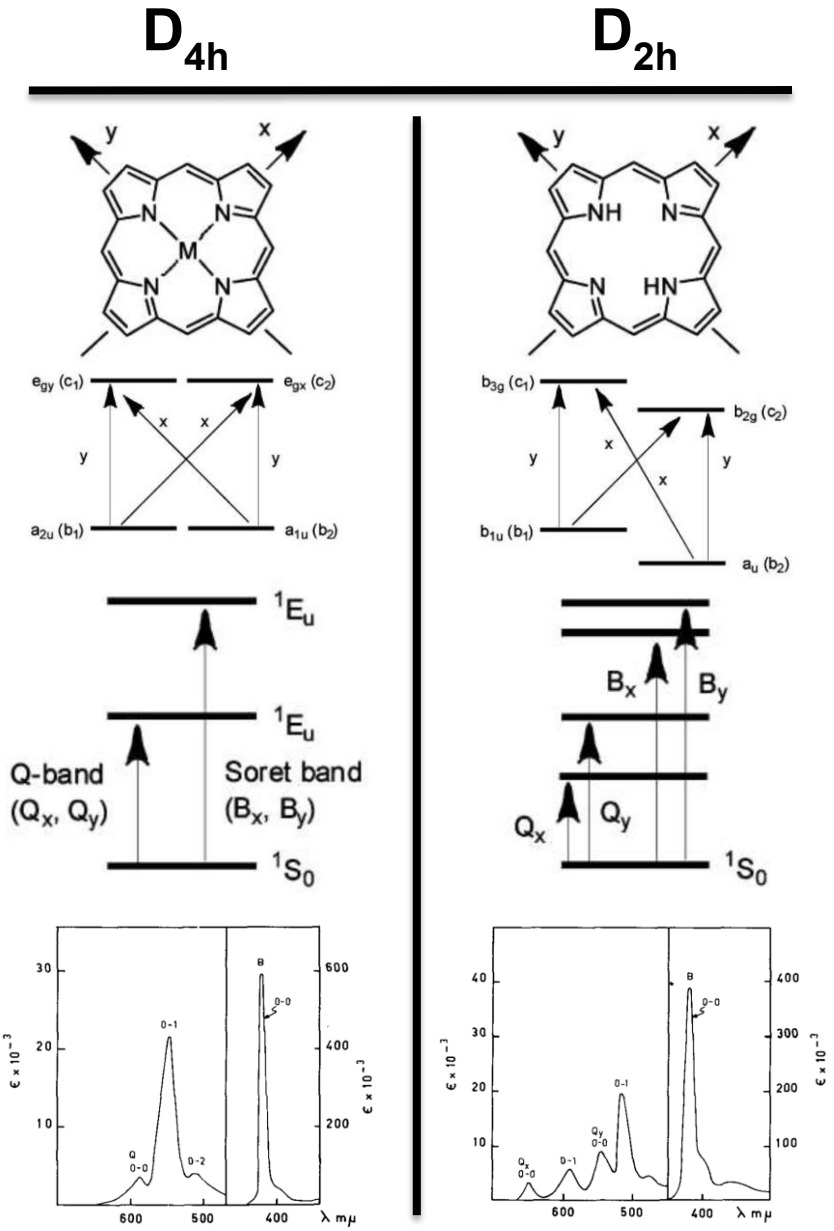

Figure 5.3 Gouterman Four Orbital Model: scheme of levels and absorption spectra for a D_{4h} symmetry metal-porphyrin (left) and a D_{2h} symmetry free-base porphyrin (right), taken from ref. [Gouterman1961-1963, Nemykin2010].

5.2 - Films grown by SuMBD

The depositions have been prepared by the CNR laboratory in Trento with Supersonic molecular Beam Deposition (SuMBD) technique. The detailed description of the experimental setup and the technique itself is located in chapter 2.

5.2.1 - Samples description

Using a Si(111) wafer, as a substrate, is prepared a series of SuMBD samples. For each deposition is used a new substrate cleaned through a multiple washes in trichloroethylene, acetone and isopropyl alcohol for 5 minutes each. Then, the substrates are put in ultra high vacuum and heated up to 200 °C for one night for degasing all contaminants: the residual carbon fraction is evaluated to be less then 0.1 equivalent monolayers (ML).
Depositions of tetra(pentafluoro-phenil)-porphyrin (H_2TPP(F)) on Si substrates are prepared, using the supersonic He beam as carrier gas, for five different deposition times:

- 100 min, sample D1
- 240 min, sample D2
- 470 min, sample D3
- 550 min, sample D4
- Bulk (above 2000 min), sample D5

These deposition times are normalized to an equivalent deposition rate of 0.1 nm/min and the deposition area on the substrate is a circular spot of 1 cm in diameter.
The samples produced by the staff in Trento have been characterized by us employing AFM microscopy as soon as they arrived in Parma.

5.2.2 - The surface behavior: an AFM study

The as grown samples are investigated with Atomic Force Microscopy (AFM) in contact mode, with a gentle set point, to point out the morphology of the surface as function of the deposition time.

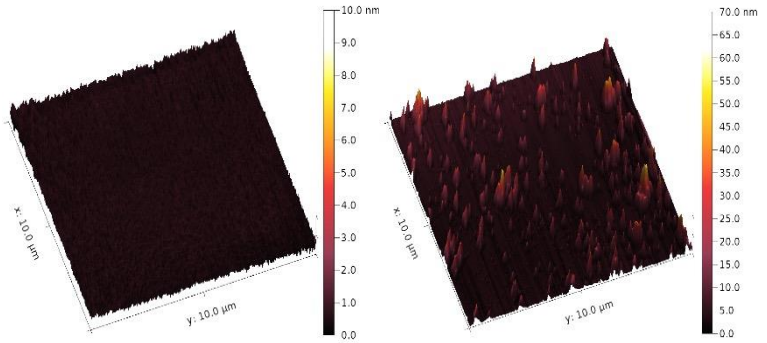

Figure 5.4 AFM topography images of samples D1(left) and D2(right): the contrast is adjusted to 10nm for sample D1 and 70nm for sample D2. In the sample D2 is possible to appreciate the appearance of growth islands not present in sample D1.

The topography images are 10x10 µm in size and the contrast is normalized at 70nm to emphasize the increase in islands high from samples with low coverage to high coverage samples. Only the D1 sample image is normalized at 10 nm to be compared with other sample images.

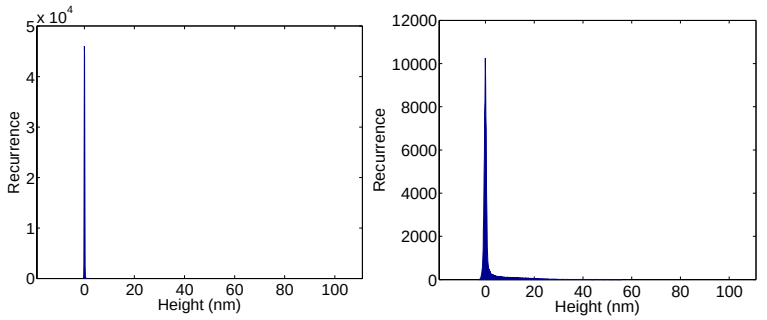

Figure 5.5 The heights distribution of sample D1(left) and D2(right): both distributions are centered at zero. The appearance of a tail in D2 distribution is ascribed to the presence of islands.

The **Figure 5.4** compares samples D1 and D2 in which are present large flat regions together with occasional islands: in particular in the D1 sample the investigated area is free of any islands. Extrapolating the line profiles of each line in each sample figure is possible to have the heights distribution of both samples (**Figure 5.5**). The heights, acquired with the AFM measurement, are to take into account as relative heights because the real zero position is usually centered at the substrate level. Therefore from AFM images it is impossible to speculate if flat regions are covered by porphyrin layers or not. Because of that the peaks shown in **Figure 5.5** are centered both at zero. It's remarkable the appearance of a tail in the distribution of sample D2 that can be correlated to the presence of islands in the AFM image.

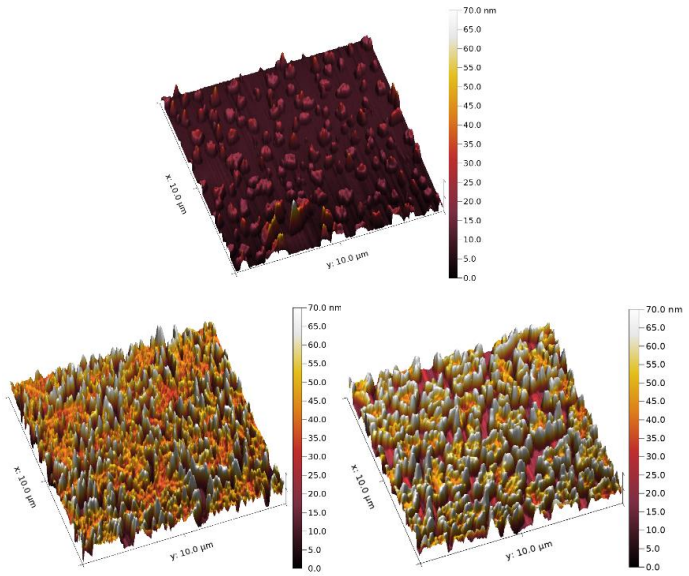

Figure 5.6 AFM topography images of sample D3(top), D4(bottom left), D5(bottom right): a change in the morphology of the growth islands is highlighted.

Focusing on samples with higher coverage (D3, D4 and D5), the AFM images (**Figure 5.6**) show the growth of islands in terms of recurrence, lateral sizes and increase of heights. The related bimodal heights distribution proves the appearance (sample D3)

and the important presence (samples D4, D5) of a second population of heights correlated to the center plateau of islands (**Figure 5.7**). Moreover, AFM topographies show that the tail in the peaks above 30 nm is the signal of edges higher than islands center. The change in the morphology of the islands highlights the possibility to have a discontinuity in the growth mechanism before and after a threshold deposition time. In particular before 500 min the growth mechanism should be completely kinetic, it means that each molecule that hits on the substrate surface, without bounce back, is fixed in the impact position. But, after that threshold, the probability that a molecule migrates on the surface due to its residual thermal energy couldn't be negligible and the edges of nucleated islands play the role of attracting sites because of their greater number of dangling bonds: as a consequence they growth more than the islands center.

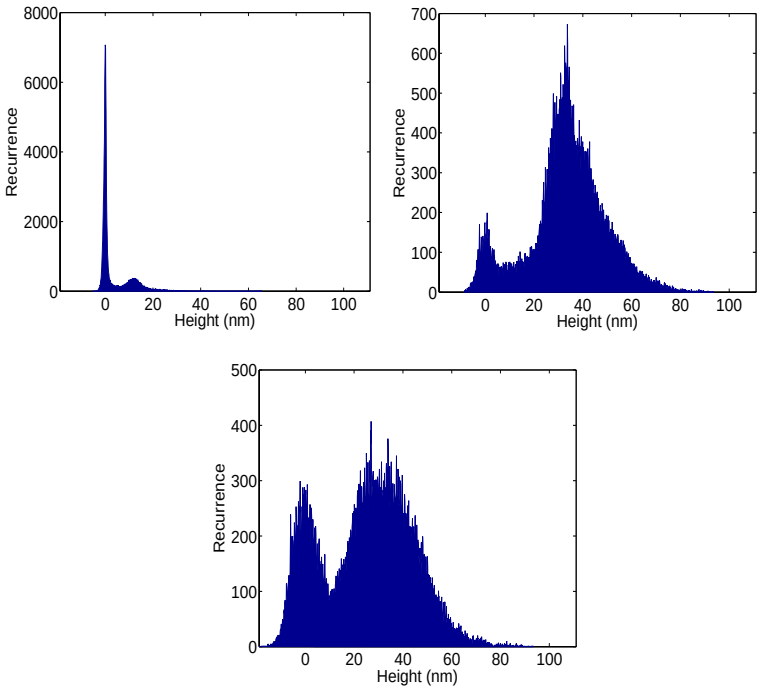

Figure 5.7 The heights distributions of sample D3(top-left), D4(top-right) and D5(bottom): there is the appearance (sample D3) and an important presence (samples D4, D5) of a second heights population associates to the central plateau of islands.

In particular, the possibility that molecules migrate on the surface (after threshold behavior) means that it should be already present a porphyrins layer on the surface because, in this case, the intermolecular interactions are not-covalent (weak) and molecules are allowed to move on the surface just by creating and breaking these bonds. As a result the stacking looks like the usual bulk stacking of porphyrins. Otherwise, if the surface is bare, molecules have to create energetic bindings in order to don't bounce away: therefore a different stacking will be created.

5.2.3 - Microfluorescence revelations

The AFM study doesn't elucidate if something different happens in the first deposition layers: but in this sense, spectroscopic characterizations are useful because the fluorescence spectrum could reflect changes in the electronic distribution due to different interactions between molecules and the substrate or in the stacking orientations. Microfluorescence spectra are acquired both in flat regions and on islands with a 473 nm DPSS laser but unfortunately, for samples D3, D4 and D5, the thickening of islands didn't allow to acquire spectra from the flat regions of the sample.
In **Figure 5.8** are the shown fluorescence spectra acquired in flat regions for samples D1 and D2 together with the typical bulk spectrum of H_2TPP(F). The bulk spectrum is a typical free-base porphyrin fluorescence spectrum accordingly with the Gouterman four orbital model [Gouterman1961-1963]. Focusing on the profiles of the SuMBD spectra, they are thoroughly different because of the presence of only one peak in the 650-670 nm spectral region. Remarkable is to point out its blue shift (about 4 nm) with the decrease of the deposition time: this shift seems to be a decrease in the intensity of the mode at 663 nm rather a real shift of the $Q_x(0,0)$ mode. Low temperature measurements, with improved resolution, might confirm this speculation. As expected, the increase in emission intensity from the shortest deposition time, sample D1, to the sample D2 without a negligible change in shape, is due to the longer deposition time used to grow the sample.

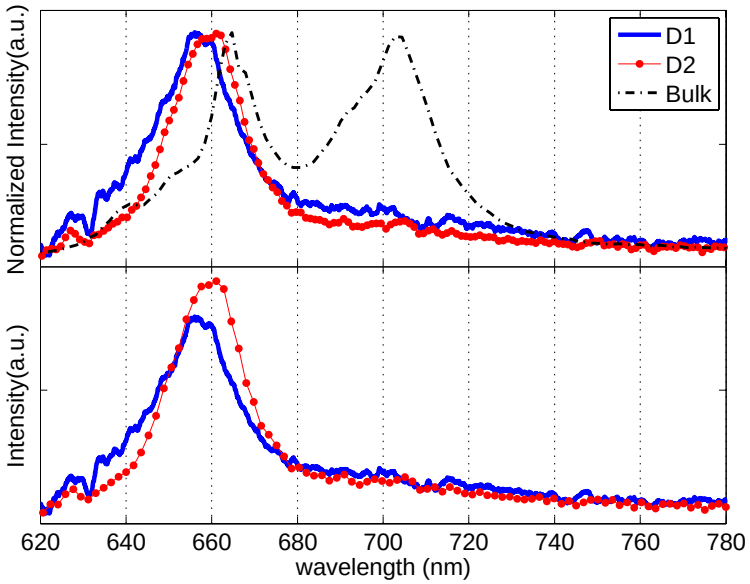

Figure 5.8 Fluorescence spectra of sample D1, D2 and the $H_2TPP(F)$ bulk: the top panel shows the normalized spectra while the bottom panel the difference in intensity of D1 and D2 due to the different deposition times.

Sample D2 is the most interesting sample of the series because of its peculiar morphology: the presence of flat regions together with islands, enough far, allows us to acquire spectra from flat regions and from islands separately, just focusing the laser spot in one of these two areas. The acquired spectra are shown in **Figure 5.9** together with the bulk spectrum of porphyrin. Both spectra of sample D2 are different in shape compared to each other and to the bulk spectrum. In particular, the relative intensity of the mode at 663 nm decreases while the 705 nm mode growth up in islands; at the same time, the shape begins to be bulk like. This spectrum shape is still present in samples D3, D4 and D5 (**Figure 5.10**) in which islands are thickened and the signals coming from flat regions and islands are merged because the size of the laser spot begins to be bigger than the inter-islands distances.

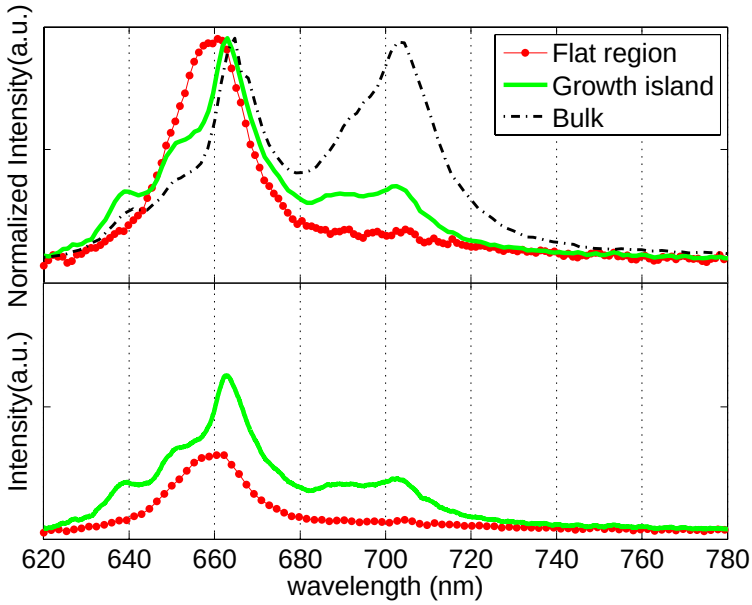

Figure 5.9 Double nature of porphyrin spectra in sample D2. A typical spectrum acquired from a flat region (red dotted line) is plotted together with the typical spectrum of an island (green line) and the spectrum of bulk (black dashed line).

Speculating about the relationship of emission spectra and molecular arrangements, seems reasonable that inside islands, the molecules stack accordingly to their thermodynamic arrangement in which the main intermolecular bond is the interaction between π orbitals of porphyrin macro-cycles [Akins1996], while, the strong difference in shape of the flat regions spectra justify a strong change in the molecular interactions with the substrate as well as in the interactions between molecules.

At the same time, is well known from literature [Iannotta2003] that SuMBD depositions are kinetic depositions in which molecules, to be deposited, acquire up to 25 eV of kinetic energy using He as carrier gas. Therefore, different mechanisms could occur in the first layers of deposition where incoming molecules have enough kinetic energy to be converted in binding energy but only few molecules are present on the substrate.

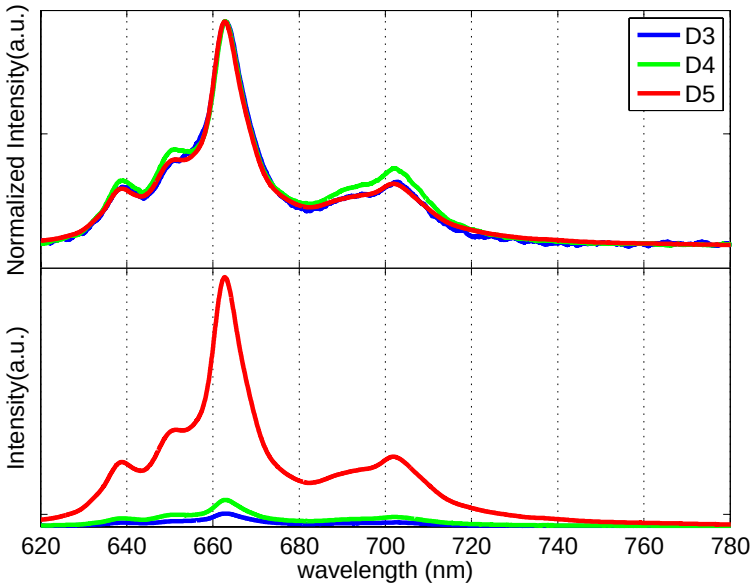

Figure 5.10 Spectra of the high coverage samples. All spectra, D3 (blue line), D4 (green line) and D5 (red line) are consistent to the typical spectrum of islands in sample D2. The progressive increase in intensity is due to the bigger amount of porphyrin molecules on the surface because of the longer deposition times.

5.2.4 - X-ray Photoelectron Spectroscopy (XPS) confirmations

To understand in detail what is happening in the first deposition layers, new SuMBD growths are produced by the group of Dr. Roberto Verucchi at CNR of Trento and a detailed in-situ XPS study is performed. Measurements are performed in a broad energy range (Survey, Pass Energy PE=50eV), in high resolution (PE=20 and 10 eV), using the Mg K_α photons (1253.6 eV). A quantitative analysis of the increase of the F1s signal, originated by the porphyrin molecules, and the consequent decreasing of O1s signal, produced by the native oxide layer present on the Si substrate, has been performed.
In **Figure 5.11** are reported two typical XPS spectra of the F1s (left) and O1s (right) signals acquired from sample D2. Experimental

data are presented together with their global fits and with all the various components that will be described in detail in a few lines.

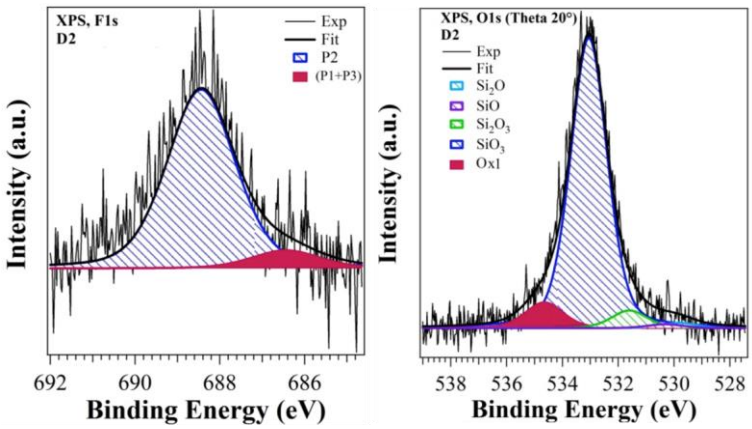

Figure 5.11 Two XPS typical spectra of F1s signal (left) and O1s signal (right) obtained from sample D2. See text for more details.

Two reasons are involved in the choice to focus on these two signals: i) the F1s atoms are present in large amount into the molecules but at the same time totally absent on the substrate surface, ii) the O1s signal hasn't any spectral overlaps with F1s. Moreover, the O1s atoms are involved mainly in interactions with the porphyrin molecules because they are located in a layer of few nanometers onto the substrate surface; as a result the contribution to the XPS signal related to the various kinds of Si-O bonds, present in the not stoichiometric native oxide layer, is minimized.
The analysis by the deconvolution of the XPS spectra of F1s and O1s core levels, performed in the group of Trento, highlights different contributions. Starting from the F1s core level, three signals can be extrapolated from data:
P1) the contribution related to the F-Si bonds established because the native oxide layer has many defects on the surface (Si dangling bonds)
P2) the contribution of the F-C bonds into H_2TPP(F) phenyls
P3) the contribution related to the establishment of F-O-Si bonds.
At the same time, during the molecules deposition, in the O1s signal appears a new contribution, Ox1, directly related to the interaction between the deposited molecules and the oxygen atoms present on the surface.

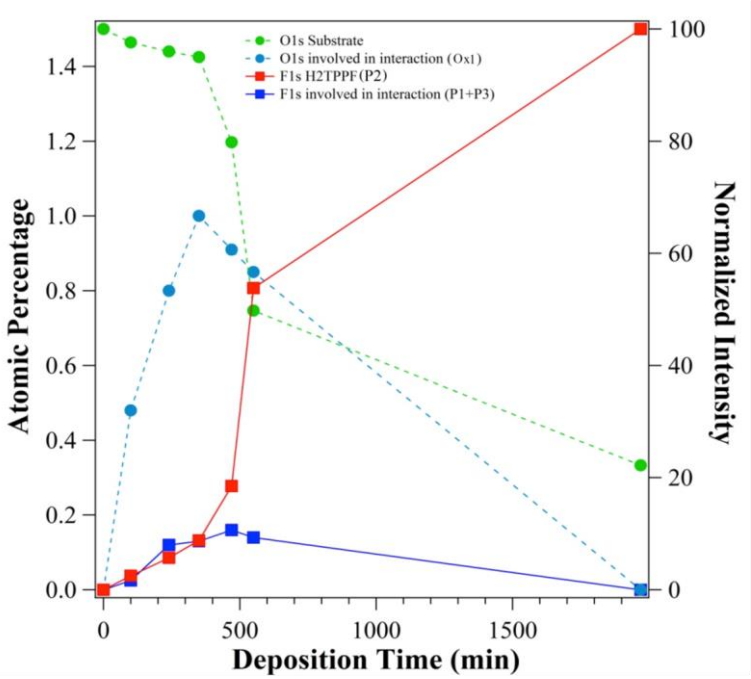

Figure 5.12 XPS signals acquired during the sample depositions. F1s signals: P2 (F-C, red squares), P1 and P3 (F-Si and F-O-Si, blue squares). O1s signals: Ox1 (blue circles) and O1s (global signal, green circles). Trends are extrapolated by the deconvolution of XPS signals as a function of the deposition times.

Significant trends can be extracted from the XPS spectra even if some care must be exercised; as obvious, cross correlations exists between the fitted amplitude of some peaks due to partial overlap, as shown in **Figure 5.11**. For each contribution, the resulting trends are shown in atomic percentage (**Figure 5.12**, left axis) together with the normalized intensity of the overall O1s signal generated by the substrate (**Figure 5.12**, right axis). Focusing on F1s contributions, P2 (red line) increase progressively during the molecules deposition but the global contribution (P1+P3), related to the interactions between molecules and the surface, increases only until 400-500 min and then decreases. The same trend is found for the oxygen contribution Ox1 as the proof that an interaction between the F and the O atoms is established. Our hypothesis is based on the formation of a "wetting layer" at the interface with the substrate in which porphyrins interact through F-O-Si and F-Si

bonds with the oxide surface; this layer coexists with physisorbed molecules during the growth process. The gradual increase of F-C signal is consistent to the increasing amount of porphyrins deposited on the surface but, if the "wetting layer" covers the entire surface uniformly and the physisorbed molecules are only on top, the signals of F1s (P1+P3) will be expected to decrease quickly from the beginning; conversely, these signals start to decrease only after 470 min. Basing on the AFM and fluorescence evidences, these trends (even with the caveats due to cross correlations mentioned above) seem to proof that the "wetting layer" is completed only after 400-500 min. Accordingly, all employed techniques are consistent to infer that the H_2TPP(F) SuMBD growths aren't layer-by-layer growths but a peculiar Starki-Krastanov growths. The growth starts with a layer by layer growth followed by a three dimensional islands growth; usually occurring in few monolayers, in our case, this continues for many deposition layers together with the growth of islands.

5.3 - The 3C-SiC@SiO_x core-shell nanowires

Having validated the formation of the "smart" organic/inorganic interface, the next step is to synthesize, characterize and evaluate the singlet oxygen generation of the proposed hybrid nanosystem. Because the SuMBD technique highlighted problems related to the uniformity of the functionalization, 3C-SiC/SiO_x nanowires are functionalized by chemists of the Parma University using the "click chemistry" procedures in which the tetra(N-propynyl-4-aminocarbonylphenyl)porphyrin (H_2TPACPP) is attached unto NWs surface.

5.3.1 - Interests and structure overview

SiC-based systems are studied in the last two decades because they are promising for many interesting applications: in particular 3C-SiC for biomedical applications [Cicero2004] due to its high biocompatibility [Rewin2009]. The 1D system as nanowires, if functionalized with porphyrins, could be employed as nanoprobe to realize a new class of high-sensitivity biosensors based on molecular recognition. The choice of porphyrins to create a suitable inorganic/organic interface is also supported by the good match between the 3C-SiC near-band-edge optical emission and the porphyrin absorption Q band. In this sense, the possible application for such a system is in cancer treatments. The 3C-SiC green emission can be used by porphyrins to activate the production of singlet oxygen, the dominant cytotoxic agent produced during photodynamic therapy (PDT) [Allison2004, Chen2006]. In order to enhance the near band edge emission of SiC, one interesting strategy is to cover the nanostructure surface with silicon oxide resulting in a core-shell structure. Because the silicon oxide is a wide band-gap material, this geometry could improve the energy transfer from the shell to the core without any modification of the emission energy.

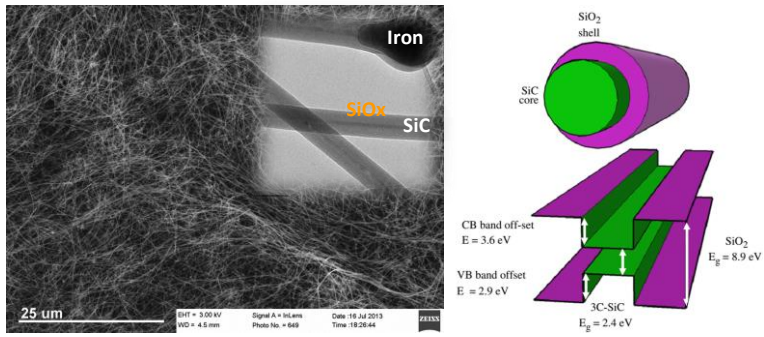

Figure 5.13 SEM image of the NWs ensemble (left), the STEM image of the core-shell structure (left, inset) and a scheme of the related type-I band alignment (right, taken from [Fabbri2010]).

In this direction, our collaborators of IMEM-CNR of Parma synthetized 3C-SiC@SiO_2 core-shell nanowires (**Figure 5.13**) arguing that in the structure there is a type-I band alignment [Fabbri2010]. In this system, following an excitation of the silicon oxide shell, carriers could be injected into the core, and here recombine according to the allowed transitions in 3C-SiC. Moreover, the shell plays the role of SiC surface passivation layer reducing the non-radiative surface recombinations of carriers; in addiction it can be tuned in thickness to induce a possible quantum confinement.

5.4 - Porphyrinated SiC@SiO$_x$ NWs for Self-Lighting PDT

In this section the focus is on the complete characterization of the nanowires structure and the optical properties of the nanosystem. Therefore the singlet oxygen generation experiments are reported and then the effectiveness of the oxidative stress on cells culture are evaluated.

5.4.1 - Hybrid nanosystem: structure and spectroscopic properties

The free porphyrin in dichloromethane solution is studied by UV-Vis absorption and fluorescence emission spectroscopy (**Figure 5.14**).

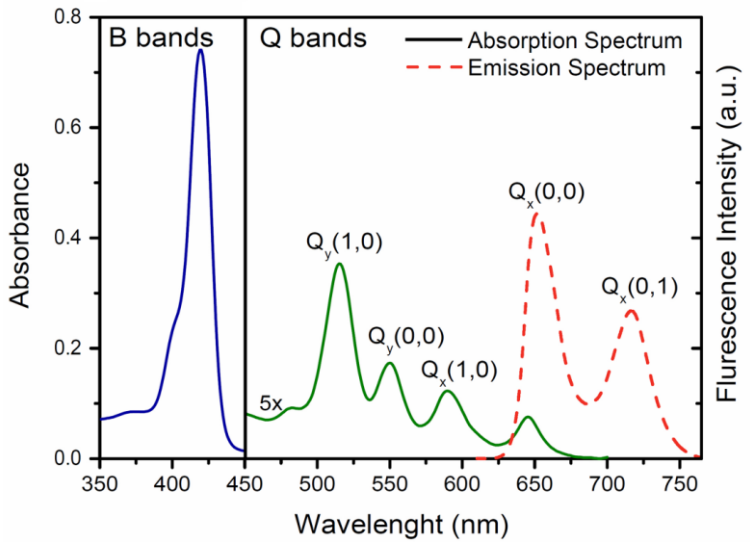

Figure 5.14 Spectroscopic characterization of H_2TPACPP: Absorption (solid lines) and fluorescence (dashed line) spectra acquired in solution.

The absorption spectrum comprehends the Soret-band at 420 nm ($S_0 \rightarrow S_2$, highly dipole allowed transition, blue line) and the Q-band at 516, 550, 590 and 645 nm ($S_0 \rightarrow S_1$, weakly dipole allowed transition, green line amplified by a factor of 5). The superimposed emission spectrum (dashed line) from solution presents a small Stokes shift, estimated as:

$$\Delta E_{Stokes} = E^{Q(0,0)}_{abs} - E^{Q(0,0)}_{em} = 150 \pm 40 \text{ cm}^{-1} \qquad \text{Eq. 1}$$

We identify the $Q_x(0,0)$ and $Q_x(0,1)$ emission peaks at 652 nm and 717 nm, respectively. These findings are consistent with the prediction of the four orbital model of free-base porphyrins [Gouterman1961-1963] determined by the 2-fold symmetry of this substituted molecule.
To be sure that the linker does not influence the spectroscopic properties of the porphyrin, both the emission and absorption spectra of the free base porphyrin with and without the linker are performed in solution; the negative control shown in **Figure 5.15** suggests that no changes are introduced by the linker.

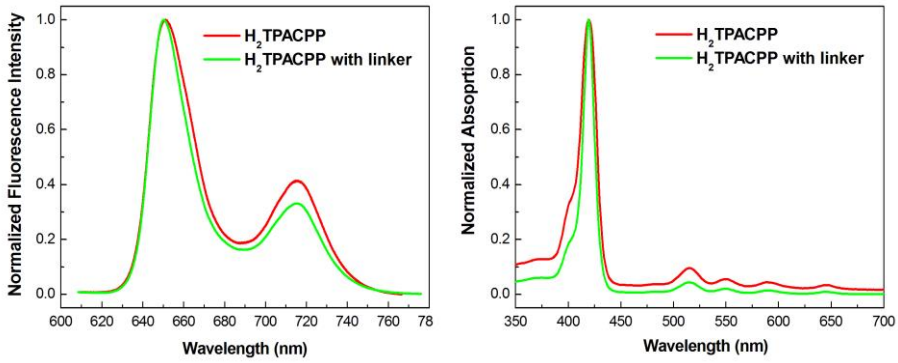

Figure 5.15 Optical characterization of the porphyrin derivative. Fluorescence (left panel) and absorption (right panel) spectra of the starting molecule (H_2TPACPP) and its derivative in dichloromethane solution are shown.

The **Figure 5.16** shows the second component of the hybrid nanosystem: with SEM imaging (**Figure 5.16 left**) is assessed the morphology of the inorganic component by showing that the NWs are arranged in dense tangles. More detailed TEM studies (**Figure**

5.16 right) reveal that the NW structure is made by a crystalline 3C-SiC core (average diameter 20 nm), coated by an amorphous SiO_x shell (average thickness 20 nm), with the catalyst nanoparticle tip.

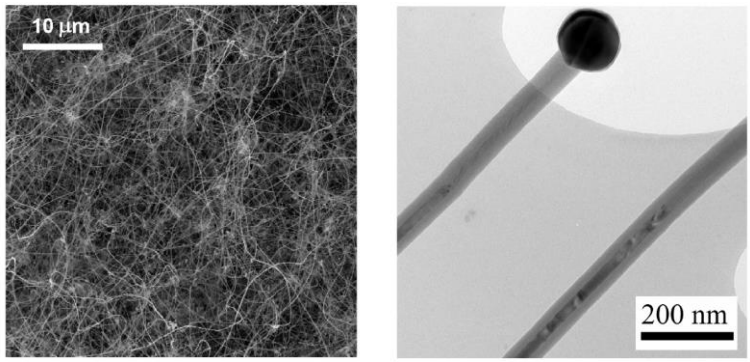

Figure 5.16 Morphological characterizations of core-shell NWs: tangles of NWs highlighted through SEM imaging (left) and core-shell structure shown by TEM image (right).

At a later stage, after the functionalization process between H_2TPACPP and SiC/SiO_x NWs, are studied the changes in the optical emissions among bare NWs, conjugated NWs and porphyrin solution (**Figure 5.17**). The emission from bare NWs consists of a single large and unstructured peak centered at 524 nm, in excellent agreement with the near band-edge emission (NBE) of 3C-SiC [Fabbri2010]. The spectrum of the conjugated NWs clearly contains both contributions originating from the inorganic and organic components. The SiC NBE transition in the NW-H_2TPACPP nanosystem is red-shifted to 545 nm. A similar red-shift has been reported by other authors [Liu-Zhang2008] and, in the present case, can be partly ascribed to the screening effects induced by the absorption of the porphyrin's Q-bands.
Comparing the porphyrin contributions to the emission spectrum of the nanosystem with the fluorescence of the same molecule in solution, one can note a small red shift, in agreement with [Liu2008], and a slight broadening of the peaks. This suggests important steric effects due to the formation of covalent bonds. The adhesion to the locally flat NWs surface (average NW radius ~30 nm, much larger than the molecular size), can lead to a reduction of

the tilting angle of the phenyl rings, with respect to the macro-cycle plane, in analogy with the effect observed in the crystalline phase. This causes an increase in the degree of conjugation of the molecule. Because from literature [Akins1996], both the electronic coupling and the steric molecule arrangement are expected to cause some red shift of the fluorescence, in a similar way, the slight broadening can be ascribed to intermolecular interactions in the solid state between H_2TPACPP molecules besides a possible heterogeneous contribution from environments of different molecular packing.

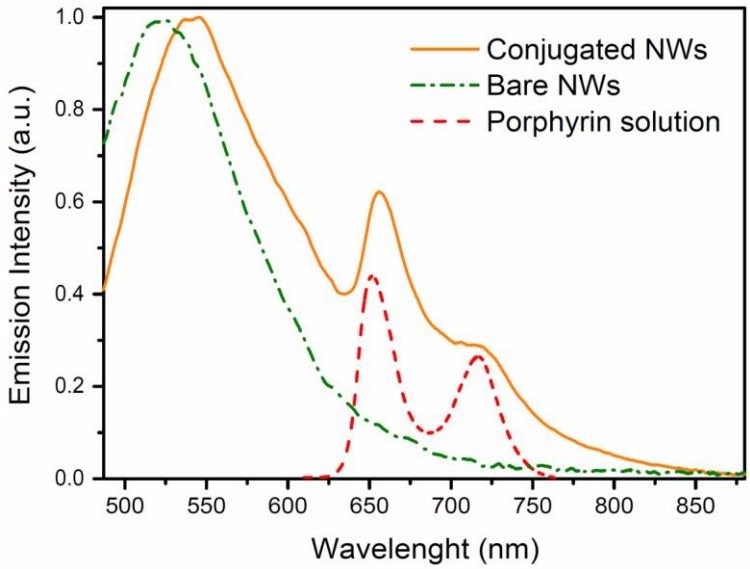

Figure 5.17 Spectroscopic characterization of the NW-H_2TPACPP system: fluorescence spectra acquired at room temperature over as-grown NWs (dashed-dotted line) and NW-H_2TPACPP (solid line). The porphyrin emission (dashed line) is also shown for sake of clarity.

Because the optical excitation is performed at 473 nm, i.e. inside the absorption of NWs but out of the main absorption band of porphyrin, the observed fluorescence, which has indeed a contribution from porphyrin, has to be ascribed to some form of electronic coupling between the NWs and the porphyrin. Can be hypothesized two feasible energy transfer processes:

1. a radiative energy transfer, in which the porphyrin absorbs the light emitted by the NWs, and then it re-emits on her typical $Q_x(0,0)$ emission [Chandrasekhar1960]
2. a Forster resonance energy transfer (FRET), in which the NWs, acting as the donor chromophore, transfer energy to the porphyrin, the acceptor, through non-radiative dipole–dipole coupling [Helms2008, Shankar2009].

We don't stress the discussion on which one process takes place because we believe that one of the two processes should occur due to i) the spectral overlap between the NBE 3C-SiC emission and the porphyrin Q-bands absorption and, ii) because of the proximity between the molecule and the NWs, considering the short chemical linker used.

5.4.2 - Singlet oxygen generation experiment

Having demonstrated the optical properties of the hybrid nanosystem, the next step is the quantification of the efficiency of the hybrid NW-H_2TPACPP system as a source of singlet oxygen ($^1O_2$). The singlet oxygen generation is revealed by a marker kit (Singlet Oxygen Sensor Green, SOSG [SOSG2004]), which shows a green fluorescence enhanced by interaction with $^1O_2$ and is highly selective to $^1O_2$ against other oxygen species (hydroxyl radicals, superoxide etc.). For each run, a set of NWs (2 mg) is dispersed in a given aliquot (500 μL) of the SOSG working solution and the solution is then exposed to radiation (6 MV X-rays in a clinical Linac Varian setup for radiation therapy, **Figure 5.18**).

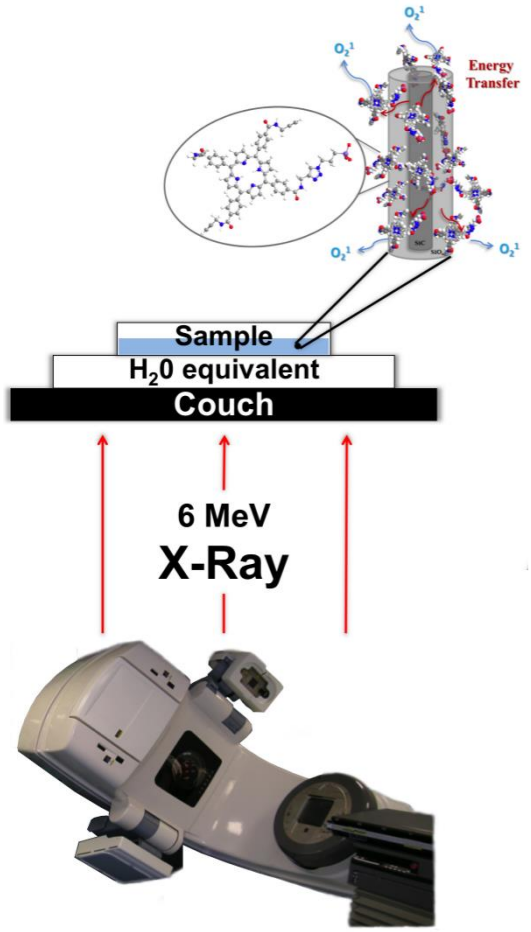

Figure 5.18 Sketch of the X-rays irradiation setup: a dish containing the sample solution is put on the couch and irradiated from the bottom (the picture of the Varian DHX linear accelerator has been taken at the treatment room of the radiotherapy department of Parma Hospital).

After irradiation, the NWs are separated through ultra-centrifugation and 200μL of the remaining solution are sampled for fluorescence analysis. Fluorescence spectra are acquired on the as-prepared solution, the irradiated solution, and the irradiated solution treated with NWs. The spectrum of the not irradiated aliquot is acquired as a reference signal of the SOSG marker, while the spectrum of the irradiated aliquot as a background for the signal of the irradiated aliquot with NWs. Representative

fluorescence spectra of the SOSG marker as-received, irradiated in water without nanowires, and irradiated in water solution containing H_2TPACPP-functionalized NWs are reported in **Figure 5.19**.

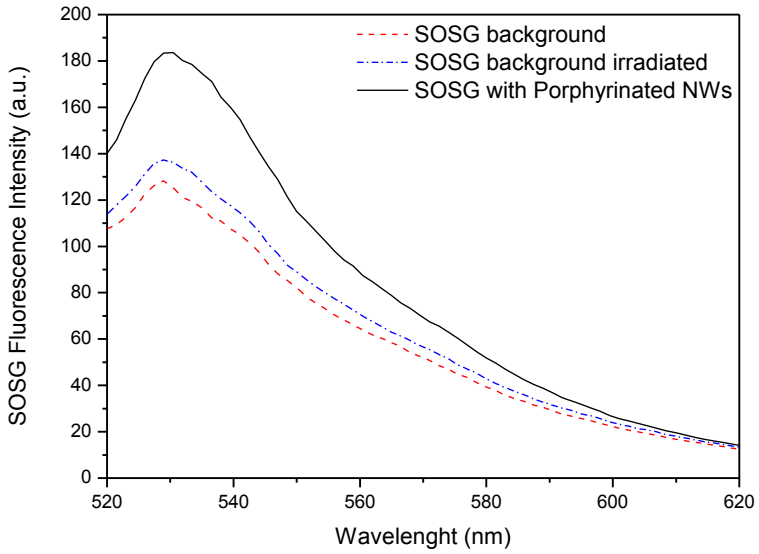

Figure 5.19 Fluorescence spectra from the SOSG kit. The fluorescence is enhanced after treatment with porphyrinated NWs exposed to radiation (spectra acquired at a dose of 0.4 Gy).

The enhancement of the green fluorescence in the SOSG after treatment with the conjugated nanowires exposed to radiation demonstrates its effective activation. This production of $^1O_2$ by the NW-H_2TPACPP system occurs even for extremely low-dose irradiation conditions (0.4 Gy). On the contrary, no SOSG activation is observed in treatments with bare NWs, nor with mere porphyrin solution, confirming that the $^1O_2$ production requires the conjugated NW-porphyrin system and takes place through the self-lighting photodynamic process.

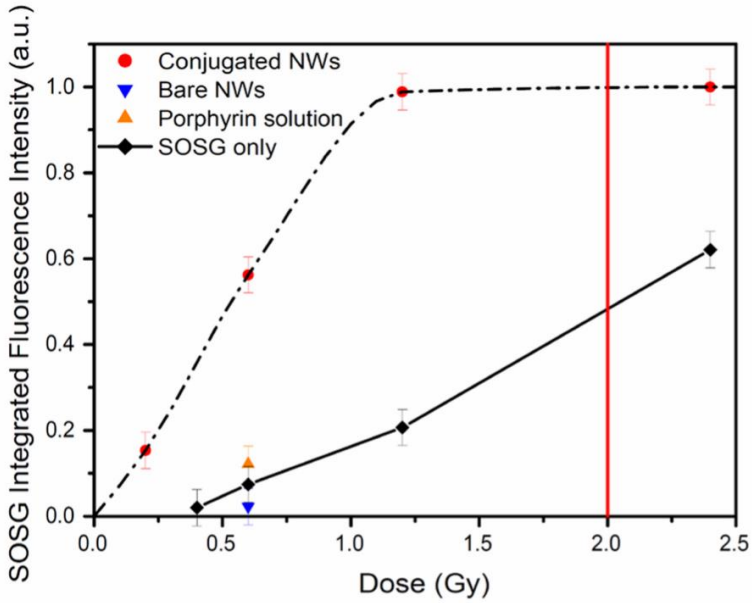

Figure 5.20 Integrated fluorescence intensity, proportional to $^1O_2$ generated, as a function of the radiation dose. The experimental points are obtained from SOSG kit in water, with H_2TPACPP-functionalized NWs (red circles) or without NWs (black diamonds). The orange up-triangle at 0.6 Gy is the experimental point obtained from SOSG kit in a water solution of mere porphyrin, while the blue down-triangle is obtained from SOSG kit in a water suspension of NWs as grown. The usual dose for clinical treatment (2 Gy) is indicated by the red vertical line and the black dashed line is a guide to the eye.

The $^1O_2$ concentration, as deduced from the integrated intensity of SOSG fluorescence, increases steeply as a function of the dose released up to 1 Gy. The dose-response relationship is shown in **Figure 5.20**, from extremely low dose values (fraction of Gy) to typical doses of radiation therapy in clinical cancer treatments (~2 Gy per each session). The response of the nanosystem suspension (NW-H_2TPACPP in water, red circles) is well above the control solution (SOSG kit alone in water, black diamonds) and almost 5 times higher than the mere porphyrin response at the same dose (free porphyrin diluted in water, orange up-triangle) as well as the NWs as grown (suspension in water, blue down-triangle).
The saturation in the SOSG fluorescence signal reached around 1Gy can be reasonably attributed to the finite capacity of SOSG

molecules to detect $^1O_2$ immediately after it has been produced. This is limited on one side by the short lifetime of this species in water (4 μs [Egorov1989]) and on the other side by the exchange - limited by diffusion- of SOSG molecules between the nanosystem surface and the bulk of the solution. One possible strategy to promote the interaction between the SOSG molecules and the singlet oxygen molecules, before their disexcitation to ground state, is to increase the SOSG concentration. Relying on the SOSG data sheet, the window of linear response of this marker is one order of magnitude in concentration, ranging from 1 to 10 μM. Unfortunately, fixing all the other parameters, in this range we checked no appreciable changes in the fluorescence response.
Another possible explanation, which cannot be ruled out, but is deemed less probable, is that for some intrinsic reasons the production of $^1O_2$ itself is limited. This could be the case only if the supply of O_2 molecules would be limited or if the conversion to singlet state is irreversible, which seems to be unrealistic assumptions.

5.4.3 - Oxidative stress evaluation on cells

Having demonstrated the efficiency of $^1O_2$ production, the next step consists in employing it to kill cancer cells. For this purpose, in vitro experiments are performed on A549 adenocarcinomic human alveolar basal epithelial cells, to test the efficiency of the NW-H_2TPACPP nanosystem for possible self-lighting photodynamic therapy. We have been chosen this line of cells because the goal is to highlight the oxidative stress above collateral effects (i.e. the mere X-rays exposure, the variation of environmental temperature, the CO_2 content, etc.); these cells are enough strong to not be much affected by other factors.

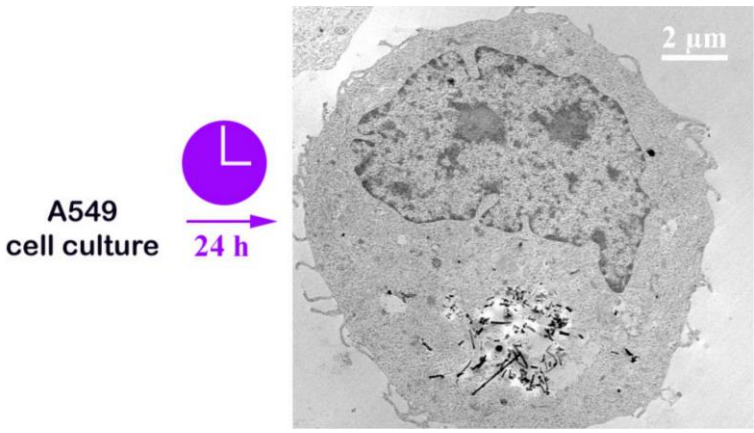

Figure 5.21 Incubated cells, the uptake and the internalization of the NWs during the first 24h.

Previous studies of our colleagues [Cacchioli2014] demonstrated that A549 cells, incubated with the NWs, are able to actively internalize them, mainly for macropinocytosis, and that after 24h an almost complete NW uptake and compartmentalization is observed (**Figure 5.21**). For the present study, A549 cells are incubated with H_2TPACPP-conjugated NWs and irradiated after 24h with 6 MV X-rays at the dose of 2 Gy, chosen accordingly to the standard conditions of clinical radiation therapy (single session). After treatment, a clonogenic survival assay (**Figure 5.22**) has been performed. Briefly, an appropriate number of cells are seeded in triplicate in 6-well plates and cultured for 12 days. After this period, the colonies are fixed with methanol:acetic acid (3:1, v/v), stained with crystal violet and scored as survivors when constituted by more than 50 cells. Unirradiated cultures are processed in the same experiment. The surviving fractions are calculated relative to the mean plating efficiency of cells untreated with NWs and unirradiated. The histograms (**Figure 5.22**) indicate that H_2TPACPP-conjugated NWs affect the survival of A549 cells, either under or without irradiation.

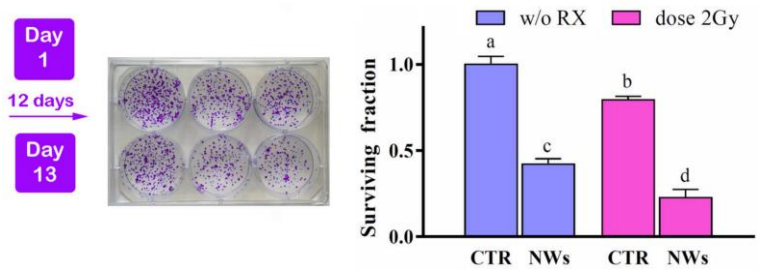

Figure 5.22 Clonogenic survival assay: colonies stained after 12 days (left). The histograms (right), normalized to the control cells, report the surviving fraction of cells treated only with the NW-H_2TPACPP (50 μg/ml), only with radiation (2 Gy) or in combination of NW-H_2TPACPP and radiation.

These results have been obtained with an irradiation time of 20 sec, which is significantly shorter than the standard clinical treatment times (40 sec with single, 90 sec with multiple irradiation fields). This shortening of the irradiation time is extremely relevant for minimizing target missing due to patient movements and reducing the psychological and physical discomfort due to the immobilization inside the isolated treatment room.
Nevertheless, the effect directly related to the Self-Lighting PDT is partially shaded by two effects: i) the effect due to the exposure to X-rays of cells without conjugated-NWs (**Figure 5.22**, difference between columns a and b) and ii) the effect due to the presence of conjugated-NWs inside the cells culture without X-rays exposure (**Figure 5.22**, difference between columns a and c). The detailed discussion on this point is in the next section but reasons are to be ascribed to the intrinsic local nature of the singlet oxygen production besides the shape of the porphyrinated NWs.

5.5 - From nanostructures to studies of interfaces

How can we reconcile the successful production of singlet oxygen in solution, with the limited results obtained with the first in vitro tests?
An explanation is possible considering the intrinsically local nature of the singlet oxygen production. Firstly, the energy transfer that is responsible for the excitation of oxygen molecules can occurs only if they can go near the porphyrinated NWs in the range of few nanometers, farther the typical lifetime of singlet oxygen in water is about 3-4 μs [Kuminova2009]. As a consequence, considering the diffusion of singlet oxygen molecules as Brownian diffusion in water, the excited oxygen molecules could diffuse roughly 200 nm before their disexcitation to the ground state.
Now, as a result of the their shape and size, porphyrinated NWs don't have the capability to move and diffuse inside the tissues in which they are injected; if this is an advantage in terms of localization of the treatment at the same time could be a drawback if inside cells the NWs aren't arranged in order to maximize the exposed surface and/or they aren't in the best positions (i.e. hold on the cells membrane, inside the nuclei etc.). This hypothesis is supported by the TEM images of the cells uptake: porphyrinated NWs uptake follows the endocytosis process in which a helpful substance gets into a cell without pass through the cell membrane. In particular, the images reveal a receptor-mediated mechanism based on the formation of an intracellular vesicle following the invagination and the subsequent fusion of the plasmatic membrane. Furthermore, images point out that the NWs are internalized in bundles inside vesicles [Cacchioli2014]. This situation "protects" vital parts of the cells (e.g. membranes, mitochondria…) from the destroying action of the singlet oxygen produced on the nanostructure surface. Therefore this situation might hamper the effectiveness of the treatment.
To overcome this limit, a possible way is to jump on the other side of the problem growing nanoparticles that can have high capability

to diffuse. The goal should be an internalization process in which every nanoparticle enters in cells individually, without sticking to each other, but that are able to anchor themselves on i.e. cellular organelles. Another strategy could be nanoparticles that stay stick on the cells membrane without to be internalized. In both cases, the release of singlet oxygen dose would be exactly where cells are more weak. The main problem of these hypothetical nanoparticles is their confinement in the region to treat. Therefore it's necessary the functionalization with a targeting molecules built for sticking on a target among which the cell membranes or cell nuclei or other organelles. A new step of functionalization is for sure a complication in the synthesis process but the resulted advantages justify the study of biocompatible nanoparticles that can be coupled with targeting molecules.
This motivated a preliminary study on core-shell nanoparticles based on CeF_3@ZnO. Some results have been obtained during my visit at University of Texas at Arlington in the group of Prof. Wey Chen, one of the pioneers of the study related to SL-PDT mechanism. The study is described in detail in the next section but the goal is the synthesis of biocompatible scintillators easy to functionalize with photosensitizers. Is well known that CeF_3 nanoparticles are effective in energy conversion from X-rays to visible light but contemporary they possess low biocompatibility without a capping agent (usually polymers) besides a low surface reactivity in terms of possible functionalization reactions available at the state of the art. Here is the requirement of ZnO shell; as for many oxides, they open the door to a lot of "easy ways" to functionalize themselves with organic molecules. In addiction many oxides, as ZnO, are proved biocompatible and provide new interesting properties.
However, there is an open question concerning how these nanoparticles interact locally with themselves and with the cell membrane during the internalization process. This is a significant point if the goal is a high efficiency in the oxidative stress induced by singlet oxygen generation. To investigate their collective behavior and the physics of their interactions at the nanoscopic scale, two studies on nanoparticle's bidimensional networks are performed. We have chosen to start from two model nanosystems, chosen for their simplicity 1) hydrophobic gold nanoparticles at the

air/water interface and 2) silica nanoparticles allowed to interact with phospholipid layers, chosen as the paradigm of an ideal interaction between a hydrophilic nanoparticle and the basic constituent unit of cell membranes. Nevertheless, investigations on both these systems are focused on the basic physical mechanisms behind them, we believe that in the future this in-depth analysis of the interactions could be useful to foresee which nanostructures will be the best to use.

5.6 - CeF_3@ZnO core-shell nanoparticles for Self-Lighting PDT

One possible way to overcome the open problem related to the spreading in the best positions of scintillating nanostructures for a high efficiency SL-PDT treatments is to synthetize stabilized nanoparticles that can be able to diffuse uniformly inside cells (in-vitro tests) or tissues (in-vivo treatments). Achieved this goal, a specific functionalization with targeting agents will allow the control of the spreading only in the diseased tissues instead of healthy tissues.
Following this current, the idea is to obtain biocompatible scintillating nanoparticles easy to functionalize. For these reasons, during my visit at University of Texas at Arlington in the group of Prof. Wey Chen, one of the pioneers in the study of SL-PDT mechanism, I worked on the synthesis of core-shell nanoparticles based on CeF_3@ZnO.
The choice of these two materials is related, from the first side, to the effectiveness of CeF_3 as energy converter from X-rays to visible light and on the other side to the good surface reactivity of ZnO that open the door to a lot of "easy" functionalization processes with different photosensitizers, including porphyrins. Moreover is proved that CeF_3 and ZnO nanoparticles blends show energy transfer by FRET after irradiation with 90 keV X-rays [Sahi2013]. Starting from this result, the production of a core-shell structure, provides a more intimate interaction between the two nanomaterials; this could increase the efficiency of the energy transfer mechanism.

5.6.1 - Preliminary results: synthesis and optical characterizations

The synthesis of CeF_3 seeds is performed following the procedure described in [Sahi2013]. In a 3 necks round flask is dissolved $Ce(NO_3)_2$ in water together with the surfactant (i.e. $PEG(COOH)_2$

or PEG-400), then a stoichiometric amount of NH_4F is added drop wise to the solution maintained under magnetic stirring. The reaction is kept at reflux for 2 hours and, after several washes with distilled water, a white precipitate is collected at the bottom of the test tube through ultra-centrifugation at 13 krpm. The CeF_3 solution, obtained after a final dispersion in distilled water, is shown in **Figure 5.23 left**; the solution is white-like without any trace of precipitate or turbidity, signal of the high stability of the nanoparticles suspension.

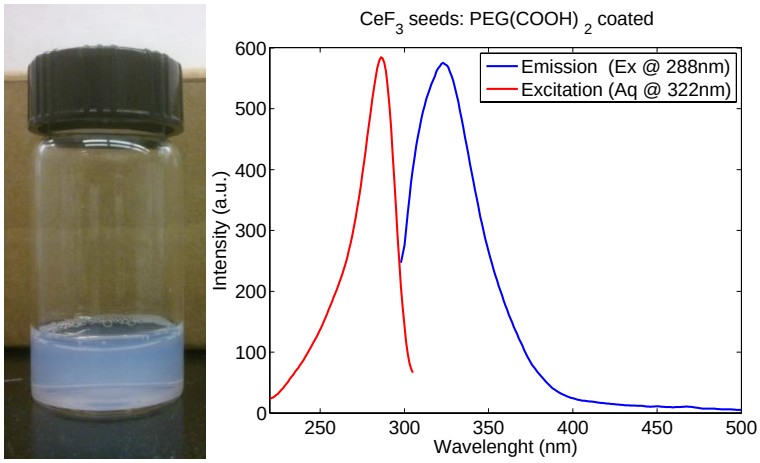

Figure 5.23 The as synthetized CeF_3 seeds. A suspension of nanoparticles is reported (left) together with the luminescence spectra (right).

Luminescence and excitation measurements are performed immediately after synthesis and the results are reported in **Figure 5.23 right**: the emission peak is slightly broad and is centered on 325 nm. Because the spectral position of the emission is related to the particles size -smaller particles have higher blue shift of the optical emission and vice versa- the size of the as synthetized nanoparticles is smaller than 10 nm, in agreement with [Sahi2013].

Before the synthesis of the core-shell nanoparticles, an optimization of the synthesis of ZnO has been performed. In particular, an accurate control of the temperature, the duration and the pH of the reaction are probed. The reaction is performed in a 3 necks round flask kept at 48° C where $Zn(ac)_2$ is dissolved in distilled water. Now, di-ethylene glycol (DEG) is first added under magnetic

stirring and after triethanolamine (molar ratio with Zn ions equals to 2) is added drop wise to the solution. The reaction is left to run for 15 minutes and then the obtained ZnO nanocrystals are immediately washed several times and re-dispersed in distilled water.

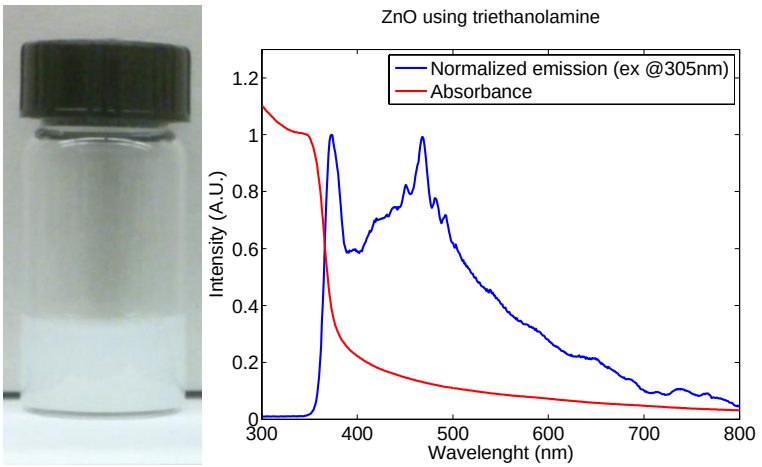

Figure 5.24 The as synthetized ZnO nanocrystals. The suspension in water (left) together with absorption and emission spectra (right).

The resulted suspension is shown in **Figure 5.24 left** while on the **right** are shown the absorption and the emission spectra of the as grown ZnO nanocrystals, in agreement with [Sahi2013, Woo2008]. It is possible to observe the characteristic NBE peak centered on 373 nm and a broad structured band that is related both to the surface defects and the surfactant (DEG) anchored onto the nanocrystals surface. At the same time the absorption spectrum highlights a sharp absorption edge at 350 nm without a significant background; this is a good indication that the nanocrystals are small and well dispersed. In support of that, in literature similar emission peaks, around 373 nm, are related to nanoparticles size of the order of 10 nm [Woo2008].
Now, the synthesis of core-shell nanoparticles is performed adding the CeF_3 seeds at the beginning of the ZnO reaction and following the same procedure described above. Because one of the key parameters is the ratio between the seeds amount and the final ZnO amount, four different CeF_3:ZnO mass ratios are tried. A

subtle control of this ratio allows to adjust the shell thickness besides to avoid homogeneous nucleation that causes the synthesis of unintended nanostructures as CeF_3-ZnO dumbbell or ZnO isolated nanoparticles. Accordingly, the seeds amount are fixed to 10mg in each reaction and the mass ratios are calculated considering the amount of $Zn(ac)_2$ precursor to obtain 10 mg (ratio 1:1), 5 mg (ratio 1:0.5), 2 mg (ratio 1:0.2) or 1mg (ratio 1:0.1) of ZnO at the end of the synthesis. The only assumption is that the entire precursor amount is converted to product during the reaction. Because in general the efficiency of chemical reactions is lower than one, the real mass ratio at the end will be lower than the theoretical: luckily, low concentrations of shell precursor promote the heterogeneous nucleation instead of homogeneous therefore this assumption doesn't cut down the success of the reaction.

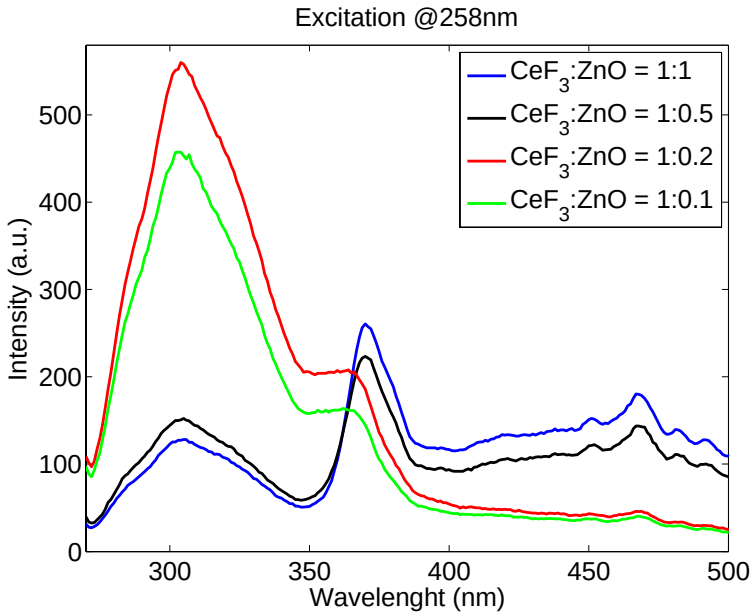

Figure 5.25 Emission spectra of CeF_3@ZnO nanostructures acquired for different mass ratios of the two compounds.

In **Figure 5.25** are shown the emission spectra acquired from solutions of the four samples synthetized. After samples cleaning, each solution is obtained dispersing 1mg of dried powder in 1mL of deionized water. The spectra are acquired with an excitation

wavelength of 258 nm that correspond to the maximum of the excitation peak of the CeF_3 seeds. Both signals of the CeF_3 seeds and ZnO are present at 310 nm and 375 nm respectively, showing that the ZnO reaction is correctly occurred but at the same time two different spectrum shapes come out. The relative intensities between CeF_3 signal and ZnO signal are reversed from low ratios to high ratios synthesis. This is explainable considering the different amount of triethanolamine used in these four reactions: the molar ratio between Zn ions and triethanolamine is kept constant to two, as a result the total quantity of the latter is different for each synthesis and in particular higher for 1:1 and 1:0.5 ratios respect to 1:0.2 and 1:0.1 ratios. Accordingly, the emission spectra highlight a strong increase in the intensity of the emission peak of CeF_3 starting from 1:1 and 1:0.5 to 1:0.2 and 1:0.1 ratios where less amount of triethanolamine is used.
There results show that triethanolamine may limit the oxidation of seeds but doesn't delete it. Moreover, it will be necessary to analyze the CeF_3@ZnO nanostructure with the TEM and/or SEM in order to establish if the synthesis have been produced the correct core-shell shape in addiction to verify their polidispersity. Nevertheless, in this preliminary study, emission spectra point out promising evidences that the reaction procedure is directed in the right way to realize a fluoride-oxide core-shell nanostructure.

6 *Nanosystems at interfaces*

In this chapter are reported two studies on nanoparticle's bidimensional networks aimed to understand their collective behavior and the physics of interactions at the nanoscopic scale. First a 2D network of gold nanoparticles has been investigated and later, was examined a mixed monolayer of DPPC/silica nanoparticles. We decided to start from hydrophobic gold nanoparticles at the air/water interface to study the interactions and the dynamics involved between nanostructures, in water environment.

6.1 - Gold nanoparticles (GNP) network at air/water interface

Nanoparticles are synthesized by our colleagues A. Pucci and G. Ruggeri of Department of Chemistry at Pisa University following the two-phase Brust method [Brust1994, Pucci2004]. In brief, 0.400 g (1.02 mmol) of hydrogen tetrachloro-aurate (III) trihydrate are dissolved in 30 ml of deionized water. The solution is then shaken in a separatory funnel with 80 ml of toluene solution containing 2.00 g (3.56 mmol) of tetra-n-octylammonium bromide (TOAB). The toluene phase is then recovered and combined with 0.018 mL (0.015 g, 0.07 mmol) of dodecyl mercaptan. A freshly prepared aqueous solution of sodium borohydride (25 ml, 0.386 g) is slowly added under vigorous stirring. After further stirring for 3 h, the organic phase is separated, concentrated to 10 ml, and mixed with 70 ml of ethanol. The mixture is cooled overnight at −20°C and the dark precipitate then recovered by filtration.

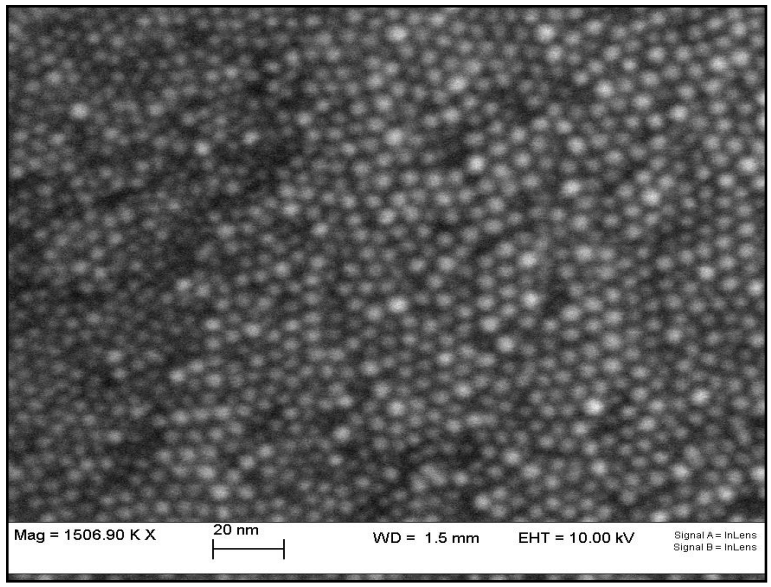

Figure 6.1 SEM image of the gold nanoparticles ensemble.

The crude product is then purified by soxhlet extraction with acetone as cleaning solvent to remove all the unbound free thiol and residual TOAB impurities, thus making the gold NPs (GNPs) fully soluble in organic solvents. The average diameter of the GNPs is estimated to be 8 nm by dynamic light scattering (DLS) analysis with a 6 nm diameter gold nucleus (SEM analysis, **Figure 6.1**).

6.1.1 - GNP Langmuir monolayer production

The Langmuir monolayer is prepared as follows: nanoparticles are dispersed in chloroform, 50 mg in 10 ml, thus obtaining a 5 mg/ml suspension used for long-term storage in the refrigerator. Before each experiment, a small batch of less concentrated suspension is prepared by dilution of the stock solution in hexane, to reach the final concentration of 0.2 mg/ml. This suspension is slowly spread at the air/water interface using a 100 µl Hamilton syringe; the tip of the syringe's needle is kept in contact with the water surface during the whole process. A total volume of 2.5 ml is spread on the Langmuir trough: a spreading time of 2 min is used for the spreading of each syringe. A 20 min waiting time is scheduled to allow solvent evaporation and to achieve the equilibration of the sample. During the experiments the water subphase is kept at constant temperature (18°C), by means of water circulation from a Lauda thermal bath through the Langmuir trough's basement.

6.1.2 - The GNP network structure

The morphology of the formation of a gold nanoparticles 2D network has been investigated in detail by microscopy techniques, revealing a complex structure with features on a hierarchy of different sizes following a Lévy distribution [Orsi2012]. In the incubation time, while the film is left at rest, individual nanoparticles (NPs) diffuse on the surface and aggregate, presumably driven by hydrophobic interaction between the

dodecanethiol coatings. This results in the formation of small disk-like aggregates. Phenomenologically, during the compression, we can identify three steps leading to the gel formation: a first step occurs when disks of sufficient size aggregate because of their mutual attraction, which is due to the indentation effects that those disks exert between each other. In this regime, as soon as an elongated aggregate is formed, e.g., by sticking together of two disks, the aggregation is likely to proceed tip to tip in a fashion similar to that reported in [Schmidle2013], resulting in the formation of quasi-1D structures, which can reach a typical length of few microns. Once those acicular aggregates are formed, a second step occurs with monolayer compression, resulting in the growth of a branched structure, finally yielding to the onset of the infinite percolative cluster, which is related to the building of the mechanical elastic modulus. The third step of formation of the network is the final compaction of this structure.

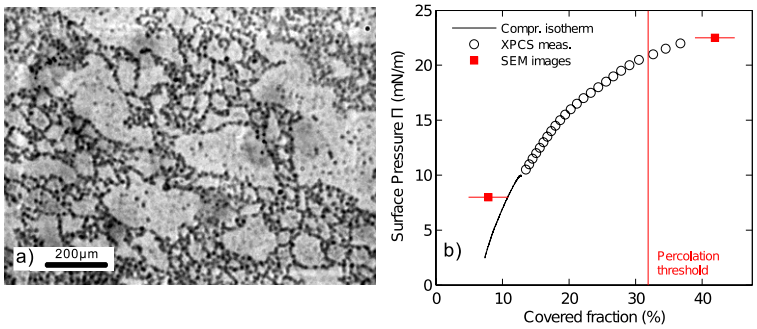

Figure 6.2 At each surface pressure Π, is shown the concentration of gold nanoparticles at the surface, monitored by imaging. (a) Image of the GNP network at Φ = 29%, taken using an inverted microscope with a 50X objective. (b) Surface pressure-concentration isotherm measured during the GI-XPCS experiment. GI-XPCS measurements are performed at the concentrations indicated by the empty circles. As a double check, Φ is also directly measured by SEM imaging on two samples transferred onto solid silicon substrate (red squares).

With the aim to describe in detail the relationship among structure, rheological properties and the dynamic of the 2D network of gold nanoparticles during the formation, we performed experiments covering a wide range of surface concentrations Φ. A sample of the resulting network, imaged by an inverted microscope, acquired with a 50X objective, is shown in **Figure 6.2a**. At the same time,

Figure 6.2b shows the surface pressure-concentration Π-Φ isotherm recorded during the GI-XPCS experiment. Because the importance in the determination of the surface concentration Φ, in our laboratory it has been cross checked employing different techniques: besides calculating Φ from the spread amount, as usual in Langmuir experiments, we also performed in situ epi-microscopy and Brewster angle microscopy on the film floating at the air/water interface, in addition to SEM imaging of films transferred onto the silicon substrate (used for two GI-XPCS selected samples, **Figure 6.2b**). The estimates of Φ arising from these investigation are all consistent with that calculated from the spread amount of nanoparticles.

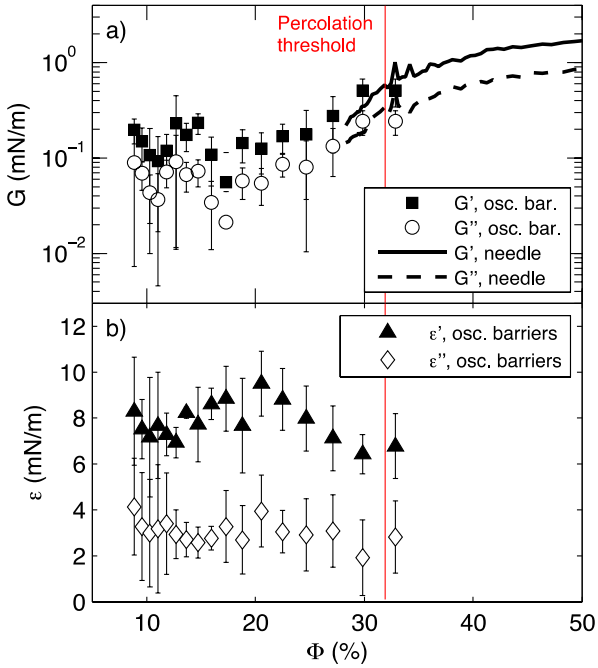

Figure 6.3 The Φ dependence of the mechanical properties of the GNP network during its formation process. (a) The network shows mainly an elastic shear modulus, which increases with Φ. (b) The compressibility stays constant up to the percolation threshold (vertical line).

The evolution of the mechanical response, above and below the percolation transition, has been measured using the techniques

discussed in the previous chapters; results are reported in **Figure 6.3**. In the range relevant to our study, both shear (G) and compression (ε) moduli are mainly real, indicating an elastic response, in agreement with previous results on the same system [Orsi2012]. Moreover it is reasonable to postulate that, at very dilute concentrations, a viscous (dissipative) regime should exist, which may correspond to extremely low values of the moduli, well below the sensitivity limits of the experimental techniques.
Nevertheless, there is an important difference between the shear and compression responses. As shown in **Figure 6.3a**, G presents a transition between two different regimes: for $\Phi < 25\%$ it has a very small value (below 0.2 mN/m, close to the sensitivity limit of the technique), while as the percolation threshold is approached, G starts to increase, reaching a saturation value of the order of 1-2 mN/m, above which it enters a nonlinear regime, indicative of the intrinsic brittleness of this structure. On the contrary, as shown in **Figure 6.3b**, the compression modulus ε stays constant at all the concentrations below the threshold and nonlinear effects dominate above this concentration.
The elastic nature of the mechanical response found below Φ_c has to be ascribed to some kind of long-range repulsion that dominates the dynamics in this diluted regime. Its origin could be electrostatic or could be due to the organic dodecanethiol molecules coating the NPs and providing the thermodynamic stabilization of them in solution through steric repulsion.

6.1.3 - Microscopic dynamics portrayed by XPCS

Going from the macroscopic to the microscopic investigations, the intrinsic dynamics of the GNP network has been measured by recording the X-ray intensity scattered from the sample in the grazing-incidence diffraction experiment (see section 4.2), at several values of Φ and in correspondence of different values of the components of the scattering vector in the directions parallel ($q_{\parallel}$) and perpendicular ($q_{\perp}$) to the air/water interface.
The acquisition of the scattered intensity is processed just dividing the pixels of the 2D detector into square groups, each of which is

labeled by its scattering vector components ($q_\parallel$, $q_\perp$). From the scattered intensity measured by each group of pixels as a function of time we calculate the intensity autocorrelation function:

$$g^{(2)}(q_\parallel, q_\perp; t) = \frac{\langle I(t_0) I(t_0+t)\rangle_{t_0}}{\langle I(t_0)\rangle^2_{t_0}} \qquad \text{Eq. 1}$$

In soft-matter experiments, the correlation functions are commonly described using the empirical Kohlrausch-William-Watts (KWW) exponential

$$g^{(2)}(q_\parallel, q_\perp; t) = A + \beta e^{-2(t/\tau)^\gamma} \qquad \text{Eq. 2}$$

in which:

- β is the contrast
- τ is the relaxation time of the dynamics
- γ, called the shape parameter, is connected to the kind of dynamics that characterizes the system together with the dependence of τ on q.

We briefly recall here that, in the case of Brownian dynamics, $\tau \propto q^{-2}$ and $\gamma = 1$; pure ballistic motion shows $\tau \propto q^{-1}$ and $\gamma = 2$ [Berne2000]; while more complex systems display some intermediate behavior, e.g. many arrested systems show a compressed shape often with $\tau \propto q^{-1}$.

Figure 6.4 reports data and fit models for correlation functions measured at $\Phi = 15\%$. The initial contrast of the correlation functions shows a clear dependence on q. Usually, when additional relaxation processes faster than the exposure time are present, they cause a sort of "blurring" of the speckle pattern. This implies a reduction of the contrast β with respect to its theoretical value β_0; this reduction depends on q following a pseudo-Debye-Waller decay [Grubel2008] ruled by the localization length $r_{loc} = \sqrt{\langle u^2 \rangle}$:

$$\beta = \beta_0 exp\left(-\frac{q_\parallel^2 \langle u^2 \rangle}{3}\right) \qquad \text{Eq. 3}$$

This is clearly the case for our data, as inspection of **Figure 6.4** shows that the initial contrast is well below the theoretical value, which in our experimental geometry is approximately $\beta_0 = 0.2$.

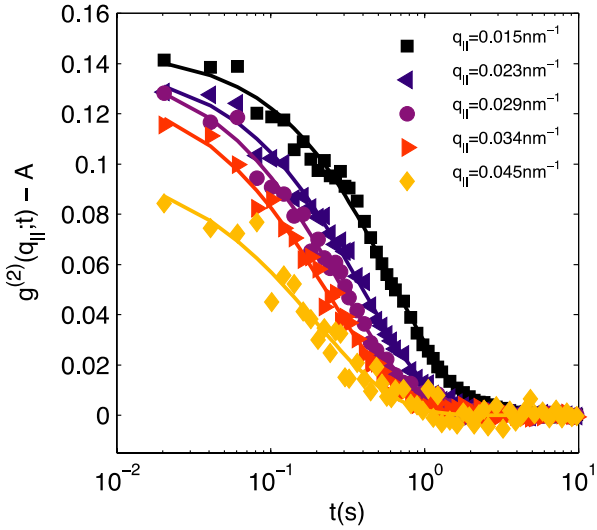

Figure 6.4 Correlation functions decay as KWW exponentials measured at Φ = 15% at several values of q. Continuous lines are fits to the KWW phenomenological law.

In **Figure 6.5a** we report the q dependence of β together with the fits based on Eq. (3). By this analysis, the localization length r_{loc} can be extracted, as reported in **Figure 6.5b**. At low concentration, the value of r_{loc} decreases linearly with increasing Φ, reaching a value compatible with the particle's diameter (8 nm) at about 22%; then this decrease saturates at higher concentrations. The linear decrease is marked by the black line in **Figure 6.5b**. The initial decrease of r_{loc} may be interpreted as if the fast single-nanoparticle motion becomes more and more hindered by the spatial constraints imposed by neighbors, while interfacial aggregates are formed. Then the saturation of r_{loc} above 22% is consistent with the idea that, at this stage, individual NPs are localized within the gel branches, confined by nearest neighbors [Orsi2014]. Further increasing concentration affects the slow dynamics of the whole film, but not the localization length due to fast motion of single NPs.

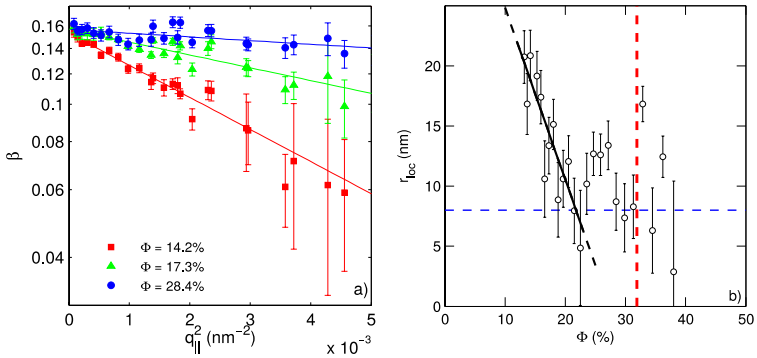

Figure 6.5 The contrast decays with $q_{\parallel}$ following a pseudo-Debye-Waller dependence is reported. (a) Data for three different concentrations are plotted on a semi-logarithmic scale as a function of the squared scattering vector. Lines are fits to Eq. (3). (b) Localization length r_{loc} as a function of concentration: with increasing Φ it decreases to reach a value comparable with the size of an individual nanoparticle (8 nm, horizontal dashed blue line). The vertical red line represents the percolation threshold.

Focusing on the relaxation time τ and on the shape parameter γ, that highlight the nature of the intrinsic dynamics of the 2D network, in **Figure 6.6a** we report the values of τ obtained from the fits to the KWW relation of the correlation functions measured at Φ =15%. In agreement with our previous investigations [Orsi2012], we find that τ depends only on the parallel component $q_{\parallel}$ of the scattering vector q, which varies on the horizontal axis in the figure, and not on the perpendicular component $q_{\perp}$, thus confirming that the dynamics is confined at the air/water interface. Therefore, in all the subsequent analysis, we averaged the results along $q_{\perp}$ to improve the statistics. We also find that τ scales always as $\tau \propto q_{\parallel}^{-n}$ (**Figure 6.6b**) with n of the order of 1 (**Figure 6.6b**), a feature common to many arrested systems.
Notably, the shape exponent γ, shown in **Figure 6.6c**, varies as a function of $q_{\parallel}$ and of the concentration Φ. In the range covered by the present study, we are able to document a transition from a stretched ($\gamma < 1$) to a strongly compressed ($\gamma > 1.6$) shape as the concentration is increased and $q_{\parallel}$ is decreased.

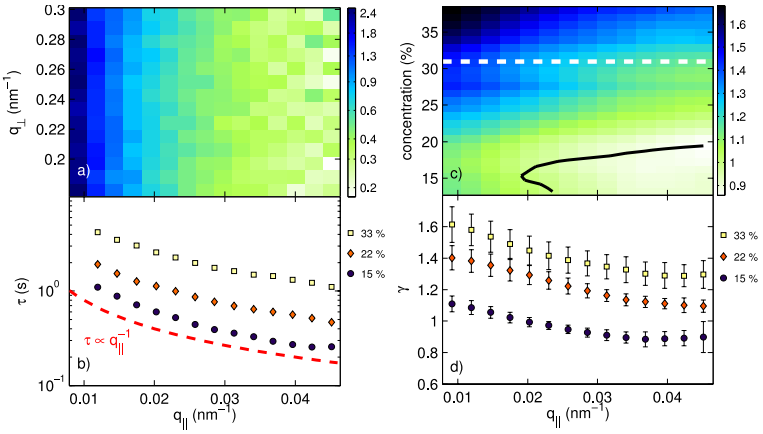

Figure 6.6 Both the relaxation time τ and shape exponent γ decrease at large $q_\parallel$. (a) Map of relaxation time τ as a function of the two components of the scattering vector, $q_\parallel$ and $q_\perp$, for Φ = 15%. Values of the color scale are in seconds. (b) Detailed dependence of τ on q measured at different concentrations (Φ = 15%, 22%, 33%). The $\tau \propto q^{-1}$ behavior is also shown for comparison (dashed line). (c) Shape parameter γ as a function of $q_\parallel$ and of Φ. The black line represents the contour of γ = 1, i.e. of simple exponential decay, while the white dashed horizontal line indicates the critical concentration (see text). (d) Detailed $q_\parallel$ dependence of γ for the same concentrations as in (b) (Φ = 15%, 22%, 33%).

The contour line marks the threshold value of γ = 1, corresponding to simple exponential decay, while the dashed line indicates the threshold concentration for the onset of the percolative cluster. The observed change in shape is a signature of a change in the physical mechanism responsible for the underlying dynamics. While a stretched shape would suggest a distribution of Brownian diffusors, with a heterogeneous distribution of relaxation times, the transition to a compressed shape, accompanied by n ≈ 1, is a signature of an arrested system. In literature are reported similar stretched-compressed dynamical crossovers in a few different out-of-equilibrium materials [Caronna2008, Ruta2012, Angelini2013].
The complex dynamics of our system are not trivial to interpret on a microscopic scale. A compressed relaxation is predicted within a detailed model proposed by Bouchaud and Pitard [Bouchaud2001] for the dynamics in a generic elastic solid. Within this model, randomly appearing dipolar stresses generate a field of strains in the network of the elastic gel. It is then assumed that the dynamics of the diffusors is determined by the relaxation of such local strains, leading to the compressed shape of the correlation

functions. This detailed model, however, puts strict constraints on the q dependence of γ (predicting two regimes, γ =1.5 for small q and γ =1.25 for large q), which do not agree with our data.
A more phenomenological model is put forward by Duri and Cipelletti some years ago [Duri2006]. Those authors attribute the compressed shape for the relaxation found in DLS and XPCS experiments to rare, intermittent rearrangements. They deduce a variation of the shape from compressed with γ = 1.5 to simple exponential as a function of the reduced scattering vector, obtained by scaling q by a typical length δ characterizing the displacement. In this case, the lower limit to the shape parameter (γ = 1) is dictated by the regime in which a single displacement is sufficient to fully decorrelate the signal. The variation of γ predicted by this model is manifestly more limited than what we observe. It is possible however that a similar model may hold in our case, if a spatially heterogeneous distribution of relaxation processes generates a distribution of relaxation times, leading to γ < 1. On the other hand, the upper limit of the range (γ = 1.5) predicted by this model is connected with the power law decay of the probability distribution function of the displacements ΔR observed in the gel.

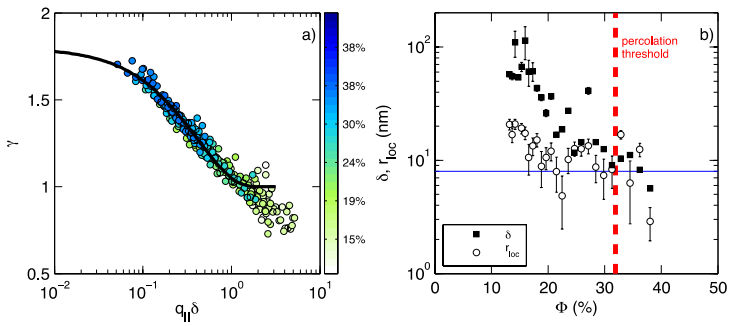

Figure 6.7 Master curve built from γ as a function of the scaled scattering vector at different Φ. (a) $\gamma(q_{\parallel})$ curves are shifted along the x axis by the scaling length δ so that they overlap. The resulting master curve is in partial agreement with the model (solid line) proposed by Duri and Cipelletti [Duri2006]. (b) Long-time displacement length δ as a function of Φ, compared with the short-time localization length r_{loc}. δ becomes comparable with the particle size (8 nm, horizontal line) and r_{loc}, above the percolation threshold (vertical dashed line).

This distribution is assumed to be Lévy-like [Duri2006, Cipelletti2003] with its tail towards large ΔR being proportional to

ΔR^{-p} with $p = \gamma + 1 = 2.5$. Therefore, our results ($\gamma = 1.8$ at low q and high concentration) would imply a steeper decay of the displacements' probability distribution in the low-q and large-Φ regime, leading to an increased ballistic-like character of the dynamics.

Encouraged by these considerations, we compare our results with a variant of the model proposed in [Duri2006]; the values of γ, measured at each concentration, are then plotted in **Figure 6.7a** on an adimensional axis provided by the scaled scattering vector $q_{\parallel}\delta$ so that they overlap, collapsing on a master curve, in analogy with Figure 3 of [Duri2006]. In this construction, an overall scale factor needs to be determined. This is accomplished by noting that for $q_{\parallel}\delta = 2$ the model predicts $\gamma = 1$; therefore the absolute values of δ can be determined. The master curve thus obtained is in agreement with the model curve up to $q_{\parallel}\delta = 2$, above which value the model would plainly predict $\gamma = 1$, while we observe a stretched shape. As anticipated, this can be reconciled with the model if we assume that in our case we observe a spatially heterogeneous distribution of relaxation times. The scaling parameter δ, reported as a function of Φ in **Figure 6.7b**, naturally offers us an estimate of the "long-time displacement length," i.e. of the dynamics taking place on the time scale of τ. In the same figure, it is compared with the "short-time localization length" r_{loc}, deduced from the Debye-Waller decay of the contrast, which on the contrary characterizes the length scale of the fast dynamics. While it is notable that a single framework is able to describe the dynamics of this system over a broad range of concentrations, detailed inspection of the figure suggests that two different regimes exist, above and below the percolation threshold: below it, the length scales r_{loc} and δ of the fast and slow dynamics decouple, while above it they become equal within experimental accuracy, and also comparable to the size of a single nanoparticle.

At the moment, to work out a more rigorous model that can take into account these data in detail, we are trying to establish a collaboration with Luca Cipelletti and his research group based in Lyon, France.

6.2 - From gold nanoparticles network to the DPPC-silica nanosystem

The study on gold nanoparticles stabilized by dodecanethiols highlights the strong tendency to the aggregation increasing the surface concentration. The interesting result, in terms of understand the mechanism of internalization of nanostructures by the cells, consists on the phenomenology related to the change of surface pressure: just raising the pressure, the nanoparticles -before Brownian free diffusors- start to create small disk-like aggregate and then the sticking of these disks produces an elastic rigid network.
In this sense, the investigation on 2D network of gold nanoparticles takes the form of a negative control because even if the spherical shape should allow the nanoparticles to diffuse everywhere in tissues where are injected, the real scenario is more complicated and not only related to the shape of the nanostructure considered. In particular, extrapolating the mechanism of network formation revealed by this study, it's possible to imagine that if we inject a certain amount of nanoparticles in a cell culture, locally the concentration could be enough to induce the formation of aggregates that i) can grow as rigid networks and then, ii) stick on cells surface. As we explain, the coupling between the "short-time localization length" r_{loc} and "long-time displacement length" δ after the percolation threshold means that the formed network behaves as a "single entity": this can promote an internalization process similar to that of the conjugated NWs. As a result the change in the shape of the nanostructures is partially effective for enhancing the nanostructure's spreadability but it has to be followed by a careful choice of the surface coverage in order to forbid the formation of aggregates and to have the best efficiency in singlet oxygen generation. The importance in the smart design of this nanostructure is clear if we imagine the complexity of a living system or of a cell culture, in which there are a lot of interfaces (e.g. cell membranes, tissues etc.) and compounds (some hydrophilic, some lipophilic) that can interact with the nanoparticle just

blocking it (e.g. on a cell membrane before internalization) or covering it (e.g. proteins that are tangled on NPs surface).
For these reasons, the study has to go deeper in the direction of understand the interactions of nanoparticles surface with the cells membrane. Therefore, we studied a model nanosystem based on silica nanoparticles allowed to interact with a phospholipid layer, chosen as the paradigm of an ideal interaction between an oxide nanoparticle and the basic constituent unit of cell membranes.

6.3 - DPPC Langmuir monolayer interacting with silica nanoparticles

We choose DPPC because it is the most abundant phospholipid in cell membranes and in the lung surfactant; the cellular tissues and fluid are constituted by DPPC for about 40% in weight of their total solid content [Boal2012].
At the same time, nanoparticles are widely utilized and Silica NPs [Santini2012] are among the most utilized in many applications. In addiction, the system silica NP/DPPC is quite important for possible hybrid bio-inorganic applications as the previously described porphyrinated NWs (section 5.4). The link is to be found in the kind of surface exposed to the environment (SiO_x in both cases) and not in the shape, extremely different between NPs and NWs systems. In this sense, DPPC/silica NPs could be a good model to improve the knowledge on the interactions between porphyrinated NWs and the cells membrane for the in-vitro experiments on singlet oxygen production. In fact, many studies have shown that the incorporation of NP in PL layers causes significant changes in the structural properties of these monolayers, such as changes in the 2D phase behavior and of the surface elasticity in the solid states [Guzman2012, Sosnowski2011].

6.3.1 - DPPC as simplest cell membrane model

Dipalmitoylphosphatidylcholine (DPPC) is a phospholipid consisting of two saturated palmitic acids linked to a phosphatidylcholine head (**Figure 6.8**).

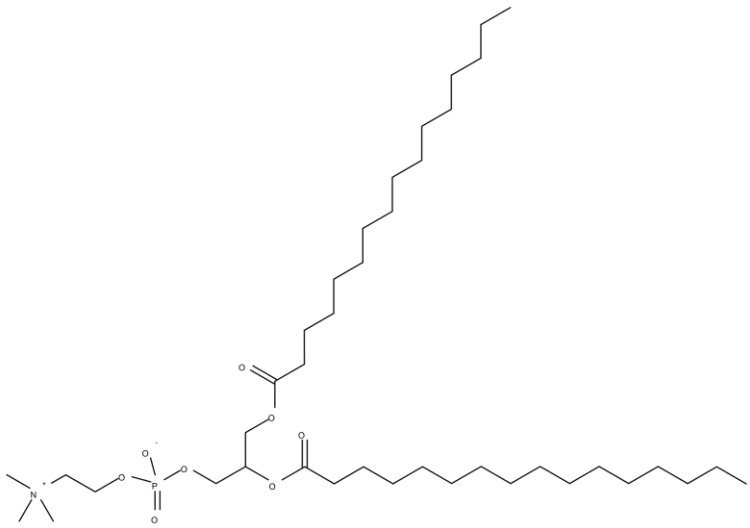

Figure 6.8 Structure of the DPPC molecule.

Because of its biological role, self-assembling and phase behavior at the aqueous interface has been extensively investigated [Möhwald1990].
In brief, in **Figure 6.9** are shown the Langmuir Π-A isotherms for different temperatures of the trough water bath. The temperatures span from 10° C to 30°C, always below the gel-liquid transition temperature of DPPC (41°C [Hirsh1998]). Above 15° C are visible all the typical regions of the DPPC isotherms as:

- The gas-liquid expanded (G-LE) phase transition
- The liquid expanded phase (LE)
- The liquid expanded-liquid condensed (LE-LC) coexistence
- The liquid condensed (LC) phase
- The solid phase with the final collapse

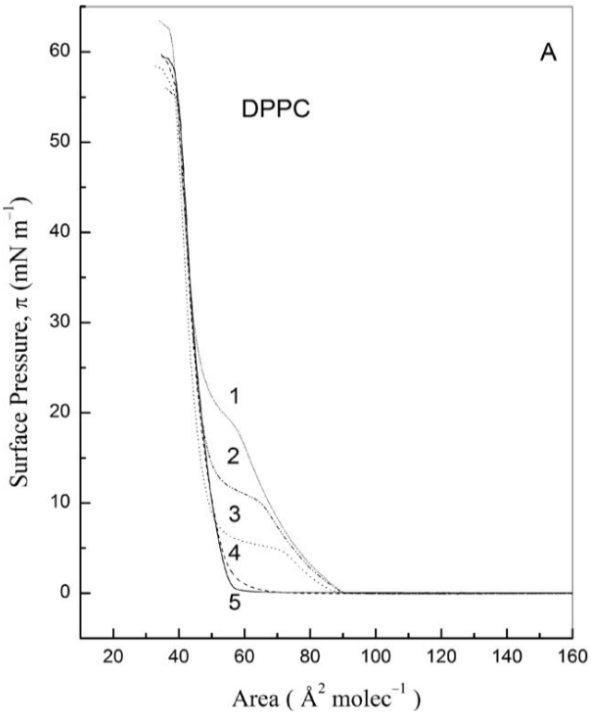

Figure 6.9 Langmuir DPPC isotherms acquired at different temperatures: respectively at 30° C (1), 25° C (2), 20° C (3), 15° C (4) and 10° C (5). Taken from [Toimil2010].

The presence of the coexistence LE-LC plateau is peculiar of phospholipids and very interesting because of the presence of peculiar domains structure (**Figure 6.10**) revealed through epifluorescence measurements during the film formation by compression. This region and the relative domains structure are very sensitive to the presence of other components in the monolayer besides to the temperature, as shown in **Figure 6.9**.

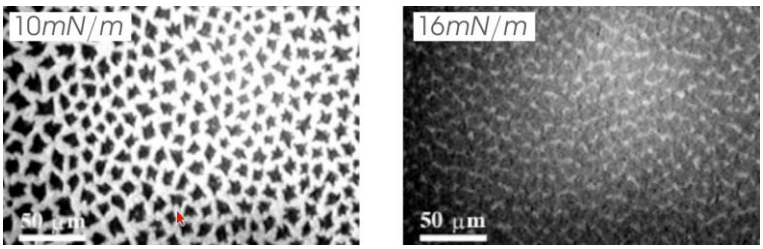

Figure 6.10 DPPC domain structure in the LE-LC coexistence region acquired with an epifluorescence microscope at 25° C, taken from [Hélène2003].

6.3.2 - To obtain the mixed interface

The investigated NP suspensions are obtained by dilution with pure water of different commercial colloidal dispersions products: Levasil 300/30, Levasil 200/30 and Levasil 50/50, all from H.C. Starck (Germany). The NPs in the three dispersions are spherical and narrowly distributed around diameters of 9, 15 and 60 nm, respectively. The dispersions are extremely stable because of the large negative surface charge of the particles, obtained in the specific production process. The NP ζ-potential is in fact -42 mV and the dispersions pH is around 9. Thus the dispersions do not contain any stabilizing agent which could interfere with the studied properties. This is also confirmed by the measurement of the surface tension which provides for all dispersions values similar to those of pure water: about 72.5 mN/m, stable for several hours.

DPPC (MW 734.1 g/mol, purity 99%) is supplied by Sigma (Germany) and used without further purification. Pure water is produced by a two stage system (Millipore, Elix plus Milli-Q) providing a resistivity greater than 18 MΩ·cm and a surface tension of 72.5 mN/m without any appreciable kinetics over several hours.

For the micro epifluorescence measurements, a small quantity of the fluorescence probe NBD-PC, (Avanti Lipids) was added to the spreading solution of DPPC (1%wt of the total lipid content). NBD-PC distributes preferentially in the liquid expanded phase [Nag1993].

The Langmuir monolayers is prepared using a Langmuir trough, cleaned with organic solvents and filled with a suspension of colloidal particles (1% wt concentration). The subphase temperature is controlled by means of water circulation between the trough basement and a LAUDA thermostat, set at 20°C.
Small constant velocity drifts of the Langmuir film are inevitable: in order to minimize them, a steel ring (1cm diameter) is placed in the subphase, centered under the measurement region. There, it reduces the subphase depth around the measurement region, effectively minimizing subphase motions. A chloroform solution of DPPC is spread at the interface between air and the aqueous suspension of NP. A waiting time of 1 hour is considered, to allow equilibration between NP and DPPC in the region close to the interface. Subsequently, the trough's area is reduced by means of the barrier motion, to reach the desired surface pressure value.

6.3.3 - Silica nanoparticles as DPPC circular features stabilizers

As a general trend, the incorporation of NPs, independently of their nature -hydrophilic or hydrophobic- and concentration, shifts the surface pressure-area isotherms of DPPC monolayers to higher areas per molecule [Guzmán2012], which can be only partially explained by the excluded area effect. Moreover, DPPC is well known to have two distinct liquid phases, called liquid expanded (LE) and liquid condensed (LC) with a first order phase transition and a notable coexistence plateau in the Langmuir isotherm.

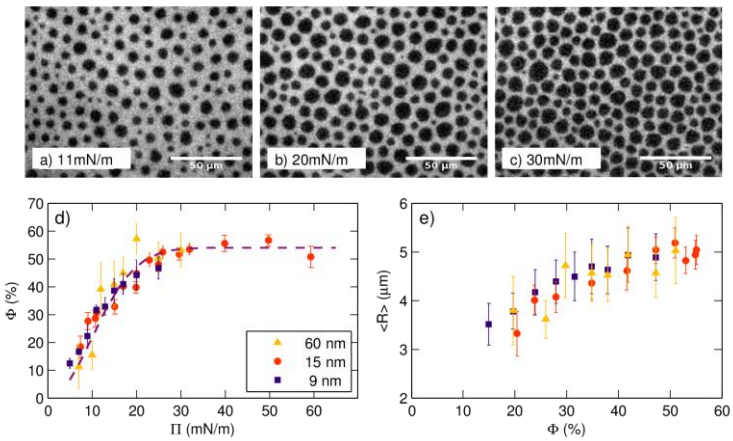

Figure 6.11 Coexistence of LC DPPC phase into the LE matrix, stabilized by silica NPs. a-c) Images taken at Π=11, 20, 30 mN/m at the epifluorescence microscope. The scale bars are 50µm long. d) Trend of the fraction of interface Φ covered by circular features vs. surface pressure Π; a saturation value is reached for Π>30%. The dashed line is a guide to the eye. e) Mean radius R of circular features, measured as a function of Φ for different values of the NP radius.

In a previous characterization [Guzmán2014], we have shown that NP are incorporated in the film when surface pressure is zero; upon compression, a mixed NP/DPPC phase if formed, which coexists with pure DPPC LC phase. Fluorescently labeled molecules are confined and blocked in the mixed phase; therefore, pure DPPC regions appear black in epifluorescence imaging (**Figure 6.11**): even at the highest attainable pressures, the film morphology is characterized by these black, circular features which are deemed to be the phantoms of the LC domains. At high surface pressure, they form a closely packed gel-like arrested state.
The fraction Φ of air/water interface covered by the circular features has been measured by accurate thresholding the epifluorescence images. As Π is increased, it increases up to 54% (**Figure 6.11d**): this saturation value is reached at Π>30mN/m. On panel e of the same figure we report the average feature radius R as a function of Φ: in the explored range the change in the feature size is limited, and the size value saturates above 45%.
The results reported in **Figure 6.11** is consistently reproducible; therefore, we are able to exploit the one-to-one correspondence between Π and Φ (through the 2D geometry provided by Langmuir

layers) to assign a specific structural state to the system in correspondence of specific values of Π, even when a direct microscopy measurement is unfeasible (e.g. during XPCS measurements). As shown in **Figure 6.11**, the observed phenomenology is found to be independent from NP's size.

6.3.4 - Micro-tracking of the features in direct space

A direct approach to the measurement of the dynamics is to track in time the position of the black, circular features that characterize the film morphology.
Their nearly circular shape simplifies the measurement of their position in epifluorescence images; we follow their displacement in time by recording videos and performing accurate position tracking. From the trajectories measured at different values of Φ, we calculate the mean square displacements (MSD); results are reported in **Figure 6.12a** for features with R=5.0±0.2 μm. We observe two distinct regimes. At low surface concentration (Φ=30.6%) MSD grows linearly as a function of time, indicating Brownian diffusion; as the packing is increased, the long-time MSD displays a sublinear trend, indicating that the diffusion is slowed down by the presence of adjacent objects.
To investigate both diffusive and subdiffusive regimes, we introduce an "effective" diffusion coefficient defined as:

$$D_{eff} = \frac{1}{4}\frac{d\langle \bar{x}(t)^2 \rangle}{dt}\Big|_{t=t^*} \qquad \text{Eq.1}$$

which represents the slope of the MSD curve at time $t = t^*$. **Figure 6.12b** reports the mean values, and their standard deviation as error bars, for the effective diffusion coefficients measured at $t^* = 2s$ (where the MSD grows linearly in time), for selected values of Φ, as a function of the inverse of the radius. Notably, at low surface concentration (Φ=30.6%) -where we observe Brownian motion- the diffusion coefficient is inversely proportional to the radius, thus following the behavior predicted by Hughes,

Pailthorpe and White [Hughes2006, Camley2011] for large, thin disks diffusing at the interface.

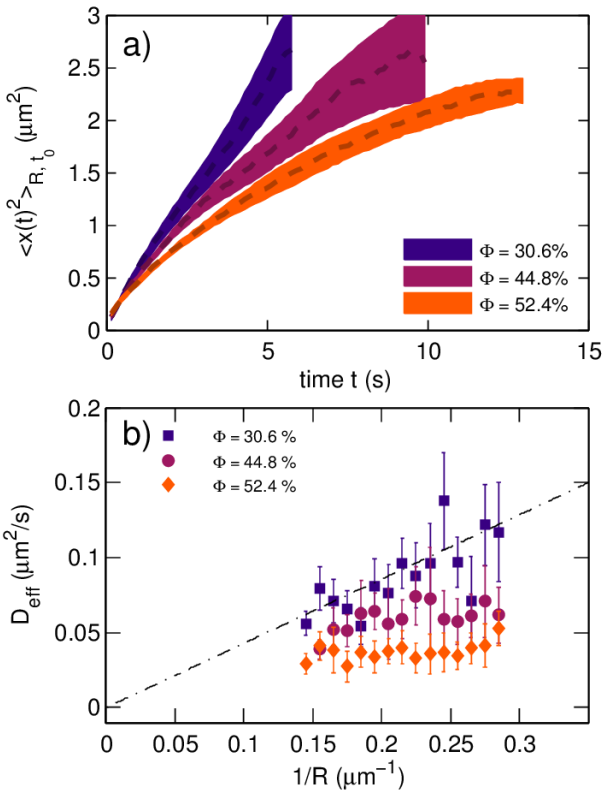

Figure 6.12 a) the MSD of circular features with R=5.0±0.2 μm grows linearly in time at Φ=30.6%, indicating diffusive dynamics. Sublinearity is observed at Φ=44.8% and Φ=52.4% on the time scale t>2 s. MSD have been averaged over the ensemble of domains with the same radius and on starting time t_0; color regions indicate standard deviations. b) The average values for the effective diffusion coefficient D_{eff} at t=2s are reported as a function of the inverse of 1/R. Error bars are standard deviation. While for Φ=30.6% $D_{eff} \propto 1/R$ in agreement with Eq.2, at higher values of Φ the dependence becomes sublinear.

This regime -in which lateral diffusion is limited by the drag exerted by the subphase, not by the surrounding 2D film- was verified experimentally by Klingler [Klingler1993] for large phospholipidic domains. In this case, the model predicts:

$$D_0 = \frac{k_B T}{8\eta R} \qquad \text{Eq.2}$$

where T=20°C and η is the subphase viscosity, which in the case of the NP containing subphase, was measured using a capillary viscometer and resulted η=1.2 mPa/s, marginally larger than pure water at the same temperature.
As Φ is increased, we observe a reduction of the diffusion coefficient, because of the increasing hindrance caused by surrounding neighbors objects, analogously to what happens in highly concentrated colloidal suspensions [Götze1999]. As a result, the diffusion coefficient becomes independent from their size. In principle this could be ascribed to the onset of the Saffman-Delbruck [Saffman1975] regime, which predicts a weak logarithmic dependence of diffusion coefficient on the radius. However, this cannot be the case as the Saffman-Delbruck length (defined as $L_{SD} = \eta_m/(2\eta)$ where η_m is the 2D viscosity of the phase that surrounds the diffusor) results much shorter than R:

$$\frac{L_{SD}}{R} = \frac{\eta_m}{2\eta R} \ll 1 \qquad \text{Eq.3}$$

We remark that the Hughes regime implies the impossibility of inferring the viscosity of the mixed DPPC-NP phase from the dynamics, since the drag from the subphase dominates the diffusion (Eq. 2).

6.3.5 - Intermittent dynamics of DPPC features: an XPCS study

The tracking analysis performed in direct space evidences the presence of a transition between two dynamical regimes: a low-Φ regime characterized by Brownian-like diffusion, and a slower high-Φ regime. The onset of this slower regime, however, exposes the limits of micro-tracking: the diffusion length scale gets shorter as the surface concentration of the circular features increases, becoming comparable with the uncertainty in the determination of

the feature's position. The complementary GI-XPCS technique allows a quantitative characterization of the dynamics, providing insights into shorter spatial scales and faster times (up to 1ms) with respect to the ones accessed by direct imaging.

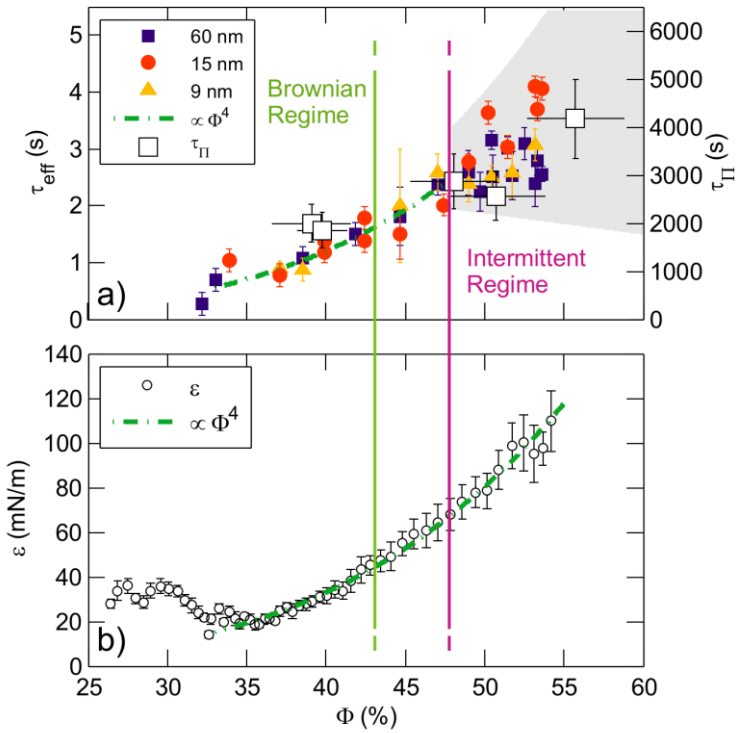

Figure 6.13 At low Φ, the relaxation time increases with Φ in the same fashion as the dilational elasticity ε. For Φ>43% the intermittent rearrangements of the high-Φ regime provide a relaxation mechanism that eludes dynamical arrest and the divergence of τ_{eff}. a) XPCS relaxation time $\tau_{eff}(\Phi)$ (filled symbols, left axis); colors indicate different NP sizes. A compatible trend is shown by the time τ_Π taken by surface pressure to reach its equilibrium value after a sudden compressional deformation (empty symbols, right axis) b) The dilational elasticity ε (left axis) steadily increase as Φ^4. The dash-dot lines are fits to a Φ^4 dependence.

In a similar way as for 2D network of gold nanoparticles described in section 6.1, we found the intensity autocorrelation functions decays as Kohlrausch-William-Watts exponentials

$$g^{(2)}(q_{\parallel};t) = A + \beta \exp\left(-2\left(\frac{t}{\tau(q_{\parallel})}\right)^{\gamma}\right). \qquad \text{Eq. (1)}$$

Therefore, we describe the evolution of the dynamics as a function of Φ in terms of changes in the relevant parameters of the fit. In particular, we focus on the time-scale τ and on "fingerprints" of the dynamical character, the shape of the correlation function represented by the stretching exponent γ and the dependence of the relaxation time from $q_{||}$. In combination, their values allow to discriminate between diffusive ($\gamma = 1, \tau \propto {q_{\parallel}}^{-2}$) and ballistic ($\gamma = 2, \tau \propto {q_{\parallel}}^{-1}$) motions.

We found a dynamics confined at the air/water interface and its relevant parameters depend only on the component of the scattering vector parallel to the interface. To take into account the effects of possible changes of shape of the exponential decay we express the relevant time scale of the dynamics using an effective relaxation time

$$\tau_{eff}(q_{\parallel}) = \tau(q_{\parallel}) \frac{\Gamma\left(1/\gamma(q_{\parallel})\right)}{\gamma(q_{\parallel})} \qquad \text{Eq. (2)}$$

where Γ is the gamma function: results are reported in **Figure 6.13a**. We note that all the measurements are compatible at Φ<48%, while a large amount of irreproducibility is evident at higher concentrations. In order to gain some insight on the physical mechanism underlying this relaxation, it is instructive to compare the behavior of $\tau_{eff}(\Phi)$ with that of the mechanical moduli. Therefore, we calculated the dilational elasticity ε= -A(dΠ/dA) from the Π-A isotherm, which is reported in **Figure 6.13b** as a function of Φ. We found that in the concentration region Φ>35%, the mechanical modulus grows as $\varepsilon \propto \Phi^4$. We also found that the same algebraic law Φ^4 trend holds also for $\tau_{eff}(\Phi)$ as well as the stress-relaxation time τ_{Π} (**Figure 6.13a**) obtained in stress-relaxation experiments in which the film's surface is suddenly compressed and then is allowed to reach its quasi-equilibrium [Cicuta2007].

Interestingly, with the steady increase of the relaxation time we find evidence of a phase transition between two different dynamical states; we observe a continuous change of the shape of

the correlation function and of the q-dependence of the relaxation time, as shown in **Figure 6.14**.
At low Φ, below 40%, the dynamics is Brownian: correlation functions decay as simple exponentials (γ≈1) and the relaxation time decays as $\tau \propto q^{-2}$. As the surface pressure is increased, the shape increase linearly towards faster-than-exponential decays (γ≈1.6) with $\tau \propto q^{-1}$, a dynamics commonly found in systems undergoing dynamical arrest [Orsi-Madsen2012, Caronna2008].

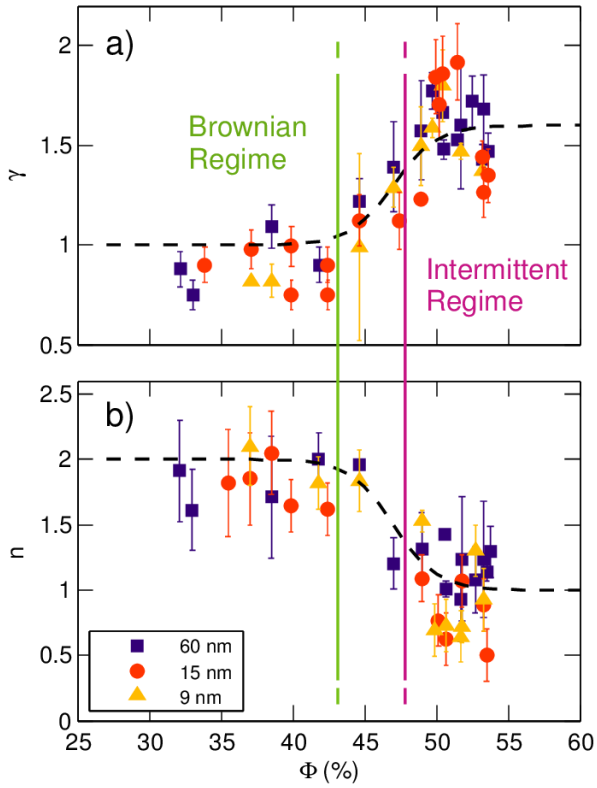

Figure 6.14 Dynamical phase transition from a diffusive regime (Brownian motion) to a regime of intermittent rearrangements of the sample's structure triggered increasing the packing fraction of circular features. (a) The shape parameter γ increase from 1 up to γ>1.5 as Φ grows from 40% to 50%. (b) In the same Φ range, the τ(q) dependence switch from $q_{||}^{-2}$ to $q_{||}^{-1}$. Colors indicate different NP sizes.

In order to test whether the nanoparticle size plays any role in this phenomenology, we tried varying the NP size, using 9nm, 15nm

and 60nm particles. As the results displayed in **Figure 6.13a** and **Figure 6.14** demonstrate, the nanoparticle size plays no noteworthy role in this phenomenology (different NP size is indicated by different colors), in the same way as the nanoparticle size is not affecting the structure of the system, as shown in **Figure 6.12**.

6.3.6 - Discussion on the dynamical transition induced by film's compacting

From the comparison of data obtained from the two techniques, we can draw a consistent picture of the evolution of the dynamics, with a degree of insight that would not have been possible otherwise.
At surface concentration (Φ<44%), we find that the circular features perform 2D diffusive motions. The diffusivity is appropriately described by a model, which applies to 2D inclusions, in which the drag from the subphase (proportional to the area) dominates that from the mixed NP-DPPC phase (proportional to the perimeter) [Huges2006, Campley2011, Klingler1993]. Consistently, GI-XPCS correlation functions decay as simple exponential.
The increase of dynamic relaxation times and the increase of the quasi-static dilational compressibility with increasing packing fraction unveil information on the inter-feature interactions that characterize the system. All follow the same Φ^4 dependence as shown in **Figure 6.13**. This dependence is much weaker than the $(1-\Phi/\Phi_c)^{-2}$ regime connected to a hard disks repulsive potential. At the same time is known that in monolayers of phospholipids (DPPC/POPG) mixed with palmitic acid or n-hexadecanol, which exhibit LC/LE phase-coexistence, the viscosity increases following a $(1-\Phi/\Phi_c)^{-1}$ law due to a long range electrostatic potential between LC domains [Ding2002]. The much weaker dependence found in our system may be connected to the presence of NPs around the circular features, whose electrostatic charge may screen the long range electrostatic inter-feature potential. This is also supported by the fact that similar power law trends have been

found in many core-shell 3D colloidal systems, e.g. in star-like micelles or in soft PNIPAM spheres in which a Φ^7 dependence was found [Koumakis2012]. In our system, the mixed DPPC/NP matrix may act as an outer shell layer surrounding the compact circular features, resulting in an effective 2D core-shell system. It is interesting that the NP size does not have play any role in the range investigated.
The signal-to-noise ratio in our data was not sufficient to calculate higher order correlation functions, from which the presence of intermittency and dynamical heterogeneities could be investigated.

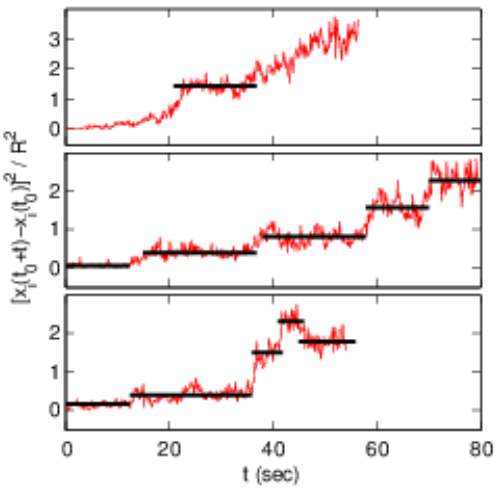

Figure 6.15 The square displacements of three different objects measured at Φ=52.4% reported as a function of time and normalized to the square of the domain's radius, R^2. Black lines highlights the time regions characterized by rattling movements.

Nevertheless, the presence of intermittent rearrangements inferred by the interpretation of XPCS measurements is directly confirmed by micro-tracking. As shown in **Figure 6.15**, the square displacements (i.e. not averaged neither over the statistic ensemble, nor over the initial time t_0) for three different circular features presents long periods of slow diffusion or vibrational motion around a static position, followed by sudden long jumps over distances larger than R. These random, hyperdiffusive jumps are

commonly marked in the literature as the cause of the compressed shape of XPCS correlation functions [Duri2006, Berthier2011].

7 *Conclusions and future works*

In this thesis, I reported some studies of interfacial systems, focused on biomedical applications. I have performed structural and functional characterizations of multifunctional nanomaterials. I have also characterized the dynamics in two different Langmuir films, simplified paradigms of ideal interfaces.
In detail, the nanosystems investigated are:

- Supersonic beam depositions of fluorinated porphyrins $H_2TPP(F)$ on flat silicon/silica substrates, as idealized flat interfaces mimicking those of the real nanowires (see below);
- An hybrid nanosystem based on the coupling of 3C-SiC@SiO_x core-shell nanowires with the porphyrins derivative $H_2TPACPP$ for Self Lighting-PDT applications on cancer treatment;
- Core-shell nanoparticles based on CeF_3 surrounded by ZnO, prepared during my visit at University of Texas at Arlington in the group of Prof. Wey Chen;
- A Langmuir 2D network of gold nanoparticles at air/water interface to investigate the dynamics of interactions at nanoscopic scale;

- A Langmuir 2D mixed monolayer of DPPC/silica nanoparticles chosen as model system for study the interactions of hydrophilic nanoparticles with a model cell membrane.

I combined several complementary techniques for these studies. In particular, electron and probe microscopies (SEM, TEM, AFM) were employed to highlight the structural properties of nanomaterials and the morphology of the films surface while fluorescence techniques (microfluorescence, epifluorescence) was used to measure the optical properties of nanomaterials and to observe the morphology of Langmuir films. Moreover, several physical investigations were performed at the state of the art, such as:

- Irradiations (6 MeV) at the Varian linear accelerator placed at the Radiotherapy department of Parma Hospital to study the singlet oxygen production of porphyrinated nanowires and to evaluate their oxidative stress on cells (in vitro tests);
- Measurements of mechanical properties in Langmuir films through two different complementary techniques available in our group; the oscillating needle (ISR) and the oscillating barriers;
- XPCS available at the synchrotron ESRF of Grenoble (FR) to investigate the characteristic dynamics of Langmuir films at the nanoscopic scale.

The results have been discussed from the point of view of the interactions among nanomaterials themselves as well as between nanomaterials and the interfaces involved in biomedical applications. Therefore an accurate examination of the physical mechanisms behind the dynamics of these interactions was performed. Briefly, the more relevant outcomes are the following:

a. $H_2TPP(F)$ SuMBD depositions on Si(100) substrates shown a peculiar Stranski-Krastanov phenomenology. The growth has been layer-by-layer at the beginning followed by a three dimensional island growth; usually occurring in few monolayers, in our case, this continues for many deposition layers together with the growth of islands. This morphology was clearly displayed by AFM, and was confirmed by microfluorescence spectra and XPS measurements.

b. More stable and homogenous covering layers were then obtained by the "click chemistry" approach in which the organic/inorganic interface was formed on 3C-SiC@SiO_x core-shell nanowires by suitably functionalized with H_2TPACPP porphyrin. TEM images have shown the crystalline structure of the SiC core and the presence of an amorphous SiO_x shell while the appearance of the porphyrins Q-band emission, superimposed to the nanowires luminescence, have proved the effectiveness of the functionalization. The singlet oxygen generation, due to the nanosystem irradiation at 6 MeV, was effectively revealed by a marker kit (Singlet Oxygen Sensor Green, SOSG [SOSG2004]) in function of the released dose. Nevertheless during in vitro experiments, the effectiveness of oxidative stress was partially shaded by the short lifetime of the singlet oxygen (3-4 μs [Kuimova2009]), the shape of the porphyrinated NWs and the nature of the surface exposed to the environment.
c. A different approach to overcome these problems was then followed: I carried out a preliminary study on CeF_3@ZnO core-shell nanoparticles synthetized via wet chemical methods. Optical measurements have shown the simultaneous presence of both the CeF_3 and ZnO signals proving the synthesis of ZnO in the presence of CeF_3 seeds. Further SEM and TEM investigations need to be performed to investigate their structure.
d. At the same time, to understand aggregation processes at interfaces and arrested dynamics, a network of hydrophobic gold nanoparticles as a Langmuir monolayer at air/water interface has been investigated. The complete structural characterization was performed with in situ epi-microscopy in addition to SEM imaging of films transferred onto the silicon substrate. Mechanical measurements have shown that the structure behaves as a bidimensional elastic gel at all concentrations. Correlation functions, calculated from GI-XPCS experiments, have been reconcilable with a phenomenological model proposed by Duri and Cipelletti [Duri2006], which hypothesizes that the correlation of the scattered intensity is driven by rare intermittent

rearrangements of the network. According to the model, a master curve was built. Its scale factors, corresponding to the long-time displacement length δ, characterize the dynamics on the time scale of a few seconds. This is distinct from the short-time localization length r_{loc}, determined by the pseudo-Debye-Waller analysis of the initial contrast, which characterizes dynamics faster than 10 ms. However, as the concentration Φ increases towards the percolation threshold, was shown that the two lengths converge to a common limit comparable to the single-particle size.

e. Going ahead with the study, we investigated a Langmuir 2D mixed monolayer of DPPC/silica nanoparticles. Epifluorescence measurements have shown a stable NP/DPPC mixed matrix that surrounds regions composed of tightly packed DPPC molecules, phantoms of pristine DPPC LC domains. The mixed phase matrix suppresses the coalescence of these regions. Through the use of GI-XPCS, we have been able to measure the dynamics of these circular features. The dynamics is Brownian at relatively low concentration; as it is raised we observe a transition towards a new dynamical regime, featuring intermittent, cooperative rearrangements. These results indicate that a residual dynamics remains present even in the densely packed structure formed.

These studies of mixed interfaces examined either as fundamental studies and in view of future biological applications might be useful to understand the phenomenology and the behavior of nanostructures interacting with bio-membranes and interfaces e.g. cell membrane, organelles etc.

Future works

To face the problem of NWs internalization, NWs coated with an amino-polyethylene glycol (amino-PEG) derivative are currently being produced and characterized. The rationale is the optimization of the surface hydrophilicity just controlling the time of the reaction and the amount of the precursor. Moreover, because

of the flexibility of the "click chemistry" reaction, a future prospective -scheduled within BioNiMED project- will be the coupling of porphyrinated NWs with superparamagnetic nanoparticles combining the SLPDT mechanism with hyperthermia effect induced by radiofrequency magnetic fields. The resulting triple system could be the forefront of a new generation of nanomaterials for treatments on tumors.

A completely different approach to the same problem consists in keep working with much smaller objects, namely CeF_3@ZnO core-shell nanoparticles. The novelty of this approach is the combination of the efficiency of CeF_3 to convert X-rays in visible light with the biocompatibility and the various functionalization processes available for ZnO. In particular, the production of a hybrid nanostructure through the functionalization with photosensitizers and/or targeting molecules could be promising.

In the long term, obviously in vivo tests shall be performed on those systems that best performed in the in vitro tests.

At the same time, the experience acquired on the interaction between nanostructure and bio-membranes shall be used to investigate hyperthermia effect of superparamagnetic nanoparticles interacting with lipid layers. This effect has been well characterized -at a phenomenological level- both in vitro and in vivo; however, a fundamental study of the local mechanism of action is still lacking.

Acknowledgments

First of all I would like to express my gratitude to *Prof. Luigi Cristofolini*, his friendship has been at the basis of my professional and personal growth. He has been a precious scientific guide as well as a persistent source of advices and inspirations, during my everyday work.
I would also like to thank people of our group:

> *Dr. Davide Orsi* for the priceless help in the development of instruments software and in general for the everyday scientific support.
>
> *Dr. Paolo Camorani* for the practical support during measurements in laboratories.

For the precious help, for the priceless discussions/advices on several experiments and for the results interpretation, I would also like to acknowledge all the people related to the BioNiMED project, in particular:

Dr. Giancarlo Salviati, Dr. Francesca Rossi, Dr. Filippo Fabbri, Prof. Franca Bigi, Dr. Silvana Pinelli, Dr. Rossella Alinovi and Dr. Giovanna Benecchi.

I am also be grateful to *Prof. Wei Chen* of University of Texas at Arlington for having hosted me in his laboratories during my formative stage period. I would also like to thank all his group, *Dr. Lun Ma, Sunil Sahi* and *Brian Bui* for their precious availability.

Last but not least, as it is usual to say, an epic thank you to all my PhD students' colleagues for the support inside and outside of the university. Their unique friendship has given me the strength to go ahead in my work every day.

List of Publications

In this thesis are presented some results and discussions reported in the following articles, published or in submission on international peer-reviewed scientific journals.

- F. Rossi, E. Bedogni, F. Bigi, T. Rimoldi, L. Cristofolini, S. Pinelli, R. Alinovi, M. Negri, S. C. Dhanabalan, G. Attolini, F. Fabbri, M. Goldoni, A. Mutti, G. Benecchi, C. Ghetti, S. Iannotta and G. Salviati
  Porphyrin conjugated SiC/SiO_x nanowires for X-ray-excited photodynamic therapy
  Scientific Reports 5, 7606, 6pp (2015)

- D. Orsi, B. Ruta, Y. Chushkin, A. Pucci, G. Ruggeri, G. Baldi, T. Rimoldi and L. Cristofolini
  Controlling the dynamics of a bidimensional gel above and below its percolation transition
  Physical Review E 89, 042308 (2014)

- D. Orsi, E. Guzmán, L. Liggieri, F. Ravera, B. Ruta, Y. Chushkin, T. Rimoldi and L. Cristofolini
  Combining X-ray correlation spectroscopy with micro-tracking to portray a 2D dynamical arrest transition
  SUBMITTED to PNAS

- Study of H_2TPP(F) SuMBD depositions on native silicon oxide: from morphology to electronic interactions at the molecules/substrate interface
  in PREPARATION

Bibliography

[Ackroyd2001] Ackroyd R, Kelty C, Brown N and Reed M, Photochemistry and Photobiology 74, 656 (2001)

[Akins1996] Akins D L, Ozcelik S, et al., J. Phys. Chem., 100, 14390-14396, (1996)

[Allison2004] Allison R R, Downie G H, Cuenca R, Hu X H, Childs C J H and Sibata C H, Photodiag. Photodyn. Therapy, 1, 27–42 (2004)

[Angelini2013] Angelini R, Zulian L, Fluerasu A, Madsen A, Ruocco G, and Ruzicka B, Soft Matter 9, 10955 (2013)

[Bell1995] Bell S E J, Al-Obaldi A H R, et al., J. Phys. Chem., 99, 3959-3964 (1995)

[Berne2000] Berne B J and Pecora R, Dynamic Light Scattering (Dover, New York, 2000)

[Berthier2011] Berthier L Dynamic heterogeneity in amorphous materials. Physics (College Park Md) 4 (2011)

[Boal2012] Boal D, Mechanics of the cell (Cambridge University Press, Cambridge) 2nd Ed (2012)

[Bonnett1995] Bonnett R, Chem. Soc. Rev. 24, 19-33 (1995)

[Bouchaud2001] Bouchaud J P and Pitard E, Eur. Phys. J. E: Soft Matter Biol. Phys., 6, 231 (2001)

[Brooks1999] Brooks C F, Fuller G G, Frank C W and Robertson C R, Langmuir 15, 2450 (1999)

[Brust1994] Brust M, Walker M, Bethell D, Schiffrin D, and Whyman R, J. Chem. Soc. Chem. Commun., 801, (1994)

[Cacchioli2014] Cacchioli A, Ravanetti F, Alinovi R, Pinelli S, Rossi F, Negri M, Bedogni E, Campanini M, Galetti M, Goldoni M, Lagonegro P, Alfieri R, Bigi F, and Salviati G, Nano Lett. 14, 4368−4375 (2014)

[Camley2011] Camley B, Brown FLH Beyond the creeping viscous flow limit for lipid bilayer membranes: Theory of single-particle microrheology, domain flicker spectroscopy, and long-time tails. Phys Rev E 84:021904 (2011)

[Caronna2008] Caronna C, Chushkin Y, Madsen A, and Cupane A, Phys. Rev. Lett., 100, 055702 (2008)

[Castano2006] Castano A P, Mroz P and Hamblin M R, Nature 6, 535 (2006)

[Chandrasekhar1960] Chandrasekhar, S., Radiative Transfer (Dover Publications, Mineola, N.Y., 1960)

[Chen2006] Chen, W & Zhang J, J. Nanosci. Nanotech. 6**,** 1159-1166 (2006)

[Cicero2004] Cicero G, Catellani A and Galli G, Phys. Rev. Lett. 93, 016102 (2004)

[Cicuta2005] Cicuta P and Terentjev E M, Eur. Phys. J. E: Soft Matter Biol. Phys. 16, 147 (2005)

[Cicuta2007] Cicuta P, J Colloid Interface Science, 308:93–9 (2007)

[Cipelletti2003] Cipelletti L, Ramos L, Manley S, Pitard E, Weitz D A, Pashkovski E E, and Johansson M, Faraday Discuss. 123, 237(2003)

[Courrier2003] Courrier H M, Thierry F, Vandamme, Krafft M P, Nakamura S, Shibata O, Colloids and Surfaces A: Physicochem. Eng. Aspects 215, 33/41 (2003)

[Ding2002] Ding J, Warriner H, Zasadzinski J, Phys Rev Lett, 16–19 (2002)

[Dolmans2003] Dolmans D E J G J, Fukumura D, Jain R K, Nature Reviews Cancer 3, 5, 380-387 (2003)

[Duri2006] Duri A and Cipelletti L, Europhys. Lett. 76, 972 (2006)

[Egorov1989] Egorov S. Y. et al., Chem. Phys. Lett., 163, 421–424 (1989)

[Fabbri2010] Fabbri F, Rossi F, Attolini G, Salviati G et al., Nanotechnology 21(34), 345702 (2010)

[Götze1999] Götze W, Recent tests of the mode-coupling theory for glassy dynamics. J Phys Condens Matter 11:A1–A45 (1999)

[Gouterman1961] Gouterman M, Spectra of Porphyrins, J. Mol. Spec. 6, 138-163, (1961)

[Gouterman1963] Gouterman M, Spectra of Porphyrins - Part II, J. Mol. Spec. 11, 108-127, (1963)

[Grubel2008] Grubel G, Madsen A, and Robert A, in Soft Matter Characterization, edited by R. Borsali and R. Pecora (Springer, Berlin), pp. 935–995 (2008)

[Guzmán2012] Guzmán E, Liggieri L, Santini E, Ferrari M, Ravera F, Colloids Surfaces A Physicochem Eng Asp, 413:174–183 (2012)

[Guzmán2014] Guzmán E, Orsi D, Cristofolini L, Liggieri L, Ravera F, Langmuir 30:11504–12 (2014)

[Hélène2003] Hélène M. Courrier, Thierry F., Vandamme, M P Krafft, S Nakamura, O Shibata, Colloids and Surfaces A: Physicochem. Eng. Aspects, 215 33/41 (2003)

[Helms2008] Helms, V. Principles of Computational Cell Biology, Fluorescence Resonance Energy Transfer, Ch. 8.3.5 (Wiley-VCH, Weinheim, 2008)

[Hirsh1998] Hirsh D J, Lazaro N, Wrigth L R, BoggsJ M, McIntosh T J, Schaefer J and Blazyk J, Biophys. J., 75, 1858–1868 (1998)

[Hudson2005] Hudson R, Carcenac M, Smith K, Madden L, Clarke O J, Pélegrin A, Greenman J and Boyle R W, Br. J. Cancer 92, 1442 (2005)

[Hughes2006] Hughes BD, Pailthorpe BA, White LR The translational and rotational drag on a cylinder moving in a membrane. J Fluid Mech 110:349 (2006)

[Jalili2004] Jalili N, Laxminarayana K, Mechatronics 14, 907–945 (2004)

[Iannotta2003] Iannotta S, Toccoli T, J. Polym. Sci. B Polym. Phys. 41, 21, 1099-0488 (2003)

[Juzenas2008] Juzenas P, Chen W, Sun YP, Neto Coelho M A, Generalov R, Generalova N, Christensen I L, Advanced Drug Delivery Reviews 60, 1600–1614 (2008)

[Kaganer1999] Kaganer V, Mo̧hwald H, and Dutta P, Reviews of Modern Physics, 71, 779 (1999)

[Klinger1993] Klingler J, McConnell HM Brownian motion and fluid mechanics of lipid monolayer domains. J Phys Chem 2:6096–6100 (1993)

[Koumakis2012] Koumakis N, Pamvouxoglou A., Poulos A. S, Petekidis G, Soft Matter, 8:4271 (2012)

[Kuimova2009] Kuimova M K, Yahioglu G, and Ogilby P R, J. Am. Chem. Soc. 131, 332–340, (2009)

[Lal2008] Lal S, Clare S E and Halas N J, Accounts of Chemical Re-search 41, (2008)

[Liu2008] Liu Y, Chen W, Wang S & Joly A L, Appl. Phys. Lett. 92**,** 043901 (2008)

[Liu-Zhang2008] Liu, Y., Zhang, Y., Wang, S., Pope, C. & Chen W., Appl. Phys. Lett., 92, 143901 (2008)

[Llusarand2008] Llusarand M, Sanchez C, Chemistry of Materials 20, 782 (2008)

[Mayles2007] Mayles Philip, Nahum Alan, Rosenwald Jean-Claude, Handbook of Radiotherapy Physics: Theory and practice, edited by Taylor & Francis group, LLC, © 2007

[Möhwald1990] Möhwald H Phospholipid and phospholipid-protein monolayers at the air/water interface. Annu Rev Phys Chem 41:441–7 (1990)

[Nag1993] Nag K, Keough KM, Biophys J, 65:1019–26 (1993)

[Nemykin2010] Nemykin V N, Hadt R G, J. Phys. Chem., Revised manuscript sent in October 7, (2010)

[Orsi2011] Orsi D, Cristofolini L and Fontana M P, J. Non-Cryst. Solids 357, 580 (2011)

[Orsi2012] Orsi D, Baldi G, Cicuta P, and Cristofolini L, Colloids Surf. A, 413, 71 (2012)

[Orsi-Madsen2012] Orsi D, Cristofolini L, Baldi G, Madsen A Heterogeneous and anisotropic dynamics of a 2D Gel. Phys Rev Lett 108:105701 (2012)

[Orsi2014] Orsi D, Vezzani A, Burioni R, Pucci A, Ruggeri G, and Cristofolini L, Colloids Surfaces A, 441, 912 (2014)

[Planells2008] Planells M, Forneli A, Martìnez-Ferrero E, Sànchez-Dìaz A, Sarmentero M A, Ballester P, Palomares E and O'Regan B C, Appl. Phys. Lett. 92, 153506 (2008)

[Pockels1891] Pockels A, Nature, 43 (1891)

[Ponchut2011] Ponchut C, Rigal J, Clement M J, Papillon E, Homs A, and Petitdemange S, J. Instrum. 6, C01069 (2011)

[Prudovsky2013] Prudovsky I, Krishnaswamy T, Kumar S, Sterling S and Neivandt D, Int. J. Mol. Sci. 14(2), 3734-3772 (2013)

[Pucci2004] Pucci A, Tirelli N, Willneff E A, Schroeder S L M, Galembeck F, and Ruggeri G, J. Mater. Chem., 14, 3495 (2004)

[Rakow2000] Rakow N A and Suslick K S, Nature 406, 710 (2000)

[Rewin2009] Rewin C L, Jaroszeski M, Weeber E, Muffly K E, Kumar A, Peters M, Oliveros A and Saddow S E, J. Mol. Recognit. 22, 380–8 (2009)

[Roberts1990] Roberts G, Langmuir-Blodgett Films (Plenum Press, 1990), ISBN 978-0306433160

[Ruta2012] Ruta B, Chushkin Y, Monaco G, Cipelletti L, Pineda E, Bruna P, Giordano V M, and Gonzalez-Silveira M, Phys. Rev. Lett., 109, 165701 (2012)

[Saddow2011] Saddow S, Silicon Carbide Biotechnology: A Biocompatible Semiconductor for Advanced Biomedical Devices and Applications, Elsevier MA, USA | ISBN-10: 0123859069 | ISBN-13: 978-0123859068 | Edition: 1 (2011)

[Saffman1975] Saffman P G and Delbruck M, "Brownian Motion in Biological Membranes", Proceedings of the National Academy of Sciences 72(8): 3111-3113 (1975)

[Sahi2013] Sahi S, Chen W, Radiation Measurements 59 139e143 (2013)

[Saini2004] Saini G S S, Sharma S, et al, Spectrochimica Acta A, 61, 3070-3076 (2004)

[Salviati2006] Salviati Giancarlo, Lessons on "Impiego delle microscopie elettroniche ed a sonda per indagini spettroscopiche su scala nanometrica" (2006)

[Santini2012] Santini E, Guzmán E, Ravera F, Ferrari M, Liggieri L, Phys Chem Chem Phys, 14:607–15 (2012)

[Schmidle2013] Schmidle H, Jager S, Hall C K, Velev O D, and Klapp S H L, Soft Matter 9, 2518 (2013)

[Shankar2009] Shankar K., Feng X. & Grimes C.A, ACS Nano 3, 788–794 (2009)

[Simonneaux2006] Simonneaux G, Le Maux P, Ferrand Y and Rault-Berthelot J, Coord. Chem. Rev. 250, 2212 (2006)

[SOSG2004] SOSG kit, produced by Molecular Probes and commercialized by Life Technologies, product information: http://tools.lifetechnologies.com/content/sfs/manuals/mp36002.pdf ("Singlet Oxygen Sensor Green Reagent", revised 30/01/2004)

[Sosnowski2011] Sosnowski TR, Koliński M, Gradón L, Ann Occup Hyg, 55:329–38 (2011)

[Strutt1899] Strutt J. W., Lord Rayleigh, Philosophical Magazine 48 (1899)

[Sutton1991] Sutton M, Mochrie S G J, Greytak T, Nagler S E, Berman L E, Held G A, et al., Nature, 352:608–10 (1991)

[Sutton2008] Sutton M., C R Physique, 9:657–67 (2008)

[Toimil2010] Toimil P, Prieto G, Miñones J, Jr and F Sarmiento, Phys. Chem. Chem. Phys, 12, 13323–13332 | 13323 (2010)

[Woo2008] Woo Boon Kuan, Chen Wei, Joly Alan G. and Sammynaiken R., J. Phys. Chem. C, 112, 14292–14296 (2008)

[Zou2014] Zou X, Yao M, Ma L, Hossu M, Han X, Juzenas P and Chen W, Nanomedicine 9, 15, 2339-2351 (2014)